Abdul Rozak Rivai Fassah

Feasibility Study on Aeroelastic States and Parameters Estimation with Visual Tracking

Technische Universiteit Delft

Feasibility Study on Aeroelastic States and Parameters Estimation with Visual Tracking

by

Abdul Rozak Rivai Fassah

to obtain the degree of Master of Science
at the Delft University of Technology,
to be defended publicly on Tuesday December 19, 2019 at 09:30 AM.

Student number:	4625692	
Project duration:	February 26, 2019 – December 19, 2019	
Thesis committee:	Dr. Q. P. Chu,	TU Delft, chair
	Dr. ir. Coen de Visser,	TU Delft, supervisor
	Tigran Mkhoyan M.Sc,	TU Delft, supervisor
	Dr. Roeland de Breuker,	TU Delft

An electronic version of this thesis is available at `http://repository.tudelft.nl/`.

TU Delft

Abstract

In recent years, developments in the field of aerospace materials and structures has been bringing major breakthroughs in the construction of air vehicles to be more lightweight yet with higher strength. However, the aircraft body can deform more appreciably due to the occurrence of flow separation and flutter. Therefore, active control is necessary in order to maintain structural integrity.

One of the proposed control methods uses visual tracking for structural state estimation which reduces complexity in terms of hardware and data processing requirements compared to the conventional method of inserting a large number of inertial measurement units and gyroscopes in wing sections. The visual tracking routine is then integrated into a new structural state estimation routine that is robust against optical occlusions, and that can accurately reconstruct the states of the complete aeroelastic system. A new idea is to use a state estimator based on a reduced order mathematical model of the aeroelastic wing. This new state estimator is validated in simulation in different gust regimes. The results show that the state estimation convergences to the true values despite the process and measurement noise present in all simulated flight conditions. However, the pole position of the reconstructed state space fails to mimic the stable characteristics of the true model. Further analysis is recommended to constrain the parameter estimation in order to ensure that the stability of the true model can be retained, yielding an accurate solution for the aeroelastic controller feedback.

Preface

This report introduces the readers with the mathematical concept of the aerostructure behaviour in air fluttering condition and the development of basic framework for the feasibilty analysis of using visual tracking as a tool for aeroelastic state and parameter estimation within an active controller scheme for structural integrity. The framework is further implemented in ten simulation cases with different gust realization and structural property for the course AE5310 Thesis in the Delft University of Technology. This assignment is a requirement to complete Master of Science study in the profile of Control and Simulation, in the track of Control and Operations, Faculty of Aerospace Engineering, Delft University of Technology. The main output of this report is to identify the possible framework for the analysis of aeroelastic states' estimation by using the visual tracker, and with that, the research questions and the research plan for the main work of the thesis that will follow.

First of all, praise be to Allah SWT, the Almighty, so that I can finish this phase.

I would like to thank dr. Coen de Visser and Tigran Mkhoyan for giving me the opportunity to work on the topic. They have been very helpful and understanding as my tutor in this assignment and they have been very patient to guide me through the unknowns that I have never encountered during my study in the profile. Special gratitude is also delivered to all PhD students: Yuri, Darwin Rajpal, Francesco, and Andres Jurisson who conducted the wind tunnel tests from 5 April to 17 April 2019 and allowed me to participate directly in the process. That was a precious experience that had given me a better insight on how to solve my ongoing thesis problem.

It was a hard journey constantly filled with ups and more downs during the process to reach this point, hence I am really grateful that I'm supported by friends and family directly or indirectly. I would like to thank the people below for their support and contribution that allowed the writer to reach this completion point:

- My parents, Ir. Sahrul Bosang and Fasicha who has incessantly supported me through the toughest period and kept the writer from breakdowns and downfalls.
- Riska Nur Aini for keeping supporting me from afar with her time and patience.
- All friends in Bosboom-Toussaintplein 28 and Korvezeestraat 160 who have been accompanying me and giving warmth in Delft just like home. Ridho, Fareza, Yanklo, Rafil, Amel, Casy, Helmi, Gilang, Priadi, Aldyth. Without them Delft won't be as cheerful experience.
- All fellow Indonesian students with whom I have been spending my time to work together (or be sad together) in EEMCS faculty building

Abdul Rozak Rivai Fassah
Delft, 10 December 2019

Contents

List of Figures

List of Tables

List of Acronyms

3D	Three Dimension
BLUE	Best Linear Unbiased Estimator
BPOD	Balanced Proper Orthogonal Decomposition
BT	Balanced Truncation
CF	Correlation-Filter Based Visual Tracking
HOG	Histogram of Oriented Gradients
HSV	Hankel Singular Values
IMU	Inertial Measurement Unit
KCF	Kernelized Correlation Filter visual tracker
KMOR	Krylov Subspace Model Order Reduction
LCO	Limit-Cycle Oscillations
MLE	Maximum Likelihood Estimate
MOSSE	Minimum Output Sum of Squared Error visual tracker
MT	Modal Truncation
NRMSE	Normalized Root Mean Square Error
OLS	Ordinary Least-Square
POD	Proper Orthogonal Decomposition
RLS	Recursive Least-Square
RMSE	Root Mean Square Error
ROTS	Reduced-Order Two-Step Method

Nomenclature

α	Angle of attack of the main wing
$\bar{c}$	wing chord
β	Flap angle w.r.t. the wing body
β_{qs}	Quasi-steady aileron deflection
$\ddot{\alpha}$	Angle of attack acceleration
$\ddot{\beta}$	Flap deflection acceleration
$\ddot{\phi}$	Roll angular acceleration of the main wing
$\ddot{\psi}$	Yaw angular acceleration of the main wing
$\ddot{h}$	Heave acceleration
$\ddot{x}$	Surge acceleration of the main wing (Chapter 2)
$\ddot{x}_s$	Displacement's second derivative (acceleration) states
$\ddot{y}$	Sway acceleration of the main wing (Chapter 2)
$\dot{\alpha}$	Angle of attack rate
$\dot{\beta}$	Flap deflection rate
$\dot{\phi}$	Roll angular rate of the main wing
$\dot{\psi}$	Yaw angular rate of the main wing
$\dot{h}$	Heave velocity
$\dot{x}$	Surge rate of the main wing (Chapter 2)
$\dot{x}_s$	Displacement's first derivative (velocity) states
$\dot{y}$	Sway rate of the main wing (Chapter 2)
Γ	Discretized Jacobian matrix, process noise
$\hat{\theta}$	Estimated parameter value
$\hat{\theta}$	Estimated parameters
$\hat{w}$	Classifier
$\hat{x}$	Estimated state value
μ	Mean
ω	Angular velocity
ω	Frequency

ω_d	Damped natural frequency
ω_n	Natural frequency
Φ	Discretized Jacobian matrix, process
ϕ	Phase
ϕ	Roll angular attitude of the main wing
$\phi(s)$	Wagner's indicial function (Subchapter 2.2)
ψ	Yaw angular attitude of the main wing
ρ	Air density
Σ	State covariance matrix
σ	Square root covariance
$\mathbf{w}$	Image weighting classifier
θ	Pitch angle, True parameter value (Subchapter 3.5)
θ_{qs}	Quasi-steady wing-aileron pitch
$\underline{\eta}$	Kalman Filter iterator
$\underline{h}$	Nonlinear measurement equation
$\underline{x}$	Real states value
$\underline{x}*$	Perturbed real states value
$\underline{z}$	Real output value
ς	Standard deviation
$\vec{\mathbf{F}}_a$	Forces and moment matrix
ζ	Damping coefficient
a	Wing shear center location
a, A	Regression matrix (Chapter 3)
A_0	Wave amplitude
B	Bias
b	Half chord length
C	Damping
c	Aileron hinge coordinate from half chord
C_α	Angular damping of the wing-aileron
C_β	Angular damping of the aileron
C_a	Damping parameter matrix due to aerodynamic lag influence
C_h	Translation damping of the wing-aileron
C_S	Damping parameter matrix due to aeroelastic structure property
C_Z^c	Total circulatory lift coefficient

$C_Z^{\beta,c}$	Total circulatory lift coefficient due to the aileron deflection
$C_Z^{\theta,c}$	Total circulatory lift coefficient due to the wing pitch
e	Output error
$E(\cdot)$	Expected value
f	Specific force
G	Nonlinear process noise
h	Heave displacement
i	(subscript) Wing section (Subchapter 2.3)
I_α	Wing moment of inertia
I_β	Flap moment of inertia
K	Kalman gain (Chapter 3)
K	Stiffness
k	(subscript) Discretized data step
$k+1,k$	(subscript) Kalman Filter One-step ahead prediction
$k+1,k+1$	(subscript) Kalman Filter One-step ahead optimal prediction
k,k	(subscript) Kalman Filter Current optimal estimation
K_α	Angular stiffness of the wing-aileron
K_β	Angular stiffness of the aileron
K_a	Stiffness parameter matrix due to aerodynamic lag influence
K_h	Translation stiffness of the wing-aileron
K_S	Stiffness parameter matrix due to aeroelastic structure property
M	Mass
M_α	Moment of the main fuselage in wing axis (Subchapter 1.1)
M_α	Wing rotational moment
M_α^c	Circulatory wing moment
M_β	Flap rotational moment
M_β	Moment of the wing-aileron body in wing axis (Subchapter 1.1)
M_β^c	Circulatory aileron moment
M_a	Mass parameter matrix due to aerodynamic lag influence
M_S	Mass parameter matrix due to aeroelastic structure property
N	Number of samples
P	State covariance
Q	Measurement covariance matrix
R	Process covariance matrix

S	Wing surface
S_α	Static unbalance of the wing-aileron
S_β	Static unbalance of the aileron
T	Simulation period
t	Time
U_N	Discretized Input
V	Airspeed
v_0	Initial velocity
W	(subscript) Wing
x	Surge attitude of the main wing (Chapter 2)
x_0	Initial position
y	Sway attitude of the main wing (Chapter 2), Output matrix (Chapter 3)
Y_N	Discretized Output
Z	Force on Z-axis of Earth frame
Z^c	Circulatory lift
K_z	Aerodynamic lag parameter matrix
x_s	Displacement states
z_i	Aerodynamic lag states
$_{true}$	Estimated true model states value
ρ_P	Pearson correlation coefficient
$\mathbf{A}_{red}$	Balanced realization of **A** state-space matrix
$\mathbf{B}_{red}$	Balanced realization of **B** state-space matrix
$\mathbf{C}_{red}$	Balanced realization of **C** state-space matrix
$\mathbf{D}_{red}$	Balanced realization of **D** state-space matrix
x_{bias}	Biased true model states value
x_{red}	Reduced model states value
x_{true}	True model states value

Chapter 1

Introduction

1.1 Introduction to Aeroelasticity and Basic Understanding of Flutter Occurrence

Aeroelasticity is a discipline in aerospace engineering that focuses on the deformations of elastomechanical bodies due to aerodynamic acts [53]. From this definition, it can be seen that the aerodynamic forces and moments acting on a body passing through such airflow will then excite such a structural response on the body. The response is generally named as deformation. The interaction of the two aspects of aeroelasticity is well described in Fig. 1.1.

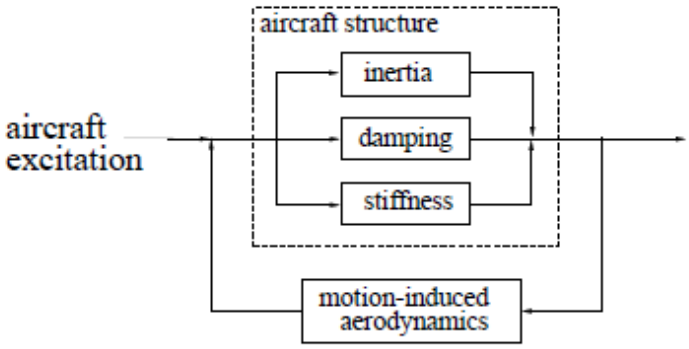

Figure 1.1: Interaction between aerodynamics and structural dynamics [53].

In recent years, the development in the field of aerospace material and structure has been bringing a significant breakthrough for the construction of air vehicles. The contribution of this field of research brings a significant impact, such as by introducing the lighter material for aircraft structural components, improving the strength of the material, and introducing the composite material to the aircraft. These all allow the expansion of dimensional constraints of aerostructure. However, due to its lightweight, the airplane structure can deform appreciably under such external aerodynamic loads. Such deformation changes the distribution of aerodynamic load, which then changes the distribution of deformations across the aircraft body. The flexibility of such aircraft leads to large deformation so that linear theories are not relevant for the analysis [63]. This condition implies that the aircraft should then be treated not as a rigid body but as an elastic structure [20].

As a consequence of the deformation of the aircraft body, the occurrence of flow separation due to gust and turbulence may cause degradation of the aircraft flight performance or handling qualities [38]. The highly undesirable rigid-body motion of aircraft due to airflow disturbance may also cause an autonomous oscillation, better known as a "limit cycle." Limit cycle oscillation (LCO) occurs when the nonlinear mean aerody-

namic forces become significant. LCO may also occur in the flow field are coupled deterministically to the wing motion [38]. Non-linearities in the structure or the aerodynamic forces can induce pre-flutter LCO or lead to limiting the amplitude of oscillations of an unstable system [62]. This feedback interaction between the airflow and the aircraft structures may lead to a flutter phenomenon. Flutter is a complex phenomenon that must, in general, be eliminated from occurring within the flight envelope [20].

Fluttering and buffeting are two types of nonlinear input that may cause change to the shape of the aircraft. Mayuresh J. Patil (2004) described the energy transfer interrelations as viewed in Figure 1.2 among propulsion, structure, and airflow. At fluttering mode, it is observed that the energy produced by the propulsive system is lost to the fluid due to the occurring separation. Therefore, the energy used to maintain the stability of the structure decreases. This loss causes instability to the aircraft structure that then turns to increase the drag of the aircraft. This instability phenomenon of the relative airflow is associated with separation rand produces the driving forces known as buffeting, while buffeting is the flexible response to the fluid motion [38]. The vibration level or buffeting intensity, defined by local accelerations or displacements at either natural or forced frequencies as a consequence of energy loss to the system damping. When the oscillations or displacement does not converge over time, the structural disintegration can then occur [38] [36].

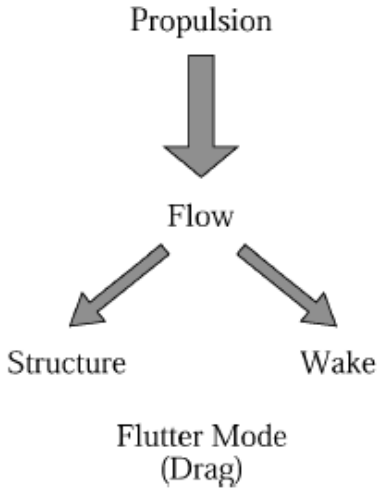

Figure 1.2: Energy transfer relation among propulsion, structure, and airflow [62].

In general, high aspect ratio lifting surfaces undergo a greater degree of structural deflections than low aspect ratio lifting surfaces [58]. By this comprehension, this means that the main wing of the aircraft will undergo the largest deformation. This large deformation occurs as the wing has the highest aspect ratio on the aircraft structure. Since the main wing is the most significant lifting surface contributor to the aircraft structure, the interaction between the aerodynamics and the structure can excite one or more elastic modes. The elastic modes can cause a significant change in the aerodynamic properties of the wing. The change in the wing property potentially causes undesired aircraft responses, which will also cause further degradation in the handling qualities of the aircraft [58]. Therefore, to maintain the handling quality of the aircraft at the regime, a control scheme is developed with the purpose of maintaining structural integrity during the fluttering condition. An aeroelastic estimation routine needs to be built to identify the displacement states of the flexible design of aircraft structure such that a more accurate state observation can be used to identify the governing state-space of the aeroelastic structure. The identified state-space can then become input for the feedback to the aforementioned controller dedicated to maintaining the integrity of the aerostructure, namely wing. Such that the more robust and fault-tolerant controller can work with controlling the aerodynamic and aeroelastic influence to the structure.

1.1.1 Problem Statement

In order to identify the system of aeroelasticity of a structure, an estimator routine for aeroelastic structure needs to be built to identify the profile of the flexible design of modern aircraft structure. However, in contrast to rigid states, aeroelastic state estimation requires more measurement points across the span to deduce the vibrational shapes of the wing excitations. To correctly capture all the operational modes, this requires a high number of accelerometers and careful geometric placement of these sensors.

However, there is, in reality, a limited amount of IMU that can be applied to the flexible structure. Hence, not all wing sections displacements can be derived from the measurement from the accelerometer. Furthermore, the body accelerations, velocities, and displacements certainly diminish along with a closer gap to the root of the wing since the root is not free to move. Therefore the root section will yield a huge stiffness and damping value. Furthermore, the related computation system also needs to work at a high sampling rate. The force and moment of each wing section can be considered as uniform across the wingspan [14].

In the Department of Control and Simulation, the Delft University of Technology, a new novel way to simplify the problem of aeroelastic state estimation due to hardware and data processing complexity is by exploiting the visual tracker. This method reduces the complexity in terms of hardware and complexity of data processing compared to the conventional method of planting inertial measurement units and gyroscopes in wing sections. The scheme of the controller for the aeroelastic structure is depicted in Figure 1.3

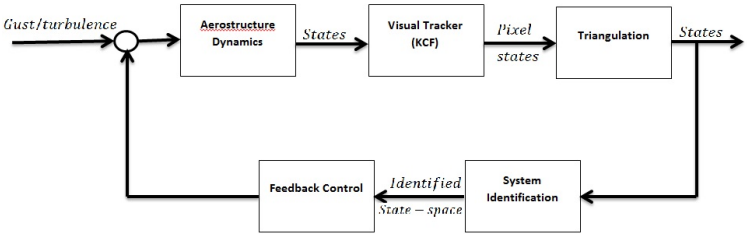

Figure 1.3: Controller scheme of an aeroelastic wing.

However, the visual tracker needs to run at a high-frame-rate to be able to capture the deformation modes that occur on the aircraft structure. In the meantime, the advancement in the image processing field develops algorithms that allow visual object tracking at a high frame rate. In general, a fast-tracking system uses the identification of features like edges, corners, or blobs (a feature that has an area) on the image as the basis of the tracking. The first developed routine called fragment tracking has been developed by Lucas and Kanade [54] and Shi [71]. However, the tracking is constrained by the transformation of the feature perspective of the image. The object displacement causes this change that, in turn, changes the shape of the features attached. Hence, this will cause drift of the tracker. The transformation of the feature's perspective can be mitigated by using the mean shift tracker routine or color based tracking [15]. Here, instead of the intensity of the pixel patch that is used to detect the object of interest. The color histogram becomes the object of the minimization problem. In this problem, the distance of the referred color histogram should be minimal compared to the position of candidate tracklet position in the proceeding frames. Despite the advancements, however, the constraint remains as the color distribution is the determining variable in the tracker. Since the object is "blurred" with the color kernel, it is harder for the tracker to detect the abrupt moves and the features of the object. More recently, the correlation-filter (CF) based tracker is developed for the feature tracking routine. In general, the CF routine divides the training image into subwindows with a predetermined target or object of interest. These subwindows than can be labeled or weighted such that the target position can then be acquired. The weight (**w**) or the classifier of the subwindow will be positive if the subwindow has a high overlap with the ground truth while the contrary will be given for subwindow far or lowly correlate with the ground truth or target. In order to give a perspective to the readers, the following figure depicts the cross-correlation process in the tracker routine.

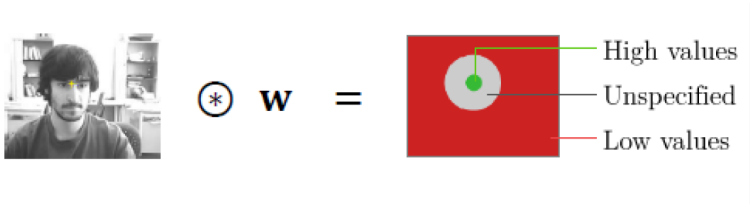

Figure 1.4: Cross-correlation process in discriminative tracker.

From Figure 1.4, it can be seen that the high value is given at the true location of the target while the other location is given low value. The high value surrounding low values creates something called peak. At an earlier stage, Bolme et al. [8] introduced the distribution of the correlation output as a Gaussian peak in their MOSSE routine. The correlation output surrounding the target location follows the two-dimensional Gaussian shape distribution, which removes the hard constraints constituted by ordinary peak calculation. This method gives the advantage to the MOSSE tracker to work at a very high frame rate (600 fps). However, the routine is limited to raw pixel image only. Therefore, the tracking is not based on the feature since it cannot be in the single-channel image. This limitation, in turn, yields a poor performance even when the object is stable. A more recent algorithm developed is Kernelized Correlation Filter [30], which tracks based on the histogram of oriented gradients (HOG) of the object of interest. This allows the routine to run at approximately 130-150 Hz with an accuracy of more than 90 percent [34]. However, the routine's accuracy is still hampered by the occlusion problem. This problem can be mitigated with the combination of a visual tracker routine with state estimation. It is exemplified by combination of visual tracker with Kalman Filter routine in pixel reference frame as in [19],[11], and [66]. Due to the nature of aeroelastic structure dynamics, the monitoring will have to be performed at multiple wing sections, whereas the angular attitude also requires multiple objects for each wing section. Once the object position is pinpointed, the position in the true world reference frame can be obtained by transforming the pixel coordinates through triangulation calculation [29]. In contrast, the angular attitude also requires multiple objects for each wing section. Furthermore, the proposed pixel-based state estimation is also constrained to model the object movement at one axis.

A new idea was based on real-time parameter estimation by using the aeroelastic dynamics mathematical model instead of using the raw pixel reference frame position in order to determine the displacement of the wing sections. The background is because the pixel unit by itself is an area. Hence the extracted position in the world reference frame will also have uncertainties. The coupling potentially yields, in turn, accurate estimation of wing sections displacement states. Hence the estimated dynamics can become an input for the parameter estimator to estimate the governing state-space representation for the basis of the active controller to mitigate the fluttering behavior of the wing-aileron body in real-time. However, as formerly mentioned, the modes of displacement for an aeroelastic structure requires measurements at numerous wing sections. The increase in the number of states to estimate will increase the computational, which will hinder the utilization of a high sampling rate system. The realization of the state-space for an aeroelastic structure should be then reduced in order to reduce the number of states to estimate, hence the computational cost for the controller will be cheaper. The expected accurate estimation can be yielded so that the estimated dynamics becomes an input for an active controller to mitigate the fluttering behavior of the wing-aileron body, as exemplified by Timme et al. [75].

The first step in the implementation of the research for the controller scheme is by testing the open-loop part in the numerical simulation environment. In order to analyze the feasibility of this new approach, a set of simulations is formulated. First, the mathematical model of the dynamics of an aeroelastic structure will be investigated. Once the mathematical state-space has been formulated, the displacement states value will be sent to a simulated visual model where the fast visual tracker routine, in this case, is KCF, is embedded. The pixel value obtained from the visual tracking routine will be transformed again through the triangulation process. The state estimation would be based on the inputs and the position obtained from the visual model. The corrected displacement position will be fed back to the visual model and correct the position of the visual tracklet. The unbiased state value will be used as the basis for parameter estimation. The rough picture of the whole numerical simulation process is depicted in Figure 1.5.

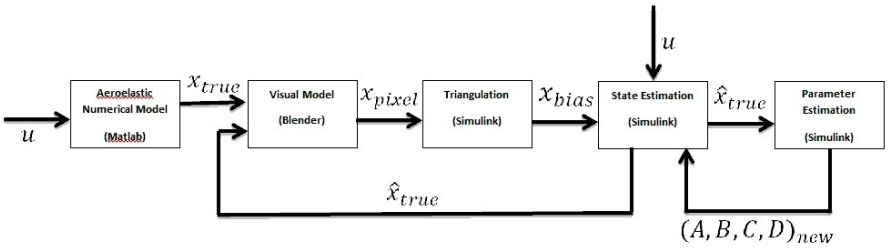

Figure 1.5: Rough picture of numerical simulation process.

1.2 Research Objective and Questions

Based on the problem backgrounds stated in the previous paragraph, the goal of this report is to analyze the feasibility of such a controller scheme in numerical simulation before the implementation in the real-life. The open-loop analysis will be focused, as described in Figure 1.6.

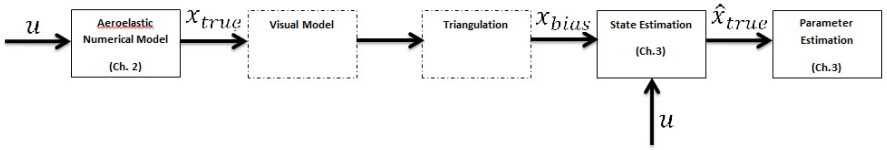

Figure 1.6: Focus parts of the numerical simulation.

The analysis that will be conducted in this report contains a few parts of the full controller scheme. As shown in Figure 1.6, this consists of the modeling of the aeroelastic model with its contributing states and its reduction and to deliver the results of numerical simulation of aeroelastic states and parameters estimation in a high-frame-rate visual tracking environment. For the focus of the paper, the visual model, which represents the physical representation of the wing and the embedded fast visual tracking routine, will be put aside. Hence, the triangulation will be unnecessary. Nevertheless, the calculation process is constrained by the limitation of the visual tracker itself, such as the sampling rate and also the transformed sensor noise from the pixel reference frame. Therefore, based on the previous scheme of the full numerical simulation, the paper will investigate the aeroelastic mathematical modeling and the system identification part, which consists of state and parameter estimation The developed algorithm can also be implemented later **in other various estimation of fast linear system states and parameters with similar hard limitations, such as processing or sampling rate**.

The research objective is then specified as:

- **Contribute** to the development of the online state estimator for the dynamics and aeroelastic constants from the nonlinear flexible structure of flexible rectangular wing **by** investigating the feasibility of application of existing online state estimation framework within active controller scheme for structural integrity control with visual tracking to estimate aeroelastic dynamics and its parameters in Theodorsen's fluttering condition.

In order to achieve the mentioned objective, few research questions are formulated as follows:

1. How can states and parameters of a nonlinear aeroelastic system be estimated by using the fusion of visual tracker and state estimation routine in real-time?

    - (RQ 1.1) What is the theoretical basis for the aircraft aeroelastic behaviors, and how does the behavior of the aeroelastic wing in fluttering or buffeting condition be represented mathematically?

- (RQ 1.2) Given the numerical measurement and process noises occurring in the process and the limitation of the hardware, what is the structure of the state and parameter estimation routine for the estimation of the aeroelastic object in visual tracking environment?
- (RQ 1.3) With the proposed framework, how does the state estimator routine in different conditions approximate the correct response? In other words, how robust is the proposed method for the different realization of turbulence, and what are the influencing parameters that may affect the state estimation results with the given system environment?
- (RQ 1.4) How does the proposed method reconstruct the true parameter values such that the reconstructed system can imitate the true model of the system? What is the error that occurs during the parameter estimation?

1.3 Report Outline

As mentioned before, the main goal of this research is to investigate the feasibility of the application of an existing online state estimation framework within an active controller scheme for structural integrity control with visual tracking to estimate aeroelastic dynamics and its parameters in Theodorsen fluttering condition. The core of this work will then be to create an aeroelastic state estimation routine that can yield the information in real-time with consideration of processing and sampling rate of hardware. Therefore, to achieve the main goal, the survey will be then aimed at two objectives. First, the mathematical model of an aeroelastic body in the flutter condition will be identified. Once the dynamics are known, it is then possible to identify the states and parameters which needs to be identified, the means of estimating states and constant parameters of the aeroelastic system will be then discussed along with the possible model reduction methods to allow a cheaper computational cost to build the full framework for the feasibility study of aeroelastic state estimation by using visual tracking.

The introduction of the flutter and the problem background has been stated in this chapter, and the main part of the report will be divided into two parts afterward. First, the derivation of the two-dimensional aeroelastic equations of motion in fluttering condition and its development as the basis for a three-dimensional aeroelastic model will be deciphered in Chapter 2. Next, the identification of the related state and parameter estimation routine and additional step with the goal of simplification of the system with the concern of the limitation of the system will be presented in Chapter 3 along with the discussion in regards to building the framework of state estimation routine with visual tracking. The numerical simulation results based on the built framework will be then displayed and discussed in Chapter 4. In addition to that, the results of additional simulation cases will be presented in Chapter 5. Lastly, the report will be closed with the conclusion in Chapter 6.

Chapter 2

Introduction to History of Flutter Research and Mathematical Model of Aerostructure in Fluttering Condition

In the next subchapter, the basic understanding and history of aeroelastic research development will be featured, and the underlying two-dimensional wing problem will then be derived. Furthermore, the Subchapter 2.2, the aerodynamic trailing circulatory lift influence to the aeroelastic equation of motion will be derived by integrating the Leishman state space into the general aeroelastic equation of motion. The two-dimensional wing equation of motion knowledge will become the basics to derive the three-dimensional wing problem in the Subchapter 2.3.

2.1 History of Subsonic Aeroelastic Research and The General Equation of Two-Dimensional Wing Problem

A few scientists proposed the basis of two-dimensional approaches to solving the structure fluttering model. These are: 1) Velocity potential method was proposed by Theodore Theodorsen (1935); 2) Vortex distribution method by Kuessner (1936) [45] and Schwarz (1940), and; 3) Integral equation method by Possio (1938) [53]. Here, Theodorsen's method as the earliest method to occur for two-dimensional aeroelasticity problem made a difference by not using Routh's discriminants to deal with sinusoidal aerodynamic behavior [38]. The discovery leads to several parametric ways of finding the flutter solution. In 1925, another model was developed in order to investigate the flutter behavior on time-domain against a step disturbance. It can be traced that Wagner and Theodorsen's works are each related in the Fourier transform [73]. This has been proven by Jones [39], where the outcome of the indicial response function derived by Wagner only deviates by a small percentage from the results obtained by using Theodorsen's work. Later the ground of Wagner's function would then become the basis in order to approximate the aerodynamic lag or Theodorsen's function in the time domain [48]. Their results are only valid at zero velocity, utter velocity, or in the presence of a sinusoidal excitation [2].

Because of the ability to capture the unsteady effects in a compact form, finite-state aerodynamic models (Theodorsen's work) has become the main base for flight dynamics and aeroelastic simulations and control design ([62],[47],[73]), as well as its application in industry [2].

2.1.1 The General Equation of Two-Dimensional Wing Problem

In a wing-aileron two-dimensional wing model, the two-dimensional wing-aileron has three degrees of freedom, namely the angular movement (pitch) of the wing-aileron system, the angular movement (pitch) of the aileron, and the translation (heave or plunge) movement of the wing-aileron system. As the equations of total force and moments acting on the wing-airfoil body at fluttering condition have been established, Theodorsen ([74], p. 9) established the general differential equations of motion for each angular and transla-

tional attitudes as

$$\begin{aligned} M_\alpha &= I_\alpha \ddot{\alpha} + (I_\beta + b(c-a)S_\beta)\ddot{\beta} + S_\alpha \ddot{h} + K_\alpha \alpha \\ M_\beta &= (I_\beta + b(c-a)S_\beta)\ddot{\alpha} + I_\beta \ddot{\beta} + S_\beta \ddot{h} + K_\beta \beta \\ Z &= S_\alpha \ddot{\alpha} + S_\beta \ddot{\beta} + M\ddot{h} + K_h h \end{aligned} \tag{2.1}$$

where ρ is the air density, b represents the half chord of wing, M represents the mass of the unit body. S represents the static moment per unit length, I represents the moment of inertia of the body, and K represents the stiffness of wing on respective subscripted axes. The subscripts α, β, & h respectively represents the angular wing-aileron, angular aileron, and plunge deflection attitudes.

As observed, the differential equations above resemble an undamped mass-spring system with the time-domain characteristic equation of $M\ddot{x} + Kx = F$. From here, the angular frequency and the damping of the system are zero. Practically speaking, some small amount of damping is known to exist in the system. Useful numerical analysis and simulation will not be possible with the addition of some structural damping, and so for full modeling [2]. The phenomenon was found evident as well in papers regarding the subject [77],[38],[75]. Therefore, with the addition of damping part into the system, Equation 2.1 becomes

$$\begin{aligned} M_\alpha &= I_\alpha \ddot{\alpha} + (I_\beta + b(c-a)S_\beta)\ddot{\beta} + S_\alpha \ddot{h} + C_\alpha \dot{\alpha} + K_\alpha \alpha \\ M_\beta &= (I_\beta + b(c-a)S_\beta)\ddot{\alpha} + I_\beta \ddot{\beta} + S_\beta \ddot{h} + C_\beta \dot{\beta} + K_\beta \beta \\ Z &= S_\alpha \ddot{\alpha} + S_\beta \ddot{\beta} + M\ddot{h} + C_h \dot{h} + K_h h \end{aligned} \tag{2.2}$$

where C represents the damping system. In the system of unflapped wing, the flap-related parameters can then be written off the equation. Hence, the equation above can be resimplified for clean wing to become

$$\begin{aligned} M_\alpha &= I_\alpha \ddot{\alpha} + S_\alpha \ddot{h} + C_\alpha \dot{\alpha} + K_\alpha \alpha \\ Z &= S_\alpha \ddot{\alpha} + M\ddot{h} + C_h \dot{h} + K_h h \end{aligned} \tag{2.3}$$

Hence, the characteristic equation then resembles $M\ddot{x} + C\dot{x} + Kx = F$. The modal mass matrix at multiple 2D airfoil wing is represented as M while the modal damping and stiffness matrix are respectively referred as C and K.

In a homogeneous solution, transforming the characteristic equation from the time domain into frequency domain [60], [36]. The frequency-domain relation between input and output of the system becomes

$$\frac{X(s)}{F(s)} = \frac{1}{Ms^2 + Cs + K} \tag{2.4}$$

As specific force f is divided by mass, then

$$\frac{X(s)}{f(s)} = \frac{1}{s^2 + (\frac{C}{M})s + \frac{K}{M}} \tag{2.5}$$

where

$$\frac{C}{M} = 2\zeta\omega_n \tag{2.6}$$

where ζ is the damping coefficient and natural frequency ω_n is

$$\omega_n = \sqrt{\frac{K}{M}} \tag{2.7}$$

The general solution of the wing displacement is

$$x(t) = A_0 e^{-\zeta\omega_n t} sin(\omega_d t + \phi) \tag{2.8}$$

where the damped natural frequency, ω_d, is formulated as

$$\omega_d = \omega_n \sqrt{1 - \zeta^2} \tag{2.9}$$

and the amplitude (A_0) and initial phase of the wave becomes

$$\begin{aligned} A_0 &= \sqrt{x_0^2 + (\frac{\zeta\omega_n x_0}{\omega_d} + \frac{v_0}{\omega_d})^2} \\ \phi &= arctan\frac{\omega_d x_0}{\zeta\omega_n x_0 + v_0} \end{aligned} \tag{2.10}$$

2.2 Aerodynamic Lag Influence to Aeroelastic Formulation (Leishman State Space)

Despite the elaborative derivation of the aeroelasticity state space and the formulation of the general solution of aeroelastic structure's equations of motion by Theodorsen, the equation still discounts the effect of the aerodynamic lag effect in its representation in the time domain. This is because the aerodynamic lag is still represented in the frequency domain so that the representation in time-domain state space is difficult. In the paper by de Breuker on the investigation of combined active and passive loads alleviation through aeroelastic tailoring [14], the combined state space of aerodynamic and structural influence is reformulated as

$$\vec{\mathbf{F}}_a = (M_a + M_s)\ddot{x}_s + (C_a + C_s)\dot{x}_s + (K_a + K_s)x_s + K_z z_i \tag{2.11}$$

where

$$\vec{\mathbf{F}}_a = [Z, M_\alpha] \tag{2.12}$$

the states are x_s whereas z_i represents the aerodynamic "stiffness" lag states due to trailing circulatory lift and the K_z represents the aerodynamic lag matrix. The M_s, C_s, K_s represent the structure influence matrix as derived in previous subsection. M_a, C_a, K_a represent the aerodynamic influence to the total "mass", damping, and stiffness respectively.

The readers may question how the aerodynamic lag states and aerodynamic lag matrix are obtained. Therefore, to answer the question, the Leishman paper is used as the reference [48]. The aerodynamic circulatory effect or lag is needed to fully capture the flutter phenomenon based on the Theodorsen's model [48]. However, this aerodynamic lag or Bessel function is written in the frequency domain. As it has already been observed in other paper, most of the approximation conducted is also using the complex frequency domain value to approximate this [53][6]. Since the non-circulatory aerodynamics expression in the time domain exists, the circulatory aerodynamics caused by wake near the trailing edge should then be represented in the time domain. Leishman introduced an approximation of this in the time domain by using indicial function approximation [48].

The lag effects that are present in the unsteady aerodynamics through the Theodorsen function are represented in the time domain by additional lag states. Hence the unsteady aerodynamics are purely in the time domain, but the number of states is increased [14]. These additional states of aerodynamic lag will then constitute the circulatory lift caused by the aerodynamic lag. The circulatory lift caused by pitch ($C_Z^{\theta,c}$) is affected by the aerodynamic lag states of z_1 and z_2. de Breuker et al. [14] gives a solution where the wake-induced lift can be combined such that the total coefficient lift becomes

$$C_Z^c = C_Z^{\theta,c} + C_Z^{\beta,c} = 4\pi\left(\frac{b_1 b_2}{2}\left(\frac{V}{b}\right)^2 z_1 + (A_1 b_1 + A_2 b_2)\frac{V}{b} z_2\right) + \pi\theta_{qs} + \pi\beta_{qs} \tag{2.13}$$

where the coefficients of $A_1, A_2, b_1, \& b_2$ is derived from the exponential fit to Wagner indicial response function which has been approximated by Jones [39] as

$$\begin{aligned} \phi(s) &= 1.0 - A_1 exp(-b_1 S) - A_2 exp(-b_2 S) \\ \phi(s) &= 1.0 - 0.165 exp(-0.0455S) - 0.335 exp(-0.3S) \end{aligned} \tag{2.14}$$

and

$$\begin{aligned} \theta_{qs} &= \frac{\dot{h}}{V} + \theta + b(1/2 - a)\frac{\dot{\alpha}}{V} \\ \beta_{qs} &= \frac{T_{10}\beta}{\pi} + \frac{bT_{11}\dot{\beta}}{2\pi V} \\ \theta &= \alpha - \frac{\dot{h}}{V} \end{aligned} \tag{2.15}$$

Therefore,

$$\begin{aligned} \theta_{qs} &= \alpha + (b(1/2 - a))\frac{\dot{\alpha}}{V} \\ \beta_{qs} &= \frac{T_{10}\beta}{\pi} + \frac{bT_{11}\dot{\beta}}{2\pi V} \end{aligned} \tag{2.16}$$

Adding these lag states into the structural-aerodynamic equations of motion itself is making the equation non-solvable as the values of these lag states can also differ over time. Therefore, Leishman introduces the first derivative of lag states equation where

$$\begin{bmatrix} \dot{z}_1 \\ \dot{z}_2 \end{bmatrix} = \begin{bmatrix} 0 & 1 \\ -b_1 b_2 (\frac{V}{b})^2 & -(b_1 + b_2)(\frac{V}{b}) \end{bmatrix} \begin{bmatrix} z_1 \\ z_2 \end{bmatrix} + \begin{bmatrix} 0 \\ \frac{1}{2} \end{bmatrix} \theta_{qs} + \begin{bmatrix} 0 \\ \frac{1}{2} \end{bmatrix} \beta_{qs} \tag{2.17}$$

Back to the calculation of lift coefficient due to the circulatory flow, the lift force due to the aerodynamic lag can then be easily calculated as

$$Z^c = \frac{1}{2} \rho V^2 S C_Z^c \tag{2.18}$$

from which the moment due to the airfoil attitude can then be calculated as

$$M_\alpha^c = Z^c b (\frac{1}{2} + a) \tag{2.19}$$

Returning to the first equation presented in this subsection, the lag states matrix and the corresponding states contribute to each force or moment of the clean wing with an amount of

$$K_z z_i = \begin{bmatrix} M_\alpha^c \\ Z^c \end{bmatrix} = \frac{1}{2} \rho V^2 S \begin{bmatrix} b(\frac{1}{2} + a) \\ 1 \end{bmatrix} (4\pi \begin{bmatrix} \frac{b_1 b_2}{2} (\frac{V}{b})^2 & (A_1 b_1 + A_2 b_2) \frac{V}{b} \end{bmatrix} \begin{bmatrix} z_1 \\ z_2 \end{bmatrix} + \pi \theta_{qs}) \tag{2.20}$$

Adjusting the aerodynamic lag contribution formulation above into a two dimensional problem, then

$$\begin{aligned} K_z z &= \begin{bmatrix} M_\alpha^c \\ Z^c \end{bmatrix} = \frac{1}{2} \rho V^2 S \begin{bmatrix} b(\frac{1}{2} + a) \\ 1 \end{bmatrix} (4\pi \begin{bmatrix} \frac{b_1 b_2}{2} (\frac{V}{b})^2 & (A_1 b_1 + A_2 b_2) \frac{V}{b} \end{bmatrix} \begin{bmatrix} z_1 \\ z_2 \end{bmatrix} + \pi \theta_{qs}) \\ &= \begin{bmatrix} \frac{1}{2} \rho V^2 S (b(\frac{1}{2} + a))(4\pi \frac{b_1 b_2}{2} (\frac{V}{b})^2) & \frac{1}{2} \rho V^2 S (b(\frac{1}{2} + a))(A_1 b_1 + A_2 b_2)(\frac{V}{b}) \\ \frac{1}{2} \rho V^2 S (4\pi \frac{b_1 b_2}{2} (\frac{V}{b})^2) & \frac{1}{2} \rho V^2 S (A_1 b_1 + A_2 b_2)(\frac{V}{b}) \end{bmatrix} \begin{bmatrix} z_1 \\ z_2 \end{bmatrix} \\ &+ \begin{bmatrix} \frac{1}{2} \rho V^2 S (b(\frac{1}{2} + a))\pi & \frac{1}{2} \rho V S (b(\frac{1}{2} + a))^2 \pi \\ \frac{1}{2} \rho V^2 S \pi & \frac{1}{2} \rho V S (b(\frac{1}{2} + a))\pi \end{bmatrix} \begin{bmatrix} \alpha \\ \dot{\alpha} \end{bmatrix} \end{aligned} \tag{2.21}$$

Where $\bar{c}$ represents the chord length of the wing system. From the derivation of quasi-steady pitch, it can be seen that the aerodynamic lag also contributes to the angular attitude and angular rate of the wing. This in turn signifies that the angular attitude is not influenced by only the structural damping and stiffness but also by the interaction between the structure and the aerodynamic environment as well.

Integrating the angular attitude and rate-dependent variable matrix into the damping and stiffness matrix of the system, now there is only one variable matrix left. The remaining parameter is dependent on the aerodynamic lag states of $z_1 \& z_2$. This yields

$$K_z = \begin{bmatrix} \frac{1}{2} \rho V^2 S (b(\frac{1}{2} + a)(4\pi \frac{b_1 b_2}{2} (\frac{V}{b})^2) & \frac{1}{2} \rho V^2 S (b(\frac{1}{2} + a)(A_1 b_1 + A_2 b_2)(\frac{V}{b}) \\ \frac{1}{2} \rho V^2 S (4\pi \frac{b_1 b_2}{2} (\frac{V}{b})^2) & \frac{1}{2} \rho V^2 S (A_1 b_1 + A_2 b_2)(\frac{V}{b}) \end{bmatrix} \tag{2.22}$$

In addition to that, the gust phenomenon can also add to the dynamic aerodynamic excitation. As the gust also possesses lag terms due to the wake effect. Other pairs of lag states can also be added to account for the gust effect signal that makes up the true gust wave.

2.3 Three-dimensional wing aeroelastic behavior solution

Given the solution of the two-dimensional aeroelastic system which has been derived above, it is now possible to expand the model into a three-dimensional wing model. The depiction of inter-relation among all two-dimensional elements in the three-dimensional wing model is well figured in Figure 2.1.

Revisiting Figure 2.1, the movement of each section is not constrained by the presence of damping or stiffness of the wing in the heaving axis. In reality, the heaving attitude of wing sections is also constrained by the skin and inner spar of the wing. Therefore a more complex model based on the referred figure. For each degree of freedom, the movement of the wing is constrained by the stiffness of the given axis. These stiffness for each section is then renamed as K_{hi} and $K_{\alpha i}$ for each i^{th} section of wing. The axis of rotation is assumed to be along the elastic axis, so no stiffness coupling exists between pitch and heave modes. However, stiffness effects between segments propagate through the model so that each stiffness interface influences the

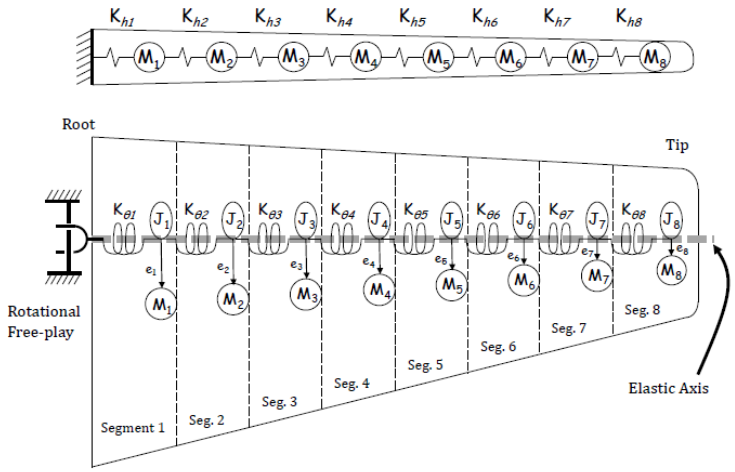

Figure 2.1: Example of three-dimensional wing model [2]

dynamics at each segment. As a result, the coupling of stiffness from all sections give a modification to the Theodorsen's differential equations of motion to every i^{th} wing section as

$$\begin{aligned} M_\alpha &= I\ddot{\alpha} + S_\alpha \ddot{h} + \sum_{j=1}^{n} K_{\alpha ij}\alpha_j \\ Z_i &= S_\alpha \ddot{\alpha} + M\ddot{h} + \sum_{j=1}^{n} K_{hij} h_j \end{aligned} \tag{2.23}$$

However, as discussed in the derivation of Theodorsen's work, small damping is also observed when researching the flutter phenomenon [77][36]. The magnitude of this damping is observed between 0 and 0.05. Hence the damping is also present in the equation. However, as damping also occurs on each wing section, it interferes as well with the dynamics of other related wing section. Therefore, the equation above becomes

$$\begin{aligned} M_\alpha &= I_\alpha \ddot{\alpha} + S_{\alpha,}\ddot{h} + C_\alpha \dot{\alpha} + \sum_{j=1}^{n} K_{\alpha ij}\alpha_j + (K_z z)_i \\ Z &= S_\alpha \ddot{\alpha} + M\ddot{h} + C_h \dot{h} + \sum_{j=1}^{n} K_{hij} h_j + (K_z z)_i \end{aligned} \tag{2.24}$$

In addition to that, the problem formulation expansion to the three-dimensional problem also means that the rolling and yawing attitude of the wing also influences the equation and the forces of remaining axes. This expands the problem into a six-degree of freedom problem $(\phi, \alpha, \psi, x, y, h)$.

The readers might wonder the decision of the writer to keep using the angle-of-attack instead of pitch angle to represent the angular attitude of the wing around its Y-axis. While in some papers interchange the term of the angle-of-attack with the pitching angle, it can be understandable from the relation derived between pitch and angle of attack in Equation 2.15. When the heave rate is low, and the air free velocity is high, the $\frac{\dot{h}}{V}$ term will then yield minute value such that the pitch angle can be considered equal to angle-of-attack. However, since Theodorsen[74] and Leishman and Nguyen [48] use the angle of attack term, hence the term is retained to maintain the consistency. As compensation, the pitch angle can be derived by using the relation previously described in Equation 2.15. In addition to that, the h is used instead of writing in z in order to avoid confusion between the aerodynamic lag states and heave states.

It is found evident from Subchapter 2.2 that the aerodynamic lag affects the equations of motion for each wing section. Following the derivation of Leishman state space, then it is possible to expand the aerodynamic lag variable matrix to be integrated into three-dimensional modeling. The integration of Leishman state-space adds the wing states with four additional lag states. Two states are the contribution of wake lag due to the angle-of-attack or pitch [14] of the aircraft while the rest is contribution due to the angle of the flap to

the global angle of the main wing structure. Hence, the additional influence due to the circulatory lift can be derived from the two-dimensional wing solution in Equation 2.21 into a three-dimensional solution as

$$\begin{aligned}\begin{bmatrix} M_\alpha^c \\ Z^c \end{bmatrix} &= K_z z_i \\ &= \begin{bmatrix} \frac{1}{2}\rho V^2 S(b(\frac{1}{2}+a))(4\pi\frac{b_1 b_2}{2}(\frac{V}{b})^2) & \frac{1}{2}\rho V^2 S(b(\frac{1}{2}+a))(A_1 b_1 + A_2 b_2)(\frac{V}{b}) \\ \frac{1}{2}\rho V^2 S(4\pi\frac{b_1 b_2}{2}(\frac{V}{b})^2) & \frac{1}{2}\rho V^2 S(A_1 b_1 + A_2 b_2)(\frac{V}{b}) \end{bmatrix} \begin{bmatrix} z_1 \\ z_2 \end{bmatrix} \\ &+ \begin{bmatrix} \frac{1}{2}\rho V^2 S(b(\frac{1}{2}+a))\pi & \frac{1}{2}\rho V S(b(\frac{1}{2}+a))^2\pi \\ \frac{1}{2}\rho V^2 S(b(\frac{T_{12}}{2\pi}))\pi & \frac{1}{2}\rho V S(b(\frac{T_{12}}{2\pi}))(b(\frac{1}{2}+a))\pi \\ \frac{1}{2}\rho V^2 S\pi & \frac{1}{2}\rho V S(b(\frac{1}{2}+a))\pi \end{bmatrix} \begin{bmatrix} \alpha \\ \dot{\alpha} \end{bmatrix}\end{aligned} \tag{2.25}$$

Here it can be seen again that the aerodynamic interaction with the structure also influences the angular attitude and rate of the wing and also aileron. Hence it can be hypothesized that the aerodynamic and structural parameters influence these two states as seen on the second matrix on the right side of the equation above.

2.3.1 In-house PROTEUS Aeroelastic Geometry Generator

PROTEUS is an in-house aeroelastic framework for optimization and tailoring, which is owned by the Department of Aerospace Structures and Materials [37]. Developed initially by de Breuker [13], the in-house software has been used to generate the geometry of multiple aeroelastic objects for the needs of scientific experiments. The software is designed to improve the conceptual design of aircraft wings with the reference of its sizing and aeroelasticity. The optimized results yield a numerical three-dimensional wing structure matrices split into several two-dimensional wing elements with matching cross-sectional properties [37]. The resulting matrices are the geometric mass and stiffness matrix, which represents the dynamics of the wing in six degrees of freedom. The interested readers can find the theoretical and computational process knowledge of the software in the works by Werter and de Breuker ([80],[79]).

2.3.2 Final Equation and Concluding Remarks

Given the structural mass and stiffness matrices are obtained from the in-house PROTEUS software, the equation of motion of three-dimensional wing can then be derived. As mentioned in the preceding subsection, the three-dimensional wing solution is obtained by dividing the geometry into several two-dimensional wing components whose dynamics is governed by Equation 2.11. While the stiffness and mass can be obtained directly from PROTEUS, the structural damping matrix representing the dampened nature of the wing movement has not existed yet. One way to generate the matrix is by manually choosing the damping coefficient. From [2], it is reported that the damping coefficient of a wing is found between 0 and 0.05 with a natural frequency as derived in Equation 2.7. Hence the damping matrix can be obtained based on PROTEUS results.

Considering the full picture of aeroelastic displacement model due to structural and aerodynamic influence, it is then now possible to make the full mathematical model of the aeroelastic wing. Let the mass and stiffness matrix generated by in-house PROTEUS software is represented as M_s and K_s. The simulated damping matrix is represented as C_s. The M_{ws}, C_{ws} and K_{ws} will represent the part of respective M_s, C_s and K_s matrices that constitute of the dynamics of the wing section's degree of freedom parameters related to all states of the equation, represented as x_a. This leaves the full model with the remaining aerodynamic lag influence is calculated based on the derivation of Leishman State-Space as derived in Section 2.2. However, as the Leishman aerodynamic lag influence only states the significant influence in the two-dimensional problem, therefore only aerodynamic lag influence in heave and pitching of the wing section exists. Furthermore, since the free velocity of air is close to zero, hence implementing the aerodynamic lag parameter K_z in the roll and yaw axis will yield negligible parameter value.

Thence, for each wing section, the full mathematical model becomes

$$\begin{bmatrix} M_\phi \\ M_\alpha \\ M_\psi \\ F_x \\ F_y \\ F_z \end{bmatrix} = M_{ws}\ddot{x}_a + C_{ws}\dot{x}_a + K_{ws}x_a + \begin{bmatrix} 0 & 0 \\ \frac{1}{2}\rho V^2 S(b(\frac{1}{2}+a))(4\pi\frac{b_1 b_2}{2}(\frac{V}{b})^2) & \frac{1}{2}\rho V^2 S(b(\frac{1}{2}+a))(A_1 b_1 + A_2 b_2)(\frac{V}{b}) \\ 0 & 0 \\ 0 & 0 \\ 0 & 0 \\ \frac{1}{2}\rho V^2 S(4\pi\frac{b_1 b_2}{2}(\frac{V}{b})^2) & \frac{1}{2}\rho V^2 S(A_1 b_1 + A_2 b_2)(\frac{V}{b}) \end{bmatrix} \begin{bmatrix} z_{1,i} \\ z_{2,i} \end{bmatrix}$$
$$+ \begin{bmatrix} 0 & 0 \\ \frac{1}{2}\rho V^2 S(b(\frac{1}{2}+a))\pi & \frac{1}{2}\rho V S(b(\frac{1}{2}+a))^2\pi \\ 0 & 0 \\ 0 & 0 \\ 0 & 0 \\ \frac{1}{2}\rho V^2 S\pi & \frac{1}{2}\rho V S(b(\frac{1}{2}+a))\pi \end{bmatrix} \begin{bmatrix} \alpha_i \\ \dot{\alpha}_i \end{bmatrix} \tag{2.26}$$

where $z_{1,i}$ and $z_{2,i}$ represents the aerodynamic lag states belonging solely to the corresponding wing section and $\dot{\alpha}_i$ and α_i are displacement attitude and rates are belonging solely to the corresponding i^{th}-wing section.

Concluding Remarks

As the full picture of the aeroelastic phenomenon in fluttering conditions has been described, it is clear to the writer and the readers about the dynamics and the states that will be estimated by using the state estimation routine. Hence, the first sub-research question (RQ 1.1) is finally obtained with the formation of the final equation. This state estimation routine will be further explained and built up in Chapter 3.

Chapter 3

System Identification of Aeroelastic Wing

Given the knowledge of the flexible equations of motion that governs the flexible wing and approaches that can be useful in constructing the full 3D model of the wing and correlation among the states and variables on the aeroelastic system, it is now possible to determine the dynamics of the wing by performing the state space calculations based on the state space derived from the final equation of previous chapter.

As described in the introduction chapter, the proposed methods are by coupling the state estimator with visual tracking. Visual tracker enables the determination of the displacement of an object by tracking the object of interest in every single image patch on the image sequence (video). Furthermore, the coupling with a state estimation routine will further enhance the quality of visual tracking by providing the position and displacement estimation of the objects of interest during occlusion. The state estimator also simultaneously estimates the dynamics of the object of interest, namely, in this case, aeroelastic structure or wing. In order to identify the system that governs the dynamics of the wing, the structural system identification has been developed in the civil engineering field that enables the states and parameters real-time estimation. The online structural system identification methods are going to be used as the ideal starting point to derive a suitable method for aeroelastic wing system identification.

3.1 State of the Art

In order to reconstruct the aeroelastic fluttering dynamics, the system identification will be conducted in order to observe the displacement of the wing section and to estimate the parameters of the aeroelastic system, namely structural stiffness, damping, and mass. From here, the validation can be run against either the original numerical model of the wing or the tracked displacement of the wing (ground truth). In dealing with the flexible structure estimation problem, Ghanem and Shinozuka identify three main real-time identification methods to solve the flexible-structure system ([22], [72]). These are Kalman Filter, Maximum Likelihood Estimation, and Recursive Least Squares. Out of these proposed methods, it is observed that Kalman Filter and Maximum Likelihood Estimation yield more reliable computational results in comparison to the standalone Recursive Least Square. Furthermore, the Recursive Least-Square approach cannot by itself solve the displacement and aerodynamic states of the wing. Therefore, the two remaining methods, namely Kalman Filtering and Maximum Likelihood Estimation, will be discussed further.

3.2 Kalman Filtering

Kalman Filter is one of the methods of state estimation that can be used recursively for an online estimation routine. Kalman Filter was developed in the 1960s with the goal of cleaning out the measurement and process noise, which may cause erroneous readings of the states in a linear system [41]. The linearity of a system can be determined from the nature of coupling among the states considered in the equation. By tracing back to the final equation of the mathematical model of an aeroelastic wing, it can be seen that each state is coupled by stiffness, damping, and mass. Therefore, it can be seen that nonlinearities do not exist in the equation. The algorithm of the Ordinary or Linear Kalman Filter can be written as follows.

1. At the first iteration, declare the initial state and covariance estimation

$$\begin{aligned} \underline{\hat{x}}_{0,0} &= \underline{\hat{x}}_0 \\ P_{0,0} &= P_0 \end{aligned} \tag{3.1}$$

2. Calculate "one-step-ahead" prediction in discrete form

$$\underline{\hat{x}}_{k+1,k} = \Phi_{k+1,k}\underline{\hat{x}}_{k,k} + \Psi_{k+1,k}\underline{u}_k \tag{3.2}$$

3. Calculate covariance matrix of state prediction error

$$P_{k+1,k} = \Phi_{k+1,k})P_{k,k}\Phi_{k+1,k}^T + \Gamma_{k+1,k})Q_{d,k}\Gamma_{k+1,k}^T \tag{3.3}$$

4. Update states' measurements

$$\underline{\hat{x}}_{k+1,k+1} = \underline{\hat{x}}_{k+1,k} + K_{k+1}(\underline{z}_{k+1} - H_{k+1}\underline{\hat{x}}_{k+1,k}) \tag{3.4}$$

5. Calculate covariance matrix of state estimation error

$$P_{k+1,k+1} = (I - K_{k+1}H_{k+1})P_{k+1,k} \tag{3.5}$$

6. Return to the Step 2 for the next iteration.

Kalman Filter is also computationally a cheaper state estimation compared to its counterpart, Particle Filter. The Particle Filter is one of a kind of Bayesian Recursive filter based on random sampling ([10],[68]). However, the random sampling is not bounded by certain distribution as happened in Kalman Filter [1]. That results in a low sampling rate created from a more computationally expensive routine and significantly lower processing rate [61]. This is exemplified by its implementation in visual tracking ([49] [50] [9] [4]).

Furthermore, the application of the Kalman Filter is not only limited to state estimation. Few applications of Kalman Filtering for parameter estimation have been shown to be working in the field of civil engineering to estimate the dynamics of the flexible structure of building during an earthquake [84], of vehicle model [7], and also the health monitoring of the structure as already performed by Wu et al. [82] by using Unscented Kalman Filter and Xie et al. by using Extended Kalman Filter [83]. The typical structure identification analysis has already been conducted to estimate the damping and stiffness parameters along with the displacement of the body by augmenting the state space with parameter estimation such that [33]

$$\begin{aligned} \dot{C} &= 0 \\ \dot{K} &= 0 \end{aligned} \tag{3.6}$$

Nevertheless, despite the Kalman Filter routine can estimate aeroelastic constant parameters directly in one step, augmenting the Kalman Filter state-space will then introduce the nonlinearities to the problem. Hence the ordinary Kalman Filter routine is no longer applicable to solve the problem. Although further researches have been conducted in order to increase the capability to measure non-linear systems such as Extended Kalman Filter [42], Iterated Extended Kalman Filter [85], Unscented ([40], [78]), and Iterated Unscented Kalman Filter [85], the computational cost becomes significantly higher compared to the Ordinary Kalman Filter routine due to nonlinearities. Moreover, by augmenting the Kalman Filter state space to solve the three-dimensional aeroelastic wing with six degrees of freedom, the augmentation adds the number of states to estimate by $108n^2$ states on top of the number of displacement states. Therefore, for every n wing sections as the results discretization of three-dimensional wing geometry, the total number of states to estimate will be in the order of at least hundreds. Although not all parts of the mass, damping, and stiffness matrix need to be estimated, it can be seen that the routine is already quite complicated. Furthermore, the number of states involved requires a high processing rate in order to enable high rate system identification. Therefore, augmenting the Kalman Filter is not suitable for the case where the aeroelastic structure is presentable in linear state-space.

3.3 Maximum Likelihood Estimation

the Maximum Likelihood Estimator (MLE) is a non-linear estimator based on the assumption that an unknown probability density function (PDF) exists on the set of observation where

$$f_N(y,\mu,\varsigma) = \frac{1}{\varsigma\sqrt{2\pi}} exp(-\frac{(y-\mu)^2}{2\varsigma^2} \tag{3.7}$$

Where N represents the number of observation points.

MLE is a special case of Bayes rule where probability density and cost function where the error estimate is available [65]. Given that each of the observation points is independent and identically distributed. The likelihood cost function is

$$L(y|\theta) = \Pi_{i=1}^{N} f(y(i)|\theta) = f(y(1)|\theta) + f(y(2)|\theta) + ... + f(y(N)|\theta) \tag{3.8}$$

Where $f(y(i)|\theta)$ represents the distribution function for each observation points.

Given that maximum likelihood has an objective to increase the likelihood of the estimator, the cost function value has to be maximized. In the parameter model structure, by assuming that y is normally distributed and the mean of the function is equal to $\mu = A(x)\theta$, therefore

$$L(y|\theta) = \frac{1}{2\pi^{N/2}}\sqrt{|\Sigma(\theta)|} exp(-\frac{1}{2}(y-A(x)\theta)^T\Sigma(\theta)^{-1}(y-A(x)\theta)) \tag{3.9}$$

As the maximum likelihood estimator is not influenced by natural logarithmic as it is monotonely increasing, then

$$\begin{aligned} \hat{\theta}_{MLE} &= arg\ max_\theta\ L(y|\theta) \\ &= argmax_\theta\ lnL(y|\theta) \\ &= arg\ max_\theta\ [ln2\pi^{N/2}\sqrt{|\Sigma(\theta)|} + \frac{1}{2}(y-A(x)\theta)^T\Sigma(\theta)^{-1}(y-A(x)\theta)] \end{aligned} \tag{3.10}$$

Nevertheless, the covariance matrix is still becoming a problem in this case since it needs to acquired initially before the calculation. By using relaxation technique ([43]), the covariance matrix can then be simplified by approximating it for each additional measurement point k such that the MLE estimator can be rewritten as

$$\hat{\theta}_{k+1} = arg\ max_\theta[ln2\pi^{N/2}|\hat{\Sigma}(\hat{\theta}_k,k)|^{1/2} + \frac{1}{2}(y(\hat{\theta}_k,k) - p(\hat{\theta}_k,k))^T\hat{\Sigma}(\hat{\theta}_k,k)^{-1}(y(\hat{\theta}_k,k) - p(\hat{\theta}_k,k))] \tag{3.11}$$

Given that the general least-squares estimator is a maximum likelihood estimator if the covariance matrix is not a function of the parameters, then

$$\begin{aligned} \hat{\theta}_{ML} &= arg\ max_\theta\ [ln2\pi^{N/2}\sqrt{|\Sigma(\theta)|} + \frac{1}{2}(y-A(x)\theta)^T\Sigma(\theta)^{-1}(y-A(x)\theta)] \\ 0 &= \frac{\partial}{\partial\theta}[ln2\pi^{N/2}\sqrt{|\Sigma|} + \frac{1}{2}(y-A(x)\theta)^T\Sigma^{-1}(y-A(x)\theta)] \\ &= \frac{\partial}{\partial\theta}[\frac{1}{2}(y-A(x)\theta)^T\Sigma^{-1}(y-A(x)\theta)] \end{aligned} \tag{3.12}$$

Based on these relaxation techniques, it had been proven that the covariance matrix to reduce to all other least squares estimators.

In order to achieve a maximum likelihood estimated values, three variation methods can be applied, namely: Output Error, Filter Error, and Equation Error [25]. First, the Output Error is a simplification technique to achieve a maximum likelihood estimation. However, in this method, the assumption is that no process noise occurs. On the other hand, the Equation Error is also a simplification but with the measurement noise neglected. While the estimation problem can be reduced to an ordinary least square problem, this method requires additional techniques to remove noise from the explanatory variables to obtain unbiased solutions. The Filter Error is the method without further simplification by accounting for the measurement and process noise into the equation, hence yielding an unbiased estimation [25] [64].

3.4 Two-Step Method of System Identification

Mulder [56] had proven that the Filter Error Method could then be divided into two parts where the flight path needs to be firstly reconstructed. Then the Least Square routine can then be used in order to obtain the actual parameters as the noises occurring in the system have been cleared up by the Kalman Filter routine. In this visual tracking case, the Kalman Filter, which wipes out the measurement and process noise effects are embedded in the visual tracker system and sensor. The states of displacement of the wing object of interest as the results of the Kalman Filter will be unbiased, and a simple Least Square routine can then be introduced in the next step to identify the parameters.

Nevertheless, the option of using the least-square estimation is marred with the error that may occur in the condition of the higher-order polynomial equation where the error value can overshoot more after passing through parameter estimation using least squares regression in the second step in the Two-Step Method. Furthermore, the small error that occurs during the estimation of the objects of interest's displacement may accumulate when the states are derived to obtain the velocity and acceleration for the displacement. This phenomenon is called as Runge's phenomenon [69]. That can be mitigated by chopping the time window of the simulation, which limits the deviation due to accumulative error over time. Therefore, the parameters need to be estimated recursively. This is also one of the properties of an online-based parameter estimator. Nevertheless, at the first time window, an offline based parameter estimation needs to be carried out.

3.5 Least Square Parameter Estimation

3.5.1 Least-Square Offline Estimators

The offline least-square estimator is based on the basic least-square methods which have a non-iterative and analytical solution. The common Least Square problem is solved based on the regression problem where

$$A\theta + e = y \tag{3.13}$$

where A is the estimated state regression matrix that contains the displacement states of the structure such as acceleration, velocity, and position displacement. θ contains the corresponding parameters of mass, damping, and stiffness. e represents the output error, and y represents the external acting aerodynamic forces and moments.

Over time, the least square method has been developed in order to approximate the increasingly nonlinear behavior of a system [51]. The objective of the estimator itself is to achieve such that the approximation of the estimated function is minimum in error compared to the real model. That is called as the best linear unbiased estimator (BLUE) formulated as

$$B\{\hat{\theta}\} = E(\hat{\theta}) - \theta = 0 \tag{3.14}$$

Where B represents the difference between the estimated parameter value and the real value [3]. Ordinary least square (OLS) is a basic linear parameter estimator which is then formulated with this goal as

$$\hat{\theta}_{OLS} = (A^T(x)A(x))^{-1}A^T y \tag{3.15}$$

However, OLS is plagued with high inaccuracies when the state's measurement is variant in terms of magnitude as well as noise realizations. Hence, an estimator's noise sensitivity modification is derived out of the covariance of the estimated states calculated through OLS. The covariance of the least-square method itself is formulated as

$$Covar\hat{\theta}_{OLS} = (A^T(x)A(x))^{-1} \tag{3.16}$$

from which the weight matrix (W) of the states can be composed out of variance of each state on the system is tabulated as

$$Var\{\hat{\theta}_{OLS}\} = diag(Covar_{\{}\hat{\theta}_{OLS}\}_{11}, Covar\{\hat{\theta}_{OLS}\}_{22}, ..., Covar_{\{}\hat{\theta}_{OLS}\}_{NN}) \tag{3.17}$$

where N represents the number of state inside the system.

Given that the least square method cost function has an optimum at zero, then the Weighted Least Square can be formulated as

$$\hat{\theta} = (A(x)(W^{-1})A(x)^T)^{-1}A(x)^T(W^{-1})y \tag{3.18}$$

In this way, the new least square method called Weighted Least Square method is found [3]. The realization of the system function while then be less dependent to the changing noise realization with smaller noise residuals.

A more advanced least-square estimation can be derived from the calculation using the same method as derivation as the Weighted Least-Square method. The Generalized Least-Squared is the development from the Weighted Least-Square, where the new weighting matrix (Σ) is a covariance matrix obtained in the Ordinary Least Square method. Therefore,

$$\hat{\theta} = (A(x)(\Sigma)^{-1})A(x)^{T})^{-1}A(x)^{T}(\Sigma)^{-1})y \tag{3.19}$$

3.5.2 Online Least-Square Estimator: Recursive Least Squares

One way to circumvent the Runge's phenomenon while keeping the computation cost low by using Least Squares is by using online calculation. In that case, the global data is chopped into the iteration time window, and the parameter estimation is recursively updated. Recursive least square is a modification of ordinary least square or weighted the least square, which incorporates the iteration of the solution, which in turn yields a global solution based on the weighting of the new data from a time window with the other regression results from previous time windows [52]. While it is inferred that recursive least-squares yield less reliable results of parameter calculation compared to the other two methods, the reliability of the results can be further improved by introducing a weighing factor (λ) [72]. The forgetting factor is chosen between 0 and 1, with one indicates that the old data from older iterations are entirely forgotten while the smaller number signifies the heavier weighting for older data. Based on the indication from Goodwin and Payne [24], the forgetting factor is recommended to be 0.99, and Ghanem and Shinozuka further confirm the results [72]. Initially, the parameter value is obtained through the offline least-square estimator, as described above. In the next time window, with the presence of the forgetting factor, the RLS weights more to the new data compared to the weight of old data. Therefore yielding a more accurate update of approximation of the parameter with the new set of data in any time window. At the first iteration, the initial parameter and covariance estimation matrix as

$$\begin{aligned} \underline{\hat{\theta}}_{0,0} &= \underline{\hat{\theta}}_{0} \\ P_{0,0} &= P_0 \end{aligned} \tag{3.20}$$

Then, the new state measurement values from the Kalman Filter routine ((z_{k+1}, u_{k+1})) are obtained. The former represents the estimated measurement of displacement attitude and rate states, and the latter represents inputs to the mathematical model. The u_{k+1}) becomes the output matrix while the regression matrix for new data points (a_{k+1}) is formulated based on the measured states.

Next, the calculation of least-square with forgetting factor can then be performed. First, the Kalman Gain of RLS is calculated as

$$K_{k+1,RLS} = P_k \cdot a_{k+1}^{T}(a_{k+1}P_k a_{k+1}^{T} + \lambda)^{-1} \tag{3.21}$$

and parameter values as

$$\hat{\theta}_{k+1} = \hat{\theta}_k + K_{k+1,RLS}(u_{k+1} - a_{k+1}\hat{\theta}_k) \tag{3.22}$$

For the next iteration, the new force and moment data will become the new output matrix, and the measured states are formed in the shape of the regression matrix. The updated parameter covariance matrix is formulated as

$$P_{k+1} = P_k - K_{k+1,RLS}a_{k+1}P_k \tag{3.23}$$

3.6 Fitting the Large System for High Rate Computation

Given the routine of system identification, as mentioned above, and the mathematical model of the aeroelastic wing, it is now possible to execute the system identification process. Given that the aeroelastic parameters are known, it will be seen that the number of states involved for a rigid wing will be the number of degrees of freedom. However, in order to render the state-space solvable, the state-space will expand to solve double the number of degrees of freedom in each wing section. This is caused by the nature of the second-order equation of the spring-mass-damper model. For an aeroelastic wing, monitoring is calculated based on a discretized wing with 6 degrees of freedom. For a certain n number of wing sections, the state-space will then have to solve $12n$ states. Moreover, the aerodynamic lag due to circulatory trailing wake is also discretized into the

number of wing sections. This will add $2n$ states to solve on top of the other displacement states. Therefore, it can be seen that the number of states rapidly increases. The bigger the system is, then the more expensive the computation cost is. This will, in turn, affect how fast the calculation can be done for the supposedly fast system.

One way to circumvent the mentioned problem is by reducing the number of states through a model order reduction techniques. In the big picture, the basis of the model order reduction technique is conducted in two steps. Firstly, the original model is transformed into other state-space representations from which the order of the system can then be reduced while maintaining the behavior of the original system. The reduction is based on the ranking of the influence of the states. Therefore by discarding the states with minuscule influence while retaining the states with significant influence, the goal is expected to be achieved.

Gillebaart and de Breuker [23] has tabulated and reviewed the four most popular model order reduction to solve unsteady aerodynamics state-space. In another paper by Besselink et al. [5], few other methods are presented and reviewed for its application in structural dynamics, numerical computation, and in control. The two papers provide the methods of model order reduction, these are:

1. Modal truncation (MT) ([12],[28]),
2. Balanced truncation (BT) [55],
3. Proper Orthogonal Decomposition (POD) [32],
4. Balanced Proper Orthogonal Decomposition (BPOD) ([81],[67]), and
5. Krylov subspace model order reduction (KMOR) ([59],[70]).

Based on the results and conclusion of the two papers, it is found that the MT and KMOR method (named otherwise as moment matching method) is computationally cheaper compared to the BT method. This is further approved by Gillebaart and de Breuker that BT is computationally the costliest among the presented methods, despite it is limited to use BT for a moderate-sized problem. However, BT and MT are more reliable since it guarantees the preservation of the stability of the true model in the reduced state-space realizations. Furthermore, the BT method is also bounded by apriori error criteria. These characteristics are not possessed by other methods that their results' accuracy needs to be investigated further [5]. The remaining POD and BPOD model reduction methods also yield accurate results. However, the error margin, which bounds the balanced realization error of BPOD, needs to be fine-tuned. The error margin tuning makes the method less robust, while POD does not guarantee the stability of its true state-space [23]. The BT method is very robust in characteristics as the method requires no input other than the required order of the ROM; this makes the method one of the most widely used model reduction methods. Although computationally costlier, since the number of the states introduced in this report is in order of 10^2 and computed before the implementation of the Two-Step Method, the BT computational cost is acceptable [26]. The method preserves the stability of the full high-order model and maintains the reduced model within a priori error bound.

Moore [55] delivers the first balanced truncation algorithm. In short, balanced truncation is a technique that reduces the order of the model based on the energy or Hankel singular values of the system's controllability and observability Gramian values [46]. An example of representation of the Hankel singular values can be seen as in the following Figure 3.1.

Hankel Singular Values or HSV is essentially the diagonal part of a singular matrix obtained from the singular value decomposition that will later be described in this section. The largest singular value does not necessarily belong to the first state in the state order. The HSV shows the contribution of one state from the lowest to the largest, as shown in the graph. The idea is by discarding the states with low energy and retaining the states with high energy. The actual model can be represented with a fewer number of states but still represent the behavior of the true model.

The computational process of Moore's balanced truncation is formulated as follows.

1. Define the linear system state space as

$$\begin{aligned} \dot{\mathbf{x}} &= \mathbf{A}x + \mathbf{B}u \\ \mathbf{y} &= \mathbf{C}x + \mathbf{D}u \end{aligned} \tag{3.24}$$

2. Solve the observability Gramian matrix (W_o) and controlability Gramian matrix (W_c) by solving the Lyapunov equations

$$\begin{aligned} \mathbf{A}W_c + W_c\mathbf{A}^* + \mathbf{B}\mathbf{B}^* &= 0 \\ \mathbf{A}^*W_o + W_o\mathbf{A} + \mathbf{C}^*\mathbf{C} &= 0 \end{aligned} \tag{3.25}$$

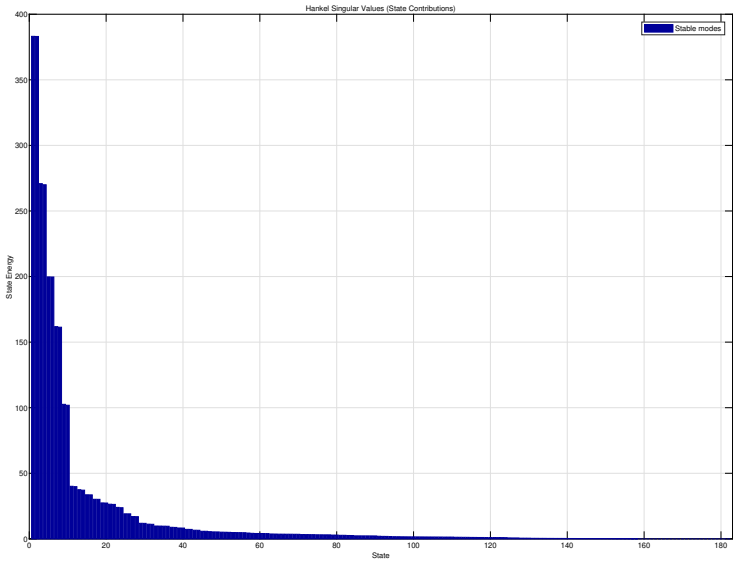

Figure 3.1: Hankel singular values of states of a system.

3. Find the balanced representation **P** and **Q** from the decomposition of obtained controlability and observability Gramian matrix from Step 2 respectively by using Cholesky decomposition (in MATLAB environment, the Step 2 and 3 can be automatically solved with command "*lyapchol*") such that

$$\begin{aligned} W_c &= \mathbf{P}\mathbf{P}^T \\ W_o &= \mathbf{Q}^T\mathbf{Q} \end{aligned} \tag{3.26}$$

4. Given the matrix $\mathbf{H} = \mathbf{Q}\mathbf{P}$, perform the singular value decomposition of the matrix such that

$$\mathbf{H} = \mathbf{V}\mathbf{S}^2\mathbf{U}^T \tag{3.27}$$

where $\mathbf{V}^T\mathbf{V} = I$ and $\mathbf{U}^T\mathbf{U} = I$ and **S** is Gramian positive semi-definite diagonal matrix.

5. Calculate the transformation matrix and its inverse, where

$$\begin{aligned} \mathbf{T} &= \mathbf{P}\mathbf{U}\mathbf{S}^{-1} = \mathbf{Q}^{-1}\mathbf{V}\mathbf{S} \\ \mathbf{T}^{-1} &= \mathbf{S}\mathbf{U}^T\mathbf{P}^{-1} = \mathbf{S}^{-1}\mathbf{V}^T\mathbf{Q} \end{aligned} \tag{3.28}$$

6. Obtain the balanced representation of state space matrices as

$$\begin{aligned} \bar{\mathbf{A}} &= \mathbf{T}^{-1}\mathbf{A}\mathbf{T} \\ \bar{\mathbf{B}} &= \mathbf{T}^{-1}\mathbf{B} \\ \bar{\mathbf{C}} &= \mathbf{C}\mathbf{T} \\ \bar{\mathbf{D}} &= \mathbf{D} \end{aligned} \tag{3.29}$$

7. Consider the model reduction to be conducted for the balanced state space (Step 6). Separate the state matrix into

$$\bar{x} = \begin{bmatrix} \bar{x}_1 & \bar{x}_2 \end{bmatrix} \tag{3.30}$$

where $\bar{x}_1$ represents the states to be kept in the reduced model. Then the state space matrices are

partitioned accordingly as

$$\begin{aligned}\bar{\mathbf{A}} &= \begin{bmatrix}\bar{\mathbf{A}}_{11} & \bar{\mathbf{A}}_{12}\\ \bar{\mathbf{A}}_{21} & \bar{\mathbf{A}}_{22}\end{bmatrix}\\ \bar{\mathbf{B}} &= \begin{bmatrix}\bar{\mathbf{B}}_1\\ \bar{\mathbf{B}}_2\end{bmatrix}\\ \bar{\mathbf{C}} &= \begin{bmatrix}\bar{\mathbf{C}}_1 & \bar{\mathbf{C}}_2\end{bmatrix}\\ \bar{\mathbf{D}} &= \bar{\mathbf{D}}\end{aligned} \tag{3.31}$$

Hence the balanced truncated model (reduced state space model) becomes

$$\begin{aligned}\mathbf{A}_{red} &= \bar{\mathbf{A}}_{11}\\ \mathbf{B}_{red} &= \bar{\mathbf{B}}_1\\ \mathbf{C}_{red} &= \bar{\mathbf{C}}_1\\ \mathbf{D}_{red} &= \bar{\mathbf{D}}\end{aligned} \tag{3.32}$$

In the algorithm of balanced truncation above, it can be ensured that the reduced model will maintain the stability of the original model and give a realization within the range error formulated as

$$\sigma_{r+1}^{H} \leq ||\mathbf{G} - \mathbf{G}_{red}||_{\infty} < \sum_{k=r+1}^{N} \sigma_k^H \tag{3.33}$$

Nevertheless, the realization is applicable for an infinite range frequency and for infinite time-domain data, which is unachievable in practice. Consequently, the classical Gramians are only approximations to the quantities that describe any physical system [21]. In other words, the reduced model representation only best approximates the true model response with a number of states close to the full one. This can be observed from the model reduction using Moore's balanced truncation in the following figures. The figures are obtained from a balanced truncation of the full aeroelastic wing example.

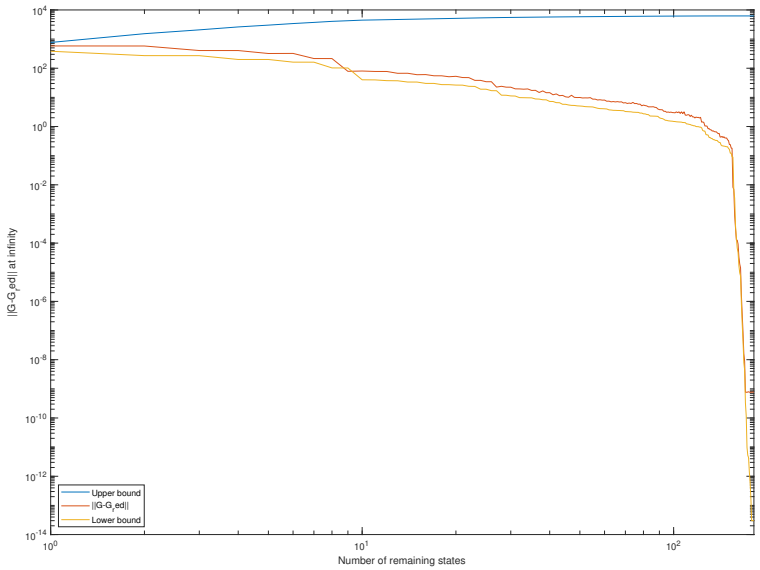

Figure 3.2: Balanced truncation error bound of the simulated aeroelastic wing.

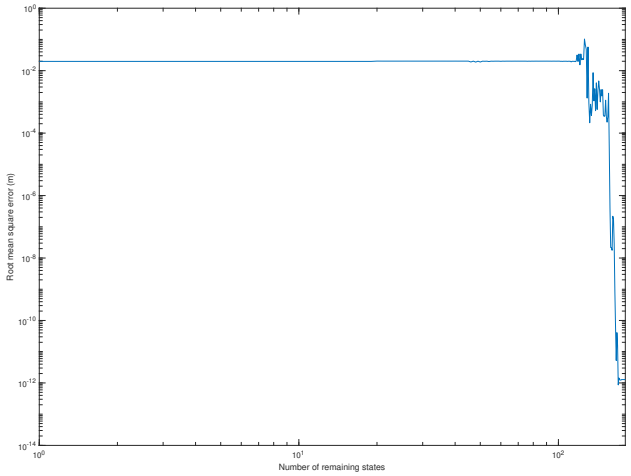

Figure 3.3: Heaving attitude of tip wing section's mean-square error of reduced full wing state-space against.

It can be seen from Figure 3.2 that the error resulted from Moore's balanced truncation is bounded in accordance with Equation 3.33. However, when the singular value (or Hankel singular value) of the transformed system is very high), this will also drive the reduced-order model to have a significant error value. Furthermore, in many cases, some measurement tools can only work at a specific range of frequency. This can translate to the system's inability to capture the frequency of faster modes. From here, the idea was conceived to approximate the bending and torsion modes of the wing in limited frequency. It will, in turn, give birth to the frequency-limited model reduction method based on the balanced truncation method founded by [55].

3.7 Frequency-Limited Model Reduction

The first attempt was taken by weighting the frequency range in the balanced truncation method by Enns [17]. The method is then further simplified by Gawronski and Juang, which removes the necessity of manually weighting the frequency range by using frequency-domain Gramian representation [21]. Based on Gawronski-Juang's algorithm. First, the controllability and observability Gramians for the full system is obtained by solving the Lyapunov equation from which the Gramian matrices value at upper and lower frequency limit. It is followed by the calculation of Gramian matrices at the frequency bandwidth. The Gramian matrices are then factorized using Cholesky decomposition. Hence the transforming matrix can then be obtained through the same step as Moore's balanced truncation method.

However, the frequency-limited controllability and observability Gramians of Gawronski et al.'s are not guaranteed to be positive definite. This condition is because the controllability and observability Gramian matrices of Gawronski-Juang's method is not guaranteed to be positive definite. In the meantime, the positive definite matrix is a prerequisite in order to make Cholesky decomposition successful. This disables the routine to perform the Gramian decomposition. As consequence, the stability of the reduced model cannot be guaranteed ([27],[76]). Furthermore, Gawronski and Juang also do not guarantee the error bound of the reduced model. Despite an attempt to condition the observability and controllability Gramian matrices to be positive semidefinite such as Higham's method [31], this nevertheless gives unsuccessful results when performing the model reduction. This is found evidence by performing balanced truncation, as shown in the following Figure 3.4.

3.7.1 Modified Frequency-Limited Model Reduction Routine

The problem of the balanced realization in a limited frequency range then becomes the basis for Gugercin and Antoulas [27]. It is proposed that the solution to the non-positive definite controllability (W_c) and observability (W_o) Gramian matrices can be solved by performing the eigenvalue decomposition (EDV) for both matri-

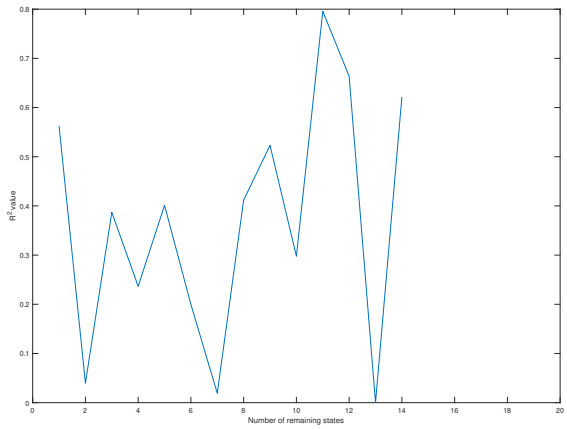

Figure 3.4: Failing model reduction of a 182-states full model by using the Gawronski-Juang method is signified by the broken line at a random range of reduction order of states. The model order reduction at a higher number of states are automatically not displayed due to the instability caused by reduction.

ces. This results in the singular value for each Gramian matrices. Simultaneously the rank of each Gramian matrix is also counted. The information is then used to rebuild the namely $\hat{\mathbf{B}}$ and $\hat{\mathbf{C}}$, which is the multiplication of the left-singular value and a new matrix built of the square root of the absolute singular matrix of both Gramian up to aforementioned matrix rank and zero for the remaining row. Hence the new matrix has positive semi-definite characteristics. This allows the Cholesky decomposition solution to be obtained.

Another innovation made in the Gugercin-Antoulas method is by solving the factorization through the solution of the Lyapunov equation such that the Cholesky decomposition of the solution exists, given the calculated $\mathbf{A}, \hat{\mathbf{B}}$ and $\hat{\mathbf{C}}$ matrices (MATLAB command: "*lyapchol*"). Based on this method, the norm error of the gain between the original model and reduced model through balanced truncation at infinite frequency will theoretically be governed in the same way as Moore's balanced truncation norm error. Because the total energy of the system at the frequency range of interest will be smaller compared to the norm error of Moore's balanced truncation, the error between the norm of the frequency-limited model and the original model will be lower compared by using Moore's BT method. The statement is exemplified in the following figure.

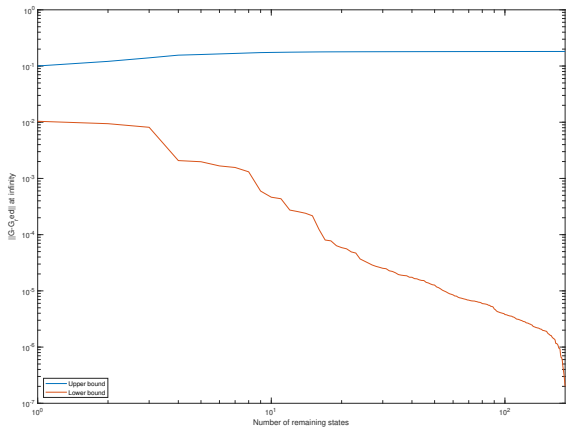

Figure 3.5: Balanced truncation error bound of modified frequency-limited Gawronski-Juang balanced truncation of the simulated aeroelastic wing.

It can be seen that the error range is at smaller orders, as seen in Figure 3.2 that the error bound of the

reduced model using the modified Gawronski-Juang method at smaller orders is almost equal to the reduced model of the higher number of states obtained by Moore's balanced truncation model. Therefore, the modified Gawronski-Juang's frequency-limited balanced truncation method can then be formulated as follows.

1. Establish the lower and upper bound of frequency limit $[\omega_1, \omega_2]$,
2. Obtain controlability and observability Gramian matrix for all frequency by solving the Lyapunov equation [55],
3. Calculate the $S(\omega)$ term for lower and upper bound of frequency limit [21], formulated as

$$S(\omega) = \int_{-\omega}^{\omega} H(v)\frac{dv}{2\pi} = \frac{j}{2\pi} ln((j\omega I + \mathbf{A})(-j\omega I + \mathbf{A})^{-1} \tag{3.34}$$

4. Determine controlability and observability Gramian at lower and upper bound frequency ($W_c(\omega_1)$, $W_c(\omega_2)$, $W_o(\omega_1)$, $W_o(\omega_2)$) where

$$\begin{aligned} W_c(\omega) &= W_c S^*(\omega) + S(\omega) W_c \\ W_o(\omega) &= S^*(\omega) W_o + W_o S \end{aligned} \tag{3.35}$$

5. Calculate the frequency-limited Gramian matrices, formulated as

$$\begin{aligned} W_c(\Omega) &= W_c(\omega_2) - W_c(\omega_1) \\ W_o(\Omega) &= W_o(\omega_2) - W_o(\omega_1) \end{aligned} \tag{3.36}$$

6. Identify the rank of $W_c(\Omega)$ as ρ_{W_c} and the rank of $W_o(\Omega)$ as ϱ_{W_o} Perform eigenvalue decomposition of frequency limited Gramian matrices [27] such that

$$\begin{aligned} W_c(\Omega) &= \mathbf{M}\Lambda\mathbf{M}^T\ ,\ \Lambda = diag(\sigma_{c1}, \cdots, \sigma_{cN}) \\ W_o(\Omega) &= \mathbf{N}\Delta\mathbf{N}^T\ ,\ \Delta = diag(\sigma_{o1}, \cdots, \sigma_{oN}) \end{aligned} \tag{3.37}$$

7. Calculate new $\hat{\mathbf{B}}$ and $\hat{\mathbf{C}}$ such that

$$\begin{aligned} \hat{\mathbf{B}} &= \mathbf{M} diag(|\sigma_{c1}|^{1/2}, \cdots, |\sigma_{c\rho_{W_c}}|^{1/2}, 0, \cdots, 0) \\ \hat{\mathbf{C}} &= \mathbf{N} diag(|\sigma_{o1}|^{1/2}, \cdots, |\sigma_{o\varrho_{W_o}}|^{1/2}, 0, \cdots, 0) \end{aligned} \tag{3.38}$$

8. Solve the factorization of modified frequency-limited controlability ($\bar{P}_\Omega$) and observability ($\bar{Q}_\Omega$) Gramian matrices through the solution of the equation

$$\begin{aligned} \mathbf{A}\bar{P}_\Omega + \bar{P}_\Omega\mathbf{A}^* + \hat{\mathbf{B}}\hat{\mathbf{B}}^* &= 0 \\ \mathbf{A}^*\bar{Q}_\Omega + \bar{Q}_\Omega\mathbf{A} + \hat{\mathbf{C}}^*\hat{\mathbf{B}} &= 0 \end{aligned} \tag{3.39}$$

   whose Cholesky factorization are determined as

$$\begin{aligned} (\bar{P}_\Omega) &= \mathbf{P}\mathbf{P}^T \\ (\bar{Q}_\Omega) &= \mathbf{Q}^T\mathbf{Q} \end{aligned} \tag{3.40}$$

9. Perform the Cholesky decomposition and singular value decomposition in order to obtain the transforming matrix (Step 3-6 of Moore's Balanced Truncation method). Obtain the realization of the reduced model.

3.7.2 Singular Perturbation [44]

Given the results of the singular value decomposition of the modified Gawronski-Juang method, it can be seen that the Hankel singular value of the modified balanced realization is closer to zero. It is also possible to use a singular perturbation method in order to obtain the realization of model reduction instead of direct partitioning of state-space matrices as presented through balanced truncation ([26],[44]). The difference is in the goal where the singular perturbation tries to achieve the equalization of steady-state gain of both the full

model and the reduced model instead of equalizing the norm at infinite frequency. In other words, the goal of the singular perturbation method is formulated as

$$G(0) = G_{red}(0) \tag{3.41}$$

In order to achieve this, the truncated state-space matrices are perturbed by the remaining matrix-part related to the rejected states ($\bar{x}_2$). Assuming the rejected states converges to a steady-state much faster than the remaining states $\bar{x}_1$. The derivative of the rejected states is set to zero [26]. This can be seen as the extension to the algorithm of balanced truncation or modified Gawronski-Juang frequency-limited balanced truncation algorithm.

Given the partitioned matrix structures as in Equation 3.31, the model reduction matrices resulted from singular perturbation method can be formulated as

$$\begin{aligned} A_{red} &= \bar{\mathbf{A}}_{11} - (\bar{\mathbf{A}}_{12}\bar{\mathbf{A}}_{22}^{-1}\bar{\mathbf{A}}_{21}) \\ \mathbf{B}_{red} &= \bar{\mathbf{B}}_1 - (\bar{\mathbf{A}}_{12}\bar{\mathbf{A}}_{22}^{-1}\bar{\mathbf{B}}_2) \\ \mathbf{C}_{red} &= \bar{\mathbf{C}}_1 - (\bar{\mathbf{C}}_2\bar{\mathbf{A}}_{22}^{-1}\bar{\mathbf{A}}_{21}) \\ \mathbf{D}_{red} &= \bar{\mathbf{D}} - (\bar{\mathbf{C}}_2\bar{\mathbf{A}}_{22}^{-1}\bar{\mathbf{B}}_2) \end{aligned} \tag{3.42}$$

3.8 Proposed Method and Concluding Remarks

Based on the literature survey in linear structure system identification, it can be observed that the method that gives reliable results is either augmented Kalman Filter or Maximum Likelihood Estimation (MLE). In order to keep the computational cost low, the MLE can then be simplified further to the Two-Step Method. The Two-Step Method consists of the Kalman Filter for state estimation and Recursive Least-Square with forgetting factor for more reliable parameter estimation. In order to further simplify the model to enable the fast-tracking. The full mathematical model of aeroelastic wing introduced in Chapter 2 can be simplified with methods of linear model reduction. Few methods are presented, and the balanced truncation method is chosen due to its simple use and robustness. The modification is then incorporated such that the tracking and identification system can then reliably track the fast displacing modes of the wing despite its limited operating frequency.

Given that the true model is known and stable, the linear state-space system and the operating frequency range of the system can then be determined before the state and parameter estimation can then be executed. The true model can be first reduced to a smaller realization such that the number of states that are going to be estimated is smaller compared to that of the true model. In this report, the proposed model reduction method is modified frequency-limited Gawronski-Juang balanced truncation method. Once the reduced model is obtained, the reduced model will be used for state estimation using ordinary Kalman Filter. The estimated state value will then become the basis to form the regression matrix for parameter estimation by using Recursive Least-Square. The figure of the open-loop analysis that will be used for the experiment setup in this report is as follows.

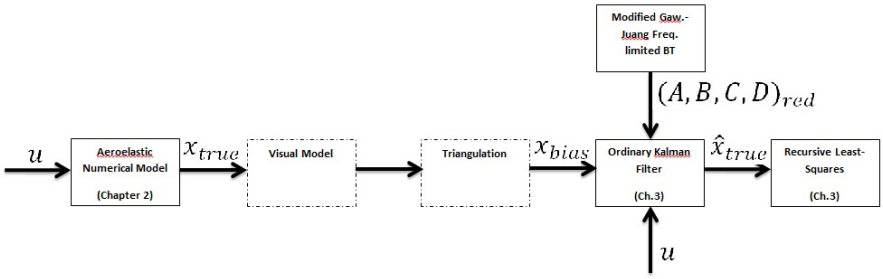

Figure 3.6: Proposed feasibility analysis framework using ROTS method.

In the end, the error obtained from the estimated parameters will be analyzed. However, since there are numerous parameters to estimate in one iteration alone, the estimated parameters will be used to obtain a new state-space matrix. In a linear case, the parameters of mass, damping, and stiffness matrices will be constant. The aerodynamic lag states-related matrix also constant with constant simulated air velocity. Hence, the eigenvalues of reconstructed state-space based on the ROTS method can be compared to the true state-space form of the model.

Concluding Remarks

Given all the concerns, the two-step method of state and parameter estimation can then be formed to accommodate the state and parameter estimation for a system of a large number of states with limited frequency or sampling rate, as described in Subchapter 3.8. The routine will be called Reduced Order Two-Step (ROTS) State and Parameter Estimation Method. Hence, the second sub-research question (**RQ 1.2**) has been fulfilled.

Chapter 4

Preliminary Analysis

With the completion of the aspect of mathematical modeling of the aeroelastic wing and the system identification suitable for the fast visual tracking system, the writer has come up with an enhanced method that is expected to enable an accurate state and parameter estimation in the system environment as mentioned earlier. The proposed Reduced-Order Two-Step (ROTS) method algorithm is reiterated from the previous chapter and formulated as follows.

1. Identify and define the linear state-space system and the operating frequency range of the system,

2. Execute balanced realization and model reduction using the modified Gawronski-Juang frequency-limited balanced truncation method,

3. Execute singular perturbation for the reduced model to obtain the final reduced model realization,

4. Execute state estimation of Kalman Filter,

5. Execute parameter estimation by using Recursive Least-Square,

6. Analyze the error and eigenvalues of reconstructed state-space based on the ROTS method compared to the true state-space form of the model.

In this chapter, a preliminary analysis of the applicability of the method will be presented to acquaint readers with the proposed method process and to help the writer during the development process to take decision further in developing the method.

4.1 Wing Geometry

In this report, a simple rectangular wing will be used as the object of interest. The rectangular wing is the property of the Department of Aerospace Structures and Materials, Delft University of Technology, the Netherlands. The wing is modeled after a clamped wing based on 4-digit NACA airfoil of NACA-0010. Hence the root is unable to move at any of six degrees of freedom. The geometry data of the wing is tabulated as follows.

Table 4.1: Wing Geometric Properties

Semi span (L_w)	1.75 meters
Chord ($2b$)	0.25 meters
Shear center location (a)	0 meters

4.2 Mathematical Modelling

As mentioned in Chapter 2, the corresponding mass and stiffness model matrix is obtained from the in-house aeroelastic structure geometry analysis software PROTEUS. In this case, the wing model is discretized into 13 two-dimensional wing sections where each has six degrees of freedom. The discretization yields a square matrix with a dimension of 78 by 78 parameters. The displacement states for each wing section represent the displacement of the center element of each wing model. Therefore the obtained structure for both mass and stiffness matrix can be seen as in the following figure.

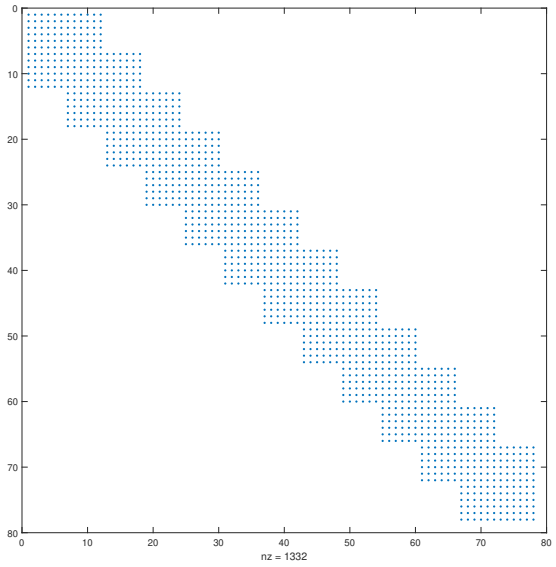

Figure 4.1: PROTEUS-generated mass and stiffness matrices' structure

It can be seen that the blue dots represent the non-zero elements of the matrix. Otherwise, the empty white field represents zero elements. The structure signifies the influence of one wing section to the immediate wing section. Therefore the displacement of one wing section can be inferred as direct or indirect results of the displacement in other wing sections. Given the actual mass and stiffness matrices, the eigenvalues lie all across the imaginary axis. Such that the wing shows an oscillating behavior given a step input, as shown in Figure 4.2. It confirms that the PROTEUS model is consistent with the true nature of the undampened system.

In addition to that, the damping matrix can be generated artificially to represent the dampening behavior of the wing displacement modes in reality. The damping parameter is dependent on the natural frequency, which is the square root of stiffness divided by mass while the damping coefficient is of chosen value between 0 and 0.05. In approaching the formulation of the structural damping matrix. Two methods are approached, first is by multiplying the double value of damping coefficient (2ζ) times natural frequency as formulated in Equation 2.6 and the second approach is introduced by Asjes [2] where

$$\omega_{n[2]} = 2\zeta\sqrt{diag(K_s) \oslash diag(M_s)} \tag{4.1}$$

For both the damping matrix formulations, the mathematical modeling with the first damping strategy will be named (**Model 1**, and the mathematical modeling with Asjes' damping strategy is (**Model 2**. The damping matrix will result in the formation of 78 by 78 square matrix. The size is consistent as the size of mass and stiffness matrices.

With the full structural mass, damping and stiffness matrices are known. The final equation can then be transformed into the state-space formulation. By doing the substitution on both hands of the equation, the

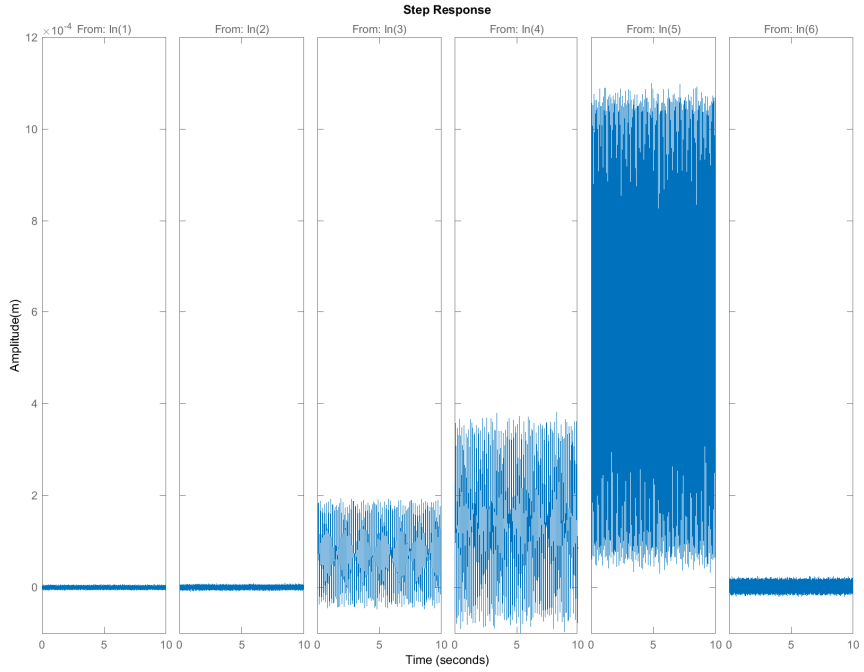

Figure 4.2: The undampened heaving attitude behaviour of the tip wing section against various inputs.

state space of the structure dynamics part can then be formed as

$$\begin{bmatrix} M_\phi \\ M_\alpha \\ M_\psi \\ F_x \\ F_y \\ F_z \end{bmatrix} = M_s\ddot{x}_a + C_s\dot{x}_a + K_s x_a + diag \begin{bmatrix} 0 & 0 \\ \frac{1}{2}\rho V^2 S(b(\frac{1}{2}+a))(4\pi\frac{b_1 b_2}{2}(\frac{V}{b})^2) & \frac{1}{2}\rho V^2 S(b(\frac{1}{2}+a))(A_1 b_1 + A_2 b_2)(\frac{V}{b}) \\ 0 & 0 \\ 0 & 0 \\ 0 & 0 \\ \frac{1}{2}\rho V^2 S(4\pi\frac{b_1 b_2}{2}(\frac{V}{b})^2) & \frac{1}{2}\rho V^2 S(A_1 b_1 + A_2 b_2)(\frac{V}{b}) \end{bmatrix} \begin{bmatrix} z_{1,i} \\ z_{2,i} \end{bmatrix}_n$$
$$+ diag \begin{bmatrix} 0 & 0 \\ \frac{1}{2}\rho V^2 S(b(\frac{1}{2}+a))\pi & \frac{1}{2}\rho V S(b(\frac{1}{2}+a))^2\pi \\ 0 & 0 \\ 0 & 0 \\ 0 & 0 \\ \frac{1}{2}\rho V^2 S\pi & \frac{1}{2}\rho V S(b(\frac{1}{2}+a))\pi \end{bmatrix} \begin{bmatrix} \alpha_i \\ \dot{\alpha}_i \end{bmatrix}_n$$
$$\mathbf{F}_a = M_s\ddot{x}_a + C_s\dot{x}_a + K_s x_a + K_z z + C_{ae}\ddot{x}_a + K_{ae}x_a$$
$$\ddot{x}_a = -M_s^{-1}((C_{ae}+C_s)\ddot{x}_a + (K_{ae}+K_s)x_a + K_z z - \mathbf{F}_a) \tag{4.2}$$

and the aerodynamic lag dynamics state space is represented as in Equation 2.17. The aerodynamic lag is not affected by the inverse of the mass in the structural dynamic part, nevertheless the structural displacement influences the aerodynamic lag values through the quasi-steady angle of attack formation.

Given the full picture of the state-space matrices. The dynamics part of the state space can then be built by incorporating the structural dynamics and aerodynamic lag part into the form of **A** matrix. Since there are 78 states of displacement, in order to solve the second-order equation, the number of structural is doubled to 156 states. On top of that, two aerodynamic lags govern the aerodynamic influence for each wing section. The addition will yield 26 aerodynamic lag states for 13 wing sections. In total, 182 states are incorporated with six inputs.

The inputs are forces and moments data obtained from the simulation of discrete cosine gusts, which

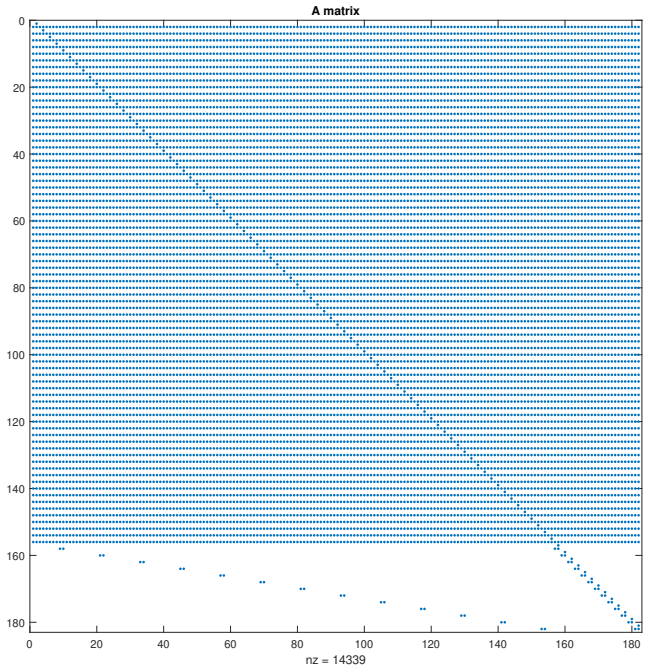

Figure 4.3: **A** state-space matrix structure

has been conducted in Wind Tunnel of TU Delft's Open Jet Facility on 12-17 April 2019. For each wing section, In this numerical simulation, the forces and moments are assumed to be distributed equally across the wingspan such that the force and moments at each wing section equal the total force and moments divided by the number of wing sections.

Given the structure of the state-space, it is then possible to start the numerical simulation. In the following section, the results of the proposed model reduction, state estimation, and the parameter estimation will be presented. In this chapter, the mathematical model will be tested against one non-turbulent condition (static forces and moments) and also one gust condition in the cosine signal form. The gust condition is simulated at a small frequency of 4 Hz at a velocity of 13.6 m/s. Therefore, the four cases to be observed in this chapter will be structured as follows

Table 4.2: Preliminary Analysis Cases

Model type	Case	V_{air}	Turbulence freq.	Add. info
Model 1	1	13.6	0 Hz	$F_z = 1N$ and $M_\alpha = 1Nm$
	4	13.6	4 Hz	-
Model 2	1	13.6	0 Hz	$F_z = 1N$ and $M_\alpha = 1Nm$
	4	13.6	4 Hz	-

4.3 Algorithm Path

4.3.1 Model reduction

In order to simplify the model in ROTS state and parameter estimation, the model reduction will have to be performed in advance to simplify the model. In this part, the reduction of the full aeroelastic model will be compared against the model reduction by using Moore's balanced truncation method, Gawronski-Juang

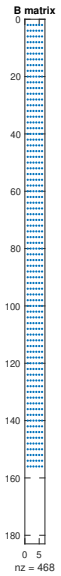

Figure 4.4: **B** state-space matrix structure

balanced truncation method, and the proposed modified Gawronski-Juang model reduction. Later for the development of state-space estimation, the **B** and **D** matrices will be further augmented to accommodate the process and measurement noise effect to the transformed, reduced states. In this report, the damping frequency is chosen at $\zeta = \mathbf{0.01}$.

4.3.2 State and Parameter Estimation Setup

Once the reduced realization of the model has been obtained, the state and parameter estimation using the Two-Step Method will then be able to be performed. At this condition, the reduced state-space realization input is further augmented by the process noise matrix **G** and the measurement noise of **H** [57]. The routine will be run at a uniform sampling rate of 50 Hz. The two noise matrices are in the form of identity matrices belonging to the respective states and parameters involved in the reduced model realizations. In this chapter, the process noise and measurement noise are determined in advance. According to [34], the determined process noise and measurement noise are chosen to be in 0.5 pixels and 1.0 pixels, respectively. However, it can be seen that the image quality in terms of pixel resolution is different where Huynh et al. uses lower quality images. In addition to that, the sensor which measures the input of forces and moments also has its own process and measurement noise. In this case, the noise is based on the world reference frame instead of the pixel reference frame. The choice of the process and measurement noise is arbitrary, representing the image resolution noise and forces and moment sensors. Furthermore, the forces and moments noise will be more pronounced as the accelerometer, and inertial measurement unit runs at a higher sampling rate. For these cases, the forces and moments input is given at a rate of 800 Hz. Hence, the effect of noise of different sensors with different sampling rate can also be studied. These noises are tabulated as

In the true derivation of the Kalman Filter formula, it is often assumed that the **D** matrix is left out since there is no interference from the inputs to the measurement estimation of the states. In the case where the singular perturbation step is executed to gain a better-reduced realization of the model, the **D** matrix is no longer a zero matrix. Nevertheless, in this report, the assumption of a zero **D** matrix is still maintained since the parameters contained in the mentioned matrix is insignificant (close to zero) in order to perform the state estimation Kalman Filter routine.

For each iteration, the results of the state estimation will then be passed to the Recursive parameter estimation routine as the new data. The algorithm used in this phase is a Recursive Least-Square, as suggested by Ghanem and Shinozuka ([22],[72],[24]). Furthermore, in order to increase the reliability of the results, the forgetting factor is also introduced. In order to verify the method as in the literature, the forgetting factor

Table 4.3: Noise Case

Parameters	Value
Process noise	1.5×10^{-5}
Measurement noise, translation states	3.0×10^{-5} meters
Measurement noise, translation rate states	3.0×10^{-5} m/s
Measurement noise, angular attitude states	3.0×10^{-5} radians
Measurement noise, angular rate states	3.0×10^{-5} rad/s

λ is chosen at **0.99**. Although further recommendation allows the forgetting factor is chosen between the range of 0.70 and 1, the preliminary results show that the error realization of recursive least-square is more pronounced when the forgetting factor is less. Due to the limited computational power of the computing processing hardware, the recursive least-square results are at the moment analyzed after 10 seconds of simulation. This translates to after two cosine gust signals are triggered.

However, as the recursive algorithm suggests, the first step is to obtain the "old data" by doing an offline parameter estimation. The offline parameter estimation is often referred to as the training phase. While the length of the training phase is arbitrary, it is chosen that the training phase will be of the same length as the simulation period. Furthermore, in order to keep the parameter estimation close to optimal, or, in other sense, to keep the covariance value low, the weighted least-square routine is performed in the training phase as formulated in the previous chapter.

In order to investigate the results, the results will be compared. In this case, the estimated state-space **A** matrix should be able to, at a certain degree, mimic the position of eigenvalues of the true model or keep the characteristics of the true model poles. However, it is almost impossible to ensure that the parameter estimation for the mass, damping, and stiffness matrices will yield the same number as it converges with the true model. Therefore, the alternative approach of eigenvalues is then more feasible to do in this case.

4.3.3 Time-domain Analysis Tools

In order to fully understand the success of a model reduction method. The reduced model can then be analyzed by various means in both the time and frequency domain. In the time domain, the success of model reduction can be analyzed by either simple observation of scatter plot of states value compared to the true model's states value, calculating the root-mean-square error (RMSE) of the reduced model, or by calculating the coefficient of determination (R-squared value). The observation of the scatters plot is done to look at a linear fit between the reduced model and the true model behavior. On the other way, the root-mean-square error calculation is performed to quantify the difference between the value obtained from the reduced model and the true model at the same number of samples [35]. Given the set of N samples of states from the reduced model and the true model. The error between the two models is represented as ε. Therefore, the root-mean-square error of the two models is formulated as

$$RMSE = \sqrt{\frac{\varepsilon^T \varepsilon}{N}} \tag{4.3}$$

It is often also that the value of root-mean-square error is represented in terms of percentage. The so-called Normalized RMSE (NRMSE) is formulated as

$$NRMSE = 100\% \times \frac{RMSE}{\bar{x}_{true}} \tag{4.4}$$

Where $\bar{x}_{true}$ represents the mean of the true model states value. From here, the model reduction is deemed successful if the RMSE is closer to zero, which signifies a minuscule error obtained from the reduced model. Another way to quantify the success rate of a model reduction is by calculating the R-squared value. The coefficient of determination is another method of regression analysis that measures the confidence of one model compared to the reference. In other words, it provides a measure of how well-observed outcomes are replicated by the model, based on the proportion of total variation of outcomes explained by the model [16]. The calculation of R-squared value is equal to the squared Pearson correlation coefficient (ρ_P) of the true

system and the reduced system which is formulated as

$$\rho_P = \frac{1}{N-1}\sum_{i=1}^{N}\left(\frac{x_{i,true}-\mu_{true}}{\sigma_{true}}\right)\left(\frac{x_{i,red}-\mu_{red}}{\sigma_{red}}\right) \tag{4.5}$$

It can be seen that the Pearson correlation coefficient is dependent on the cross-variance of the two models and the standard deviation of both systems as well as the number of samples taken. The value may range between -1 and +1. This value signifies the relation between the two sample sets. The negative correlation coefficient shows that the systems are fit, yet in reverse trend, i.e., the reduced model may estimate the decreasing trend while the true trend is ascending. The positive value signifies the same trend of data. In the case of Pearson's coefficient equal to 1, the coefficient value signifies that the reduced model can perfectly fit the true model behavior in the same trend and values. In this case, the scatter plot will then show a perfectly straight line resembling a line function of $x_{true} = x_{red}$.

4.3.4 Frequency-domain Analysis Tools

Besides the analysis in time-domain, the analysis can also be performed in the frequency domain. In this domain, the analysis can be obtained by analysis of the Bode diagram and looking at the poles position of both the reduced model and true model.

A Bode diagram is a set of plots that shows the asymptotic approximation of the frequency response of a system across the frequency spectrum. The Bode diagram measures both magnitude (in decibels) and phase (in degrees) of the frequency response of the system [60]. However, it is often found from the model-reduction analysis papers that the magnitude plot is more widely used in order to validate the results of model reduction. In the context of validation of the reduced model against the original system, the model reduction is deemed successful when the magnitude response of the reduced model is equal to that of the original model. In many cases, the Bode plot analysis suffices for the validation on the ground that the reduced system will be stable when the original system is stable [21]. Nevertheless, it can sometimes be misleading since the magnitude plot only shows the absolute position of zeros and poles. Therefore, it cannot readily indicate whether the system is stable or not. An example of a Bode magnitude plot of simple transfer functions can be seen as follows.

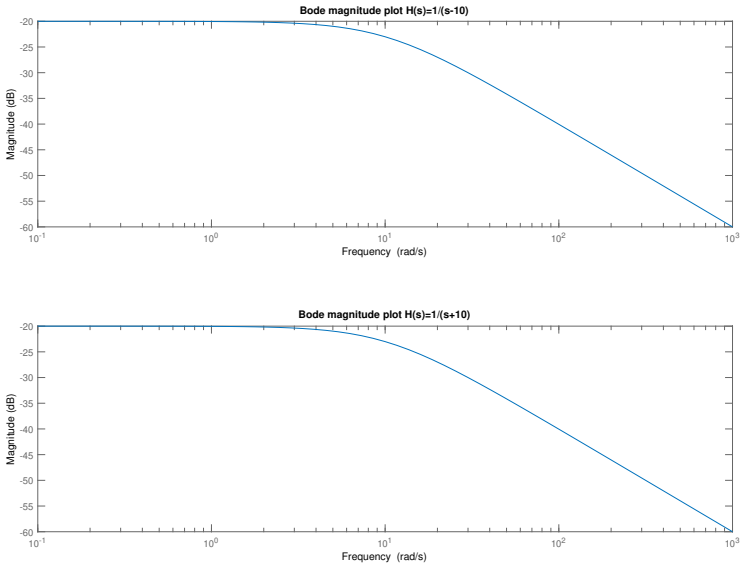

Figure 4.5: Bode magnitude plot of an unstable system (top) and a stable system (bottom).

Due to insufficient interpretation of the magnitude plot, the Bode phase shift should also be analyzed together with the Bode magnitude analysis. It is so since the difference can be seen that the phase will increase

with the unstable pole. However, it can be understood that the Bode phase plot may show a more significant difference between the two systems, thus yielding a less convincing view.

Another possible frequency analysis method is by looking at the poles' position of the reduced model. Initially, the transformed model should be able to retain the characteristics of the poles of the true model. In the context of an originally stable system, this can be translated into maintaining the representation of the reduced model such that poles are always in the left-half plane. In further translation, this can also mean maintaining the trend of pole placement of the original model, although the pole position will undoubtedly change with the remaining number of states. The results of the poles position analysis can be seen in the next subchapter regarding the preliminary analysis of the determined models and cases.

4.4 Model Reduction Results

In this section, the discussion of the analysis results in both the time-domain and frequency-domain for model reduction of both models, and the Two-Step method will be discussed further. Since there are quite many figures for analysis results added in this report, the figures will be displayed later in the next section for the convenience of the readers to see the discussion regarding the obtained results. Subchapter 4.5 contains the compilation of all figures of the results for all cases presented in this chapter.

4.4.1 Model 1 Reduction

For Model 1, the true model has eigenvalues that represent a total of 78 bending and torsion modes as well as 26 aerodynamic lag states. In total, the state-space representation of Model 1 will yield 182 poles, which can be seen as in the following Figure 4.6.

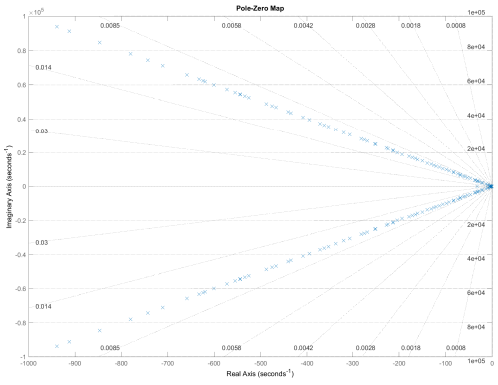

Figure 4.6: True eigenvalues of Model 1 mathematical model.

It can be observed that the introduction of the damping matrix affects the position of the eigenvalues such that all the eigenvalues lie in the left-half plane. Therefore it can be concluded that Model 1 is in a stable condition. The model reduction can then now be applied to the system as the stability criteria have been fulfilled. In this case, an example of a comparison between the algorithm of balanced truncation, frequency-limited Gawronski-Juang balanced truncation method, and modified Gawronski-Juang balanced truncation algorithm will be presented by using time-domain analysis tools. Based on the derivation of the full mathematical model of an aeroelastic wing, the analysis can then be started by using the parameters, as mentioned in Table 4.1 and 4.2. In addition to that, the frequency upper and lower limit for frequency-limited model reduction is chosen as follows.

In this comparison case, the reduced model is iterated to be reduced one by one. Hence it can be determined in which the least number of states the correct model behavior can be well represented. By analyzing the tip heaving displacement state (State 149), the normalized RMSE and R-squared values of the reduced model of all reduced realization of the system can be summarized for the three simulated model reduction

Table 4.4: Frequency Range of Visual Tracking System Case

Parameters	Value
Lower limit (ω_1)	0 Hz
Upper limit (ω_2)	150 Hz

methods. First, the analysis is using the balanced truncation method. The results are well-tabulated in Figure 4.7. The results are then compared to the reduced model iteration using the Gawronski-Juang balanced truncation method and the proposed modified version of the method.

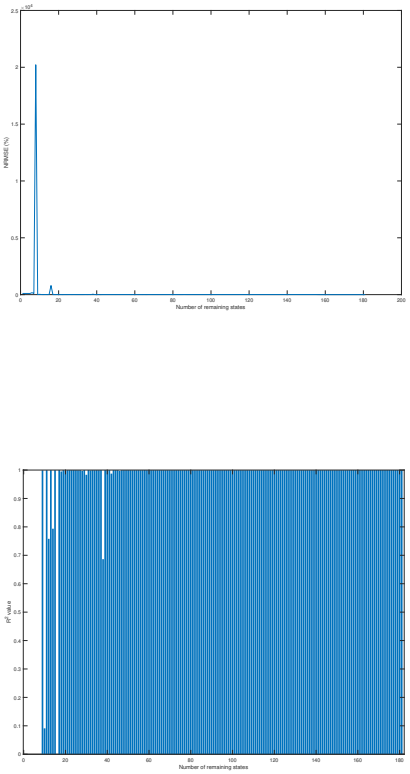

Figure 4.7: **(Model 1, Case 1)**. The Normalized RMSE in percent (top) and R-squared value of model reduction iteration using Moore's balanced truncation method (bottom)

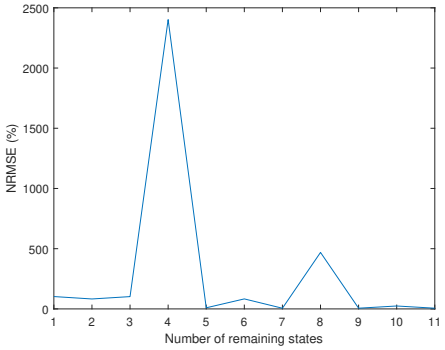

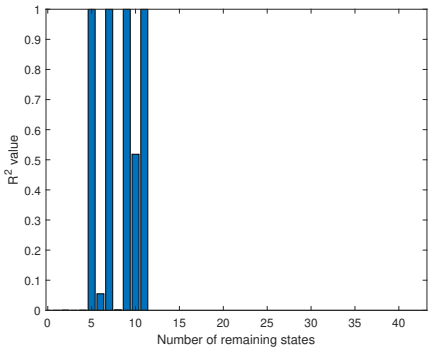

Figure 4.8: **(Model 1, Case 1)**. The Normalized RMSE in percent (top) and R-squared value (bottom) of reduction using Gawronski-Juang frequency-limited balanced truncation method.

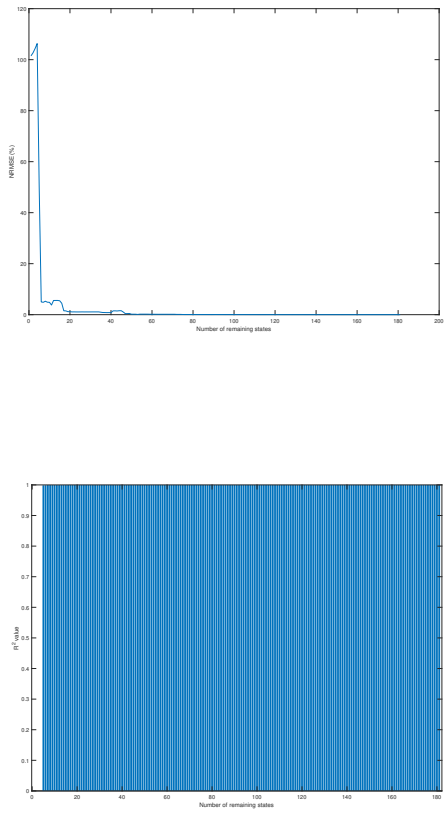

Figure 4.9: **(Model 1, Case 1)**. The Normalized RMSE in percent (top) and R-squared value (bottom) of model reduction iteration using modified Gawronski-Juang frequency-limited balanced truncation method. Reduced realization of 6 states

From the model reduction iteration results in Figure 4.7, 4.8, and 4.9, it can be seen that both Moore's balanced truncation method and modified frequency-limited Gawronski-Juang balanced truncation method successfully yield a set of stable results for any number of states' realizations. On the other hand, while the original Gawronski-Juang routine is capable of calculating a stable model reduction, the trends are less consistent compared to the other two methods. Hence the results are rejected for other simulation cases onwards. Using a 99 % confidence obtained from the R-squared value which corresponds to around 10 % in normalized RMSE, Moore's balanced truncation method can reconstruct the state-space with 10 states with a normalized RMSE of 5.2 % while the model reduction using modified Gawronski-Juang method is successful

in approximating the true model with six states with normalized RMSE of 4.3 %. The current results show that the proposed model reduction yields better results than the other compared methods. The scatter plot of the states further supports the results. Here again, the heaving tip state is used as the states with the most significant order number of displacement. Furthermore, the pole-zero placement of the system can be observed to retain the characteristics of its true model trend. It can also be seen for interested readers that reducing the state to only one state shows that the farthest state has the most significant energy among other states.

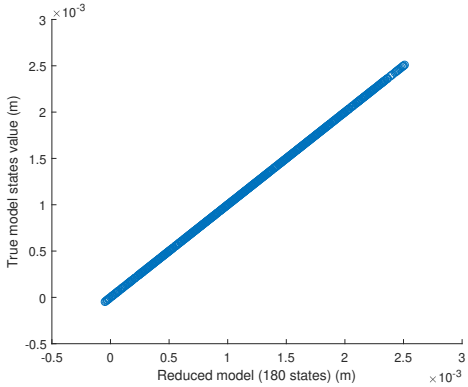

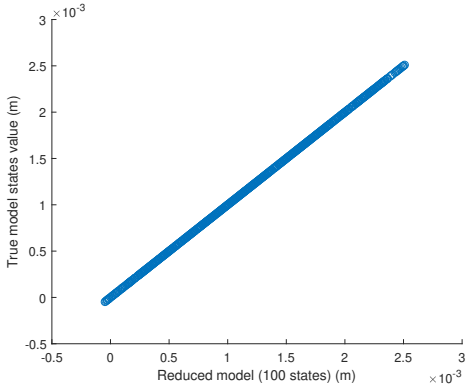

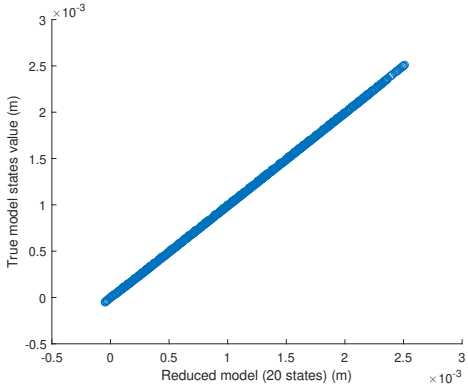

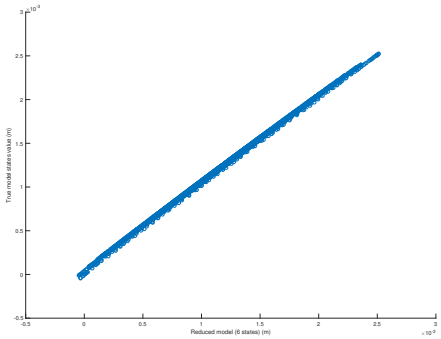

Figure 4.10: **(Model 1, Case 1)**. Scatter plots of true model samples against the reduced model of (from the first to the last) 180 states and 6 states.

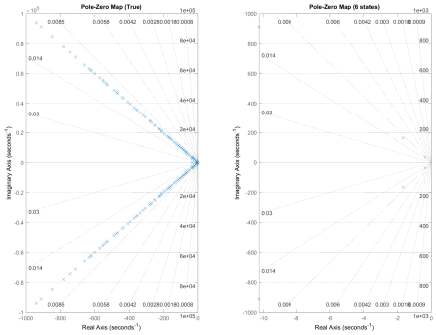

Figure 4.11: **(Model 1, Case 1)**. Pole-zero map of modified Gawronski-Juang method with 6 states against the true pole-zero map.

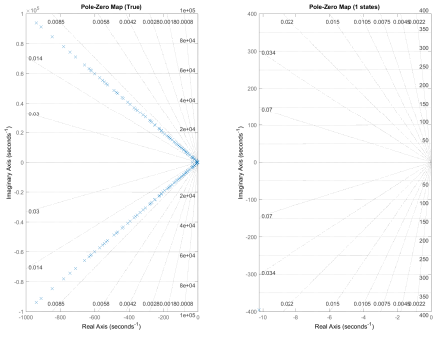

Figure 4.12: **(Model 1, Case 1)**. Pole-zero map of modified Gawronski-Juang method with 1 state against the true pole-zero map.

Furthermore, it is also suggested the singular perturbation also improves the balanced truncation results. The normalized RMSE analysis further confirms the finding. The Moore's balanced truncation results show a reduction down to 0.226 % while the modified Gawronski-Juang method shows the normalized-RMSE of 0.38 %. However, the results also show that, in this case, the least number of states to match the original model does not decrease. The results are shown in the Figure 4.13 and 4.14. Given the potential of the results, the model reduction for the remaining cases will consider the singular perturbation as the "clearing up" step for the proposed method.

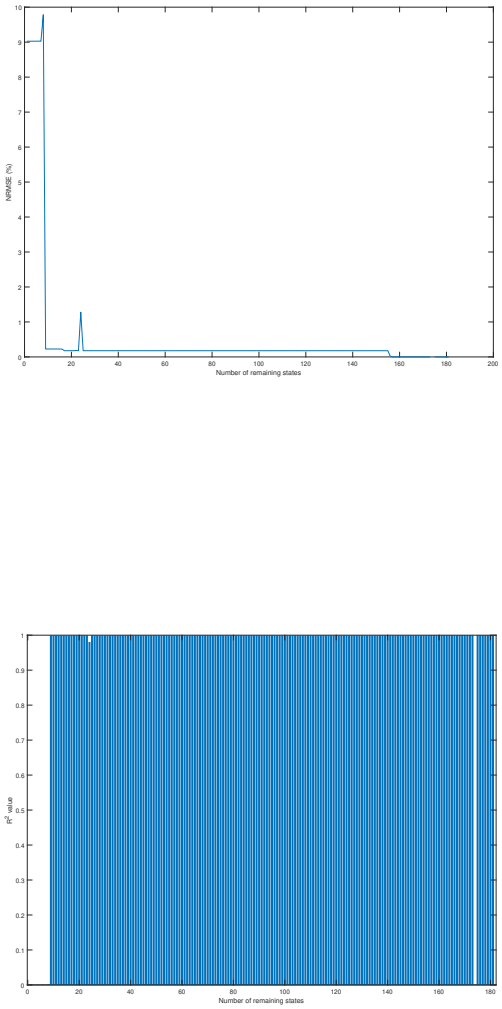

Figure 4.13: **(Model 1, Case 1)**. The Normalized RMSE in percent (top) and R-squared value (bottom) of model reduction iteration using Moore's balanced truncation method with extended singular perturbation step.

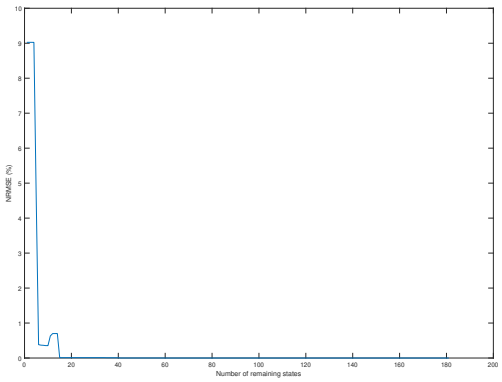

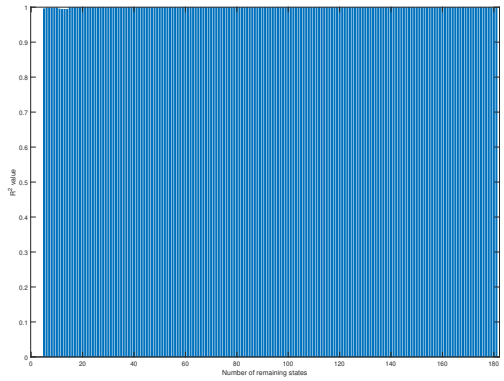

Figure 4.14: **(Model 1, Case 1)**. The Normalized RMSE in percent (top) and R-squared value (bottom) of model reduction iteration using modified Gawronski-Juang frequency-limited balanced truncation method with extended singular perturbation step.

As mentioned in Table 4.2, two cases are going to be tested fr preliminary analysis. It can be seen from the comparison of normalized RMSE that the realization quality of the reduced state space decreases with the presence of gust. It can be seen that although the R-squared value stays at a value closer to 1, the normalized RMSE grows to 2.63 % at the same reduced model realization of 6 states (Figure 4.15) for the realization using modified Gawronski-Juang frequency-limited balanced truncation method by singular perturbation step.

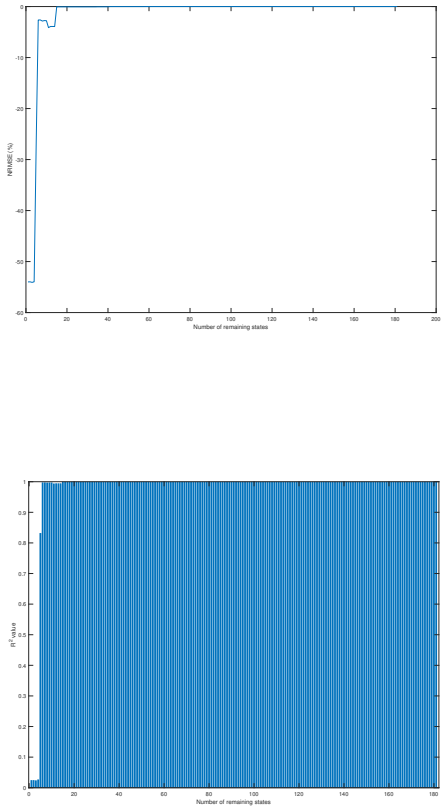

Figure 4.15: **(Model 1, Case 2)**. The Normalized RMSE in percent (top) and R-squared value (bottom) of model reduction iteration using modified Gawronski-Juang balanced truncation method with extended singular perturbation step.

Again by analyzing the scatter plots and the pole-zero maps for Model 1, Case 2, the evolution of the

linearity and the pole-zero movement can be observed. At the realization of 180 states, very close to the realization of the original model of 182 states, it can be observed that as in the Model 1 Case 1 results that the scatter plot is perfectly linear (Figure 4.16. The finding is further confirmed by the observation of poles and zeros of the reduced system in Figure 4.17.

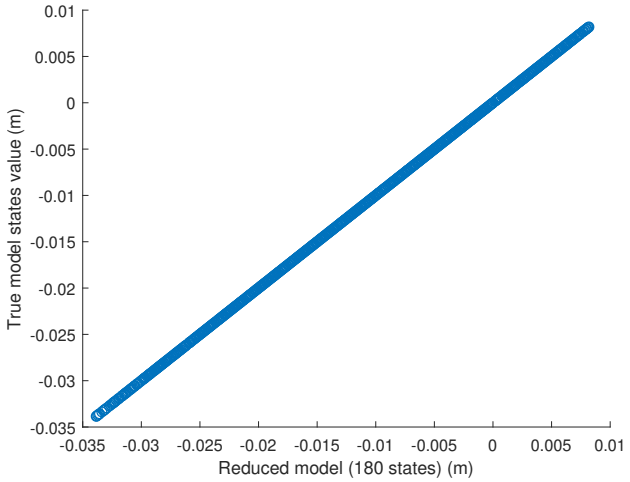

Figure 4.16: **(Model 1, Case 2)**. Scatter plots of true model samples against the reduced model of 180 states.

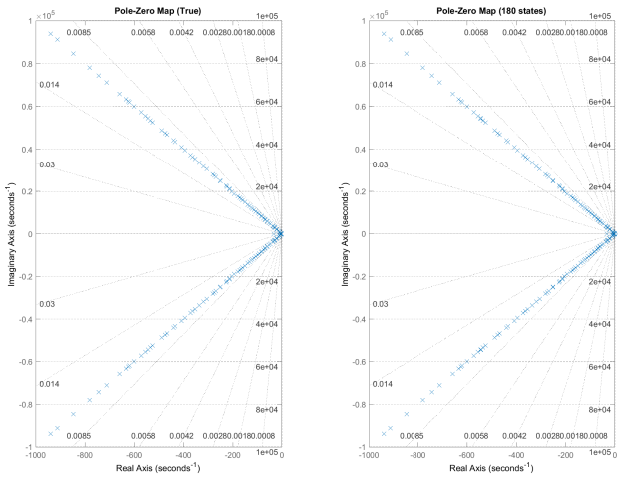

Figure 4.17: **(Model 1, Case 2)**. Pole-zero map comparison of 180-states reduced model and 182-states true model.

At a glance, one may not see the difference between the pole-zero map of the original model and the reduced model. Again the same results are observed in the scatter plots of reduced model evolution in Figure 4.18. The perfect linear trend observed at the reduced model with 180 states realizations is observed up to 6 states when it starts to degrade. A further sample is also taken with the realization of Model 1 with five states. It can be seen from the corresponding normalized RMSE and R-squared value that the realization has a low value of correlation and a higher error value. This is supported by the analysis of the scatter plot of Figure 4.18.

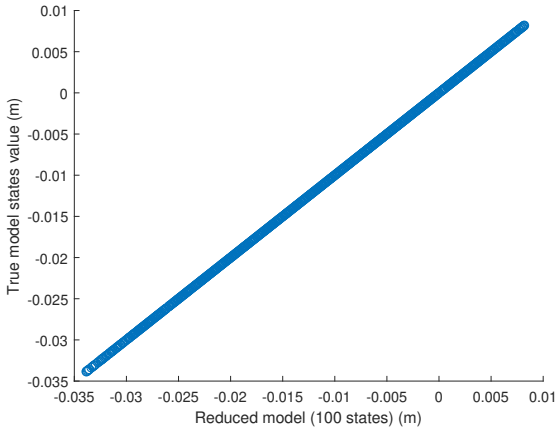
True model states value (m)
Reduced model (100 states) (m)
0.01
0.005
0
-0.005
-0.01
-0.015
-0.02
-0.025
-0.03
-0.035
-0.035 -0.03 -0.025 -0.02 -0.015 -0.01 -0.005 0 0.005 0.01

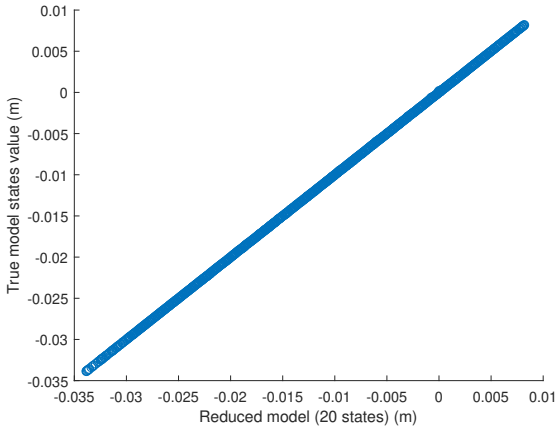
True model states value (m)
Reduced model (20 states) (m)
0.01
0.005
0
-0.005
-0.01
-0.015
-0.02
-0.025
-0.03
-0.035
-0.035 -0.03 -0.025 -0.02 -0.015 -0.01 -0.005 0 0.005 0.01

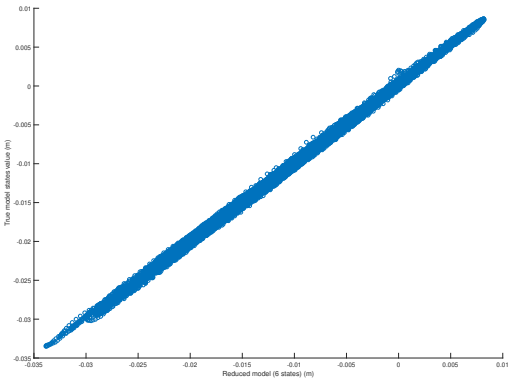
True model states value (m)
Reduced model (6 states) (m)

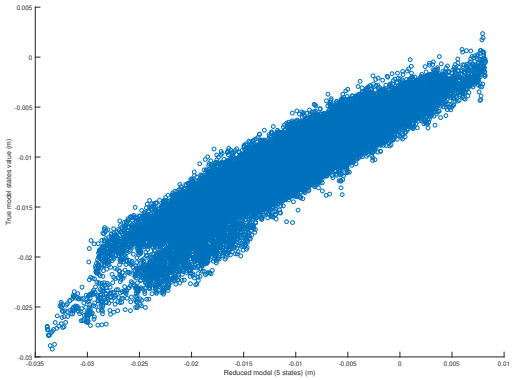

Figure 4.18: **(Model 1, Case 2)**. Scatter plots of true model against the reduced model. Evolution of tip heaving state of reduced models of (from the first to the last) 100, 20, 6, and 5 states.

It can be seen that at high normalized RMSE value and low correlation, the linear trend that has been previously observed at the realization of higher-order has pretty much degraded since the value of the samples of the states obtained from the reduced model deviates significantly. At the occurrence of higher deviation value, the linear line characteristics of the scatter plot become less dominant, and the trend becomes more random r the relation is no longer explainable with the linear relation. It can also be observed from the pole-zero map (4.19 that each realization retains to some degree the shape of the pole distribution of the true model in a triangular shape. This finding confirms the relation among the high coefficient of determination, the low normalized root-mean-square error, and the pole-zero position. It can also be observed that the realization of gusts does not affect the possible minimal realization.

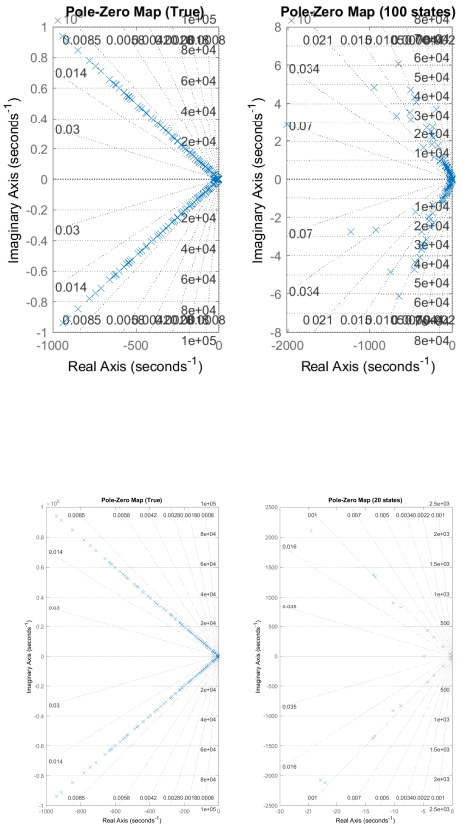

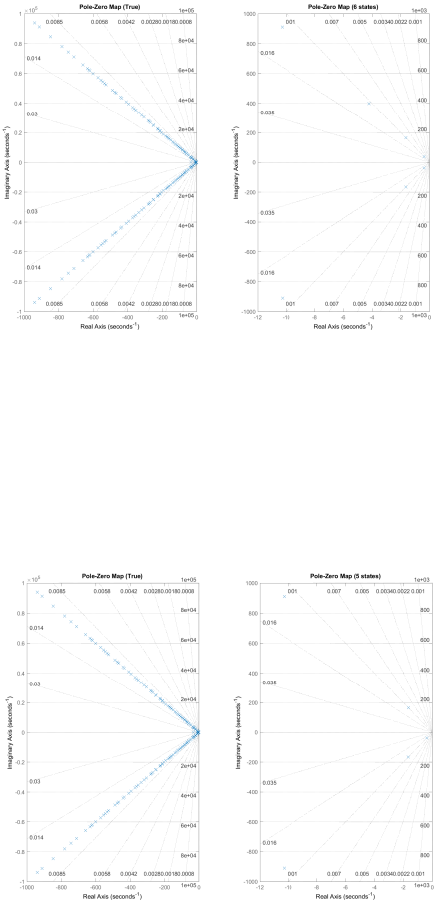

Figure 4.19: **(Model 1, Case 2)**. Pole-zero map comparison between the true (left) and the reduced model (right). The evolution in the right is of (from the first to the last) 100, 20, 6 and 5 states.

The model reduction validity can also be observed from the Bode plot frequency analysis. In this case, the heaving frequency response against the vertical force input is the subject for the comparison. Since the angle-of-attack frequency response against the inputs is flat at the frequency range of interest, therefore the dynamics of the model reduction can not be as clearly observed. For the two cases presented, the realization of gust conditions does not affect the shape of the Bode magnitude plot since it only depends on what frequency poles and zeros lie. The frequency range of interest is again at the range between 0 and 150 Hz, an equivalent to 0 and 943 radians per second, respectively. The results can be seen at Figure 4.20-4.24. Again the sample model reduction realization of 180, 100, 20, 15, and 6 states are presented. The presented results show that at realization with perfect R-squared value (up to 15 states), the Bode magnitude plot of the reduced model shows the same characteristics as the true model. However, it can be seen that the same can not be said for the realization of 6 states. The results may have a relationship that shows a slightly lower R-squared value. This condition can be investigated from the zoomed-in Bode plot of Figure 4.24 at a lower frequency, the reduced realization has the same characteristics as the true model. However, the similarities stop after the second downward slope, where the similarities end. It can be suspected that due to insufficient realization, the mode of higher frequency can not be sufficiently imitated by the reduced model since all the captured poles lie at the lower frequency. Hence, its frequency response shows a flat line after around 30 Hz, meaning that the reduced model of 6 states can only imitate the true system only at the meager sampling rate. However, this shows that a high correlation value between the true model and frequency model does not always require the reduced system to mimic the whole true system behavior at the whole range of frequency. This will be further investigated by analyzing the results of Model 2.

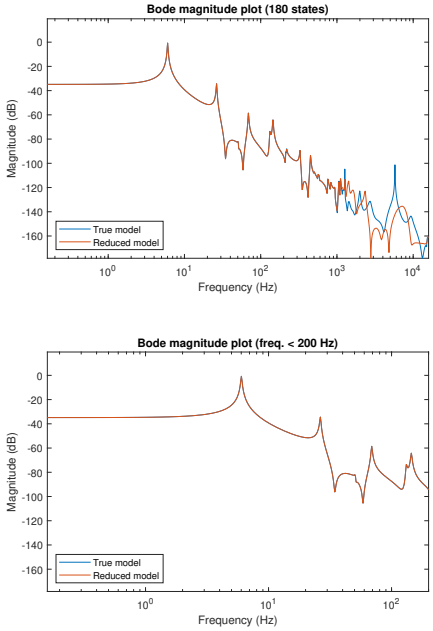

Figure 4.20: **(Model 1)**. Bode magnitude (frequency response) plot of tip heaving response due to the vertical force input. The comparison between the true model and the reduced model of 180 states for all frequency spectrum (top) and the zoomed-in plot for the frequency range of interest (bottom) in Hertz. Note that the frequency response of the reduced model is at the same magnitude as that of the true model.

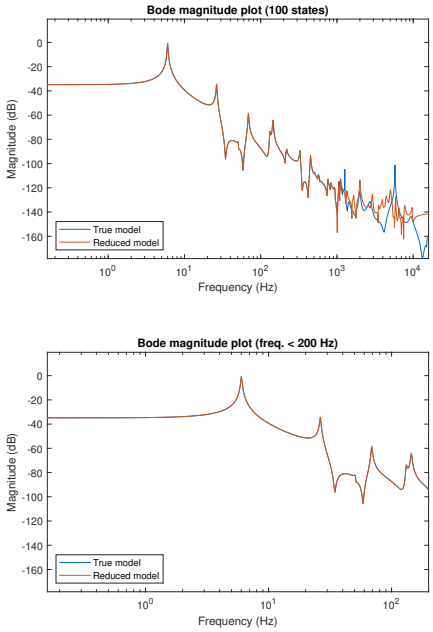

Figure 4.21: **(Model 1)**.Bode magnitude (frequency response) plot of tip heaving response due to the vertical force input. The comparison between the true model and 100-states reduced model for all frequency spectrum (top) and the zoomed-in plot for the frequency range of interest (bottom) in Hertz.

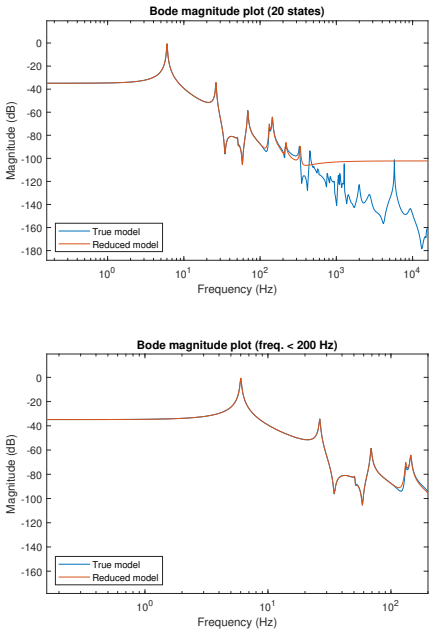

Figure 4.22: **(Model 1)**.Bode magnitude (frequency response) plot of tip heaving response due to the vertical force input. The comparison between the true model and 20-states reduced model for all frequency spectrum (top) and the zoomed-in plot for the frequency range of interest (bottom) in Hertz.

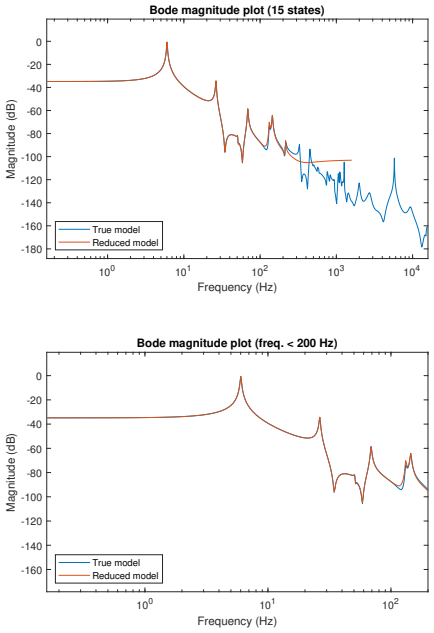

Figure 4.23: **(Model 1)**. Bode magnitude (frequency response) plot of tip heaving response due to the vertical force input. The comparison between the true model and 15-states reduced model for all frequency spectrum (top) and the zoomed-in plot for the frequency range of interest (bottom) in Hertz.

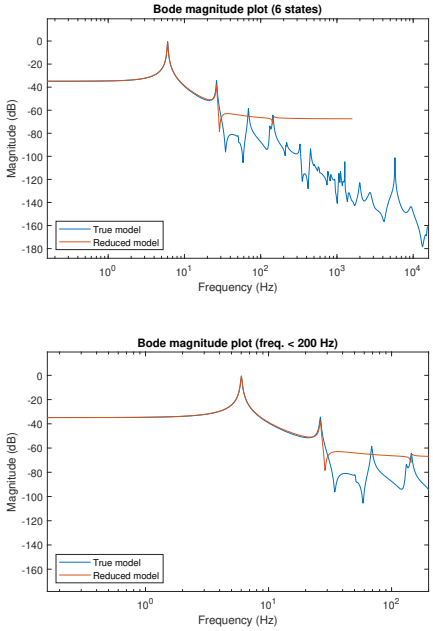

Figure 4.24: **(Model 1)**. Bode magnitude (frequency response) plot of tip heaving response due to the vertical force input. The comparison between the true model and 6-state reduced model for all frequency spectrum (top) and the zoomed-in plot for the frequency range of interest (bottom) in Hertz. Note that the frequency response at the frequency range of interest is not equal to the true model to some extent, but still yielding a highly confident R-squared value.

4.4.2 Model 2 Reduction

In Model 2, the true model also has eigenvalues, which represent a total of 78 bending and torsion modes as well as 26 aerodynamic lag states. The difference is only in the realization of the damping matrix, whose inspiration for this model comes from Asjes (2015) [2]. Hence the damping for each axis can not be generalized to one single value as in Model 1. In total, the state-space representation of Model 2 will yield 182 poles, all of which lie on the left half-plane such that the system is also stable. Using the same criteria of the frequency range as in Table 4.4, the simulation can then be executed for non-turbulent and turbulent flows.

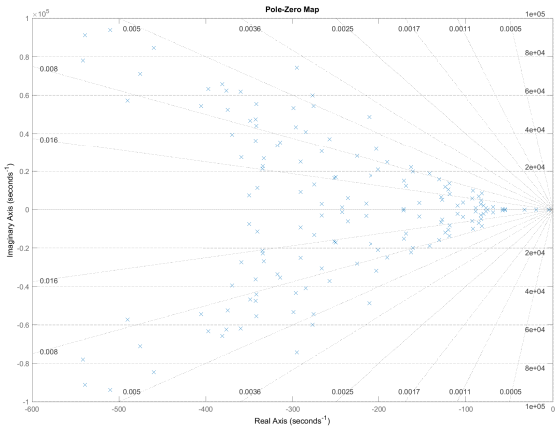

Figure 4.25: True eigenvalues of Model 2 mathematical model.

Again as the preliminary analysis of the model, the iteration is conducted by using Moore's balanced truncation and modified frequency-limited Gawronski-Juang balanced truncation with an additional step of singular perturbation for both. The comparison has been made, and it shows a significant difference. The achieved results can then be seen as in Figure 4.26-4.27. It can be observed that there is a clear difference in the results of R-squared value between the one using Moore's balanced truncation routine and the modified Gawronski-Juang method. It can be observed that while the modified Gawronski-Juang can maintain a perfect R-square value up to the realization of 15 states, Moore's balanced truncation shows the perfect coefficient of determination up to only the reduced realization of 124 states. Besides that, it can be observed that Moore's balanced truncation is unable to find the numerical realization with high R-squared value at even higher states number realization. The results mean there is little to no correlation between the true model and reduced model at realization around 170 states and above as well as the realization of 123 states and lower. This confirms the finding from [21], which states that the realization using Moore's balanced truncation is inferior in this case since the possible produced reduction model has the least number of states closer to the number of states of the true model — rendering the reduction less significant comparing the proposed Gawronski-Juang method and also its improved versions.

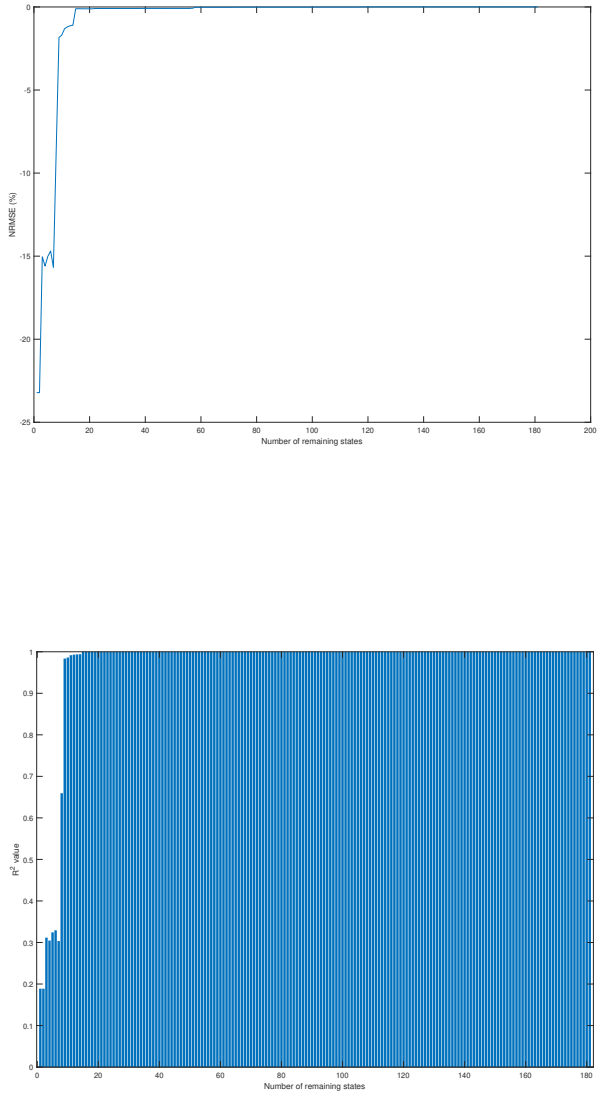

Figure 4.26: **(Model 2, Case 1)**. The Normalized RMSE in percent (top) and R-squared value (bottom) of model reduction iteration using modified Gawronski-Juang balanced truncation method with extended singular perturbation step.

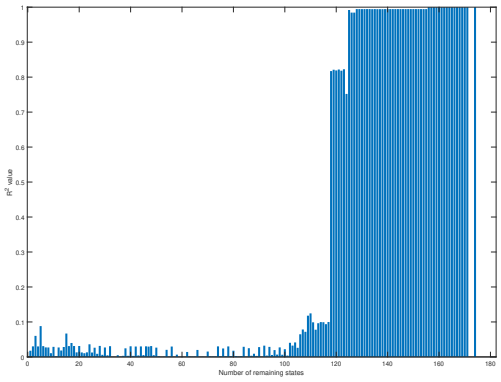

Figure 4.27: **(Model 2, Case 1)**. The R-squared value (bottom) of model reduction iteration using Moore's balanced truncation method with extended singular perturbation step. The reduced model degrades with reduction of model realization less than 156 states.

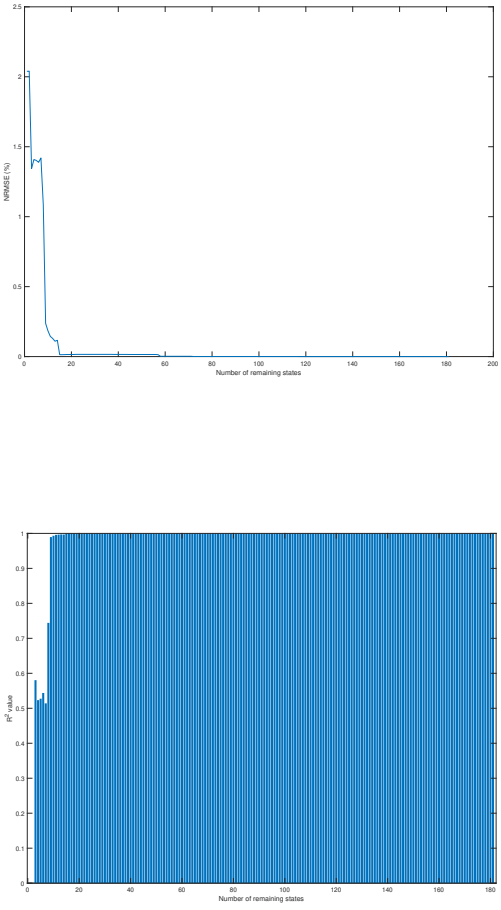

Figure 4.28: **(Model 2, Case 2)**. The Normalized RMSE in percent (top) and R-squared value (bottom) of model reduction iteration using modified Gawronski-Juang balanced truncation method with extended singular perturbation step.

Refocusing back to the results of using the modified Gawronski-Juang frequency-limited method, the perfect confidence of correlation (R-squared more than 0.9995) is found in up to 15 states. The high correlation of R-squared higher than 0.99 occurs up to the realization of only nine states (Figure 4.26. In this case, the the

realization of 15 states for a tip heaving state have a root-mean-square error of 0.01 % (Figure 4.26) in the non-turbulent condition and 0.1 % in the turbulent condition (Figure 4.28). On the other hand, the realization of 9 states has a root-mean-square error of 0.24 % at non-turbulent air and 1.84 % at the turbulent condition.

A further verification step is conducted to analyze the accuracy of the results in the same manner as previously conducted for Model 1 for the non-turbulent case 1. The analysis is firstly by analyzing the scatter plots as in Figure 4.29 for the realization of a reduced model of 180, 100, 20, and 15 states.

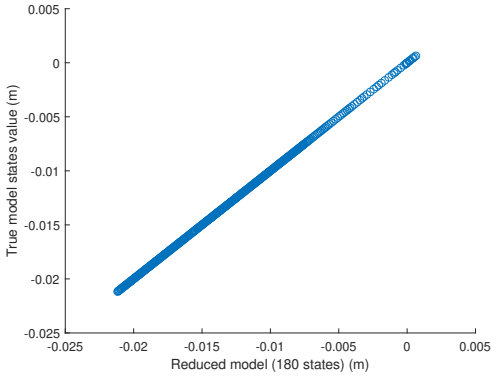

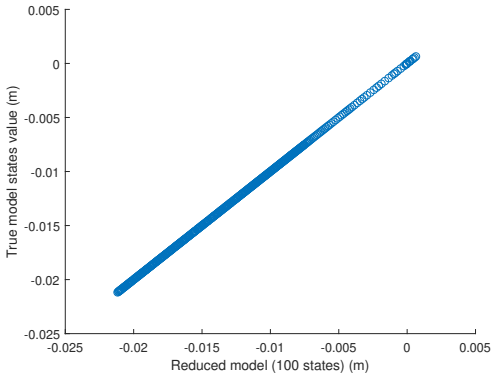

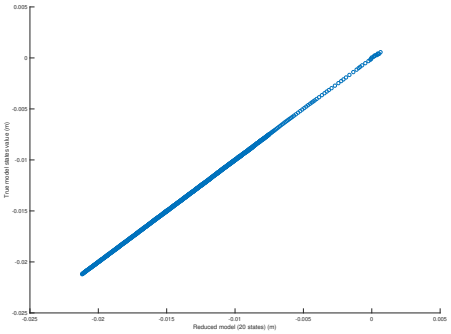

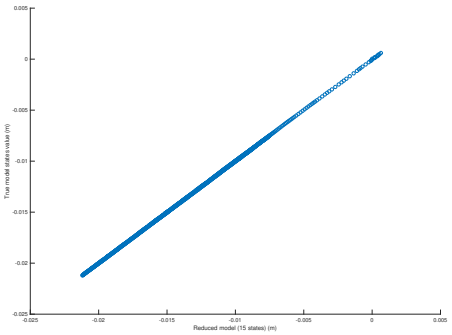

Figure 4.29: **(Model 2, Case 1)**. Scatter plots of true model samples against the reduced model. Evolution of tip heaving state based on model reduction of (from the first to the last) 180, 100, 20, and 15 states.

The scatter plot shows results that the straight linear trend similar to what happens in the reduction evolution of Model 1 when the R-squared value of the reduced model against the true states is high while the error is low. The deviation is not apparent from the scatter plot if there is any in this realization range of reduction model. This is further enhanced with the observation of the location of poles and zeros of the system. In Model 2, the position of the actual model to be more random than that of Model 1. nevertheless, since all the poles are on the left half-plane, the system is also stable. From the realization of 180, 100, 20, and 15 states (Figure 4.30, it can be seen that the evolution of the poles position also occurs. However, the trend of the poles position is roughly the same with the true model where random poles position are staying on the left part or closer to zero and close to touching the neutral imaginary value. The trend can be seen even after the realization is reduced down to 15 states. The analysis is also conducted for the realization of reduced models of 14 states and nine states, as shown in Figure 4.31. As expected from the realization of 5 states in Model 1, the same occurrence also happens in the realization of 14 states as the correlation with the true model starts to degrade. In the realization of 9 states, the degradation of the linear line is more pronounced. It can be seen from the upper-right edge of the plot where the samples at the true model tip heaving state of around zero are reproduced by the reduced model at a different number, therefore creating a straight upward line.

Furthermore, it can be seen that the scatter line becomes more sinusoidal, signifying the small deviation between the value of the true model and reduced model. Nevertheless, contrary to what happens in the reduced realization of 5 states of Model 1, the dispersion of the samples is not far from the trend of linear line. This what may cause that the R-squared and root-mean-square accuracy of the realization of 9 states remains high.

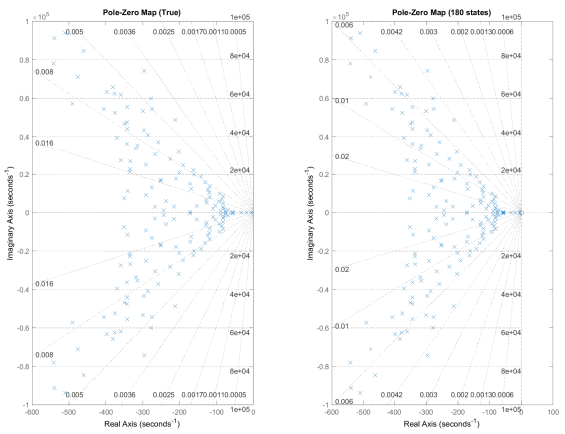

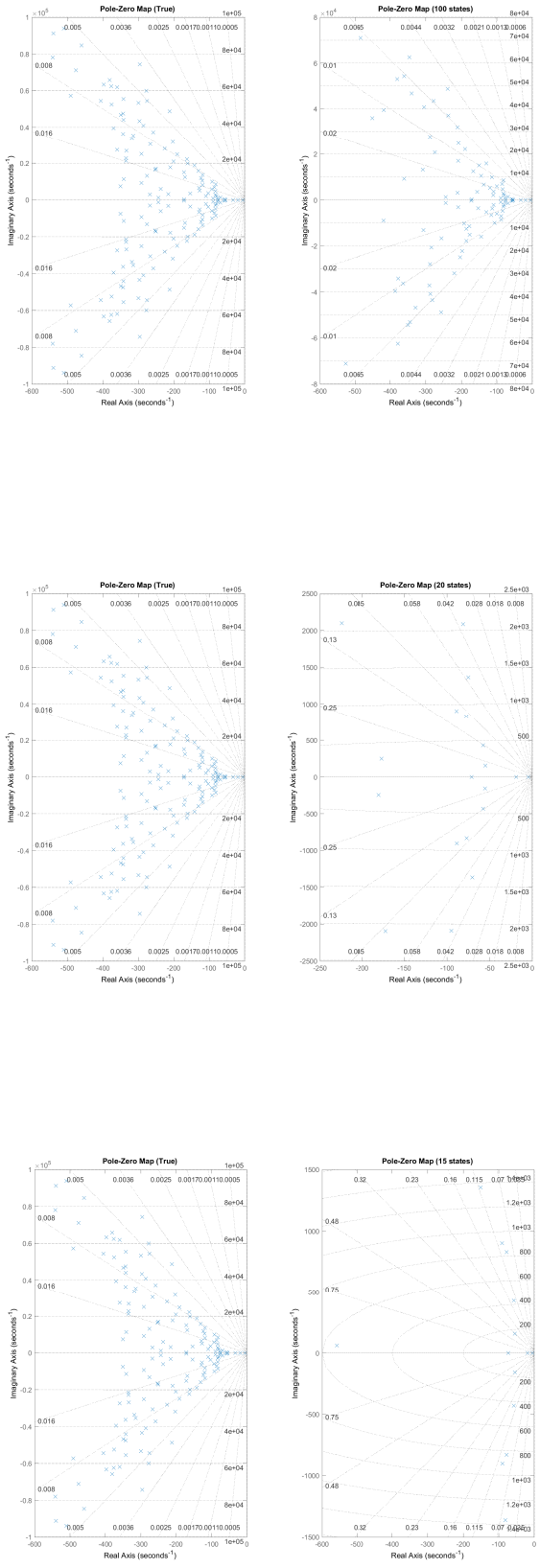

Figure 4.30: **(Model 2, Case 1)**. Pole-zero map of the true model (left) and the reduced model (right). The evolution are the realization of (from the first to the last) 180, 100, 20, and 15 states.

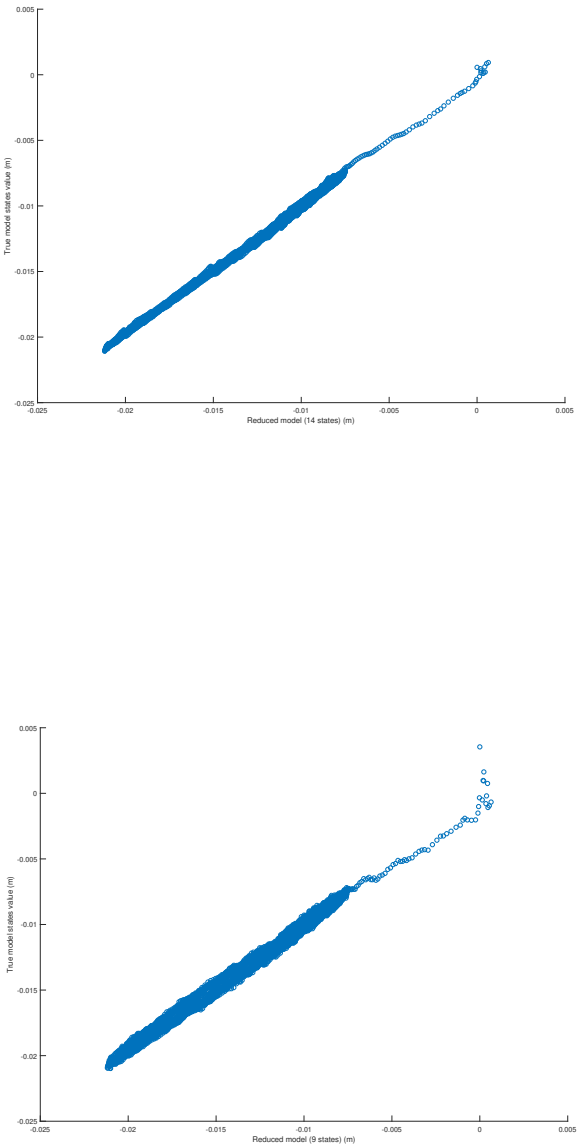

Figure 4.31: **(Model 2, Case 1)**. Scatter plots of true model samples of tip heaving state against the reduced model. The degrading results of realization of 14 (top) and 9 states (bottom).

In order to further confirm the findings obtained in Model 2 Case 1, a similar analysis is also executed for Case 2 with a similar model. The Normalized RMSE and root-mean-square error have been investigated, and the results can again be seen in Figure 4.28. It can be reconfirmed that the minimum reduced model realization with a high confidence coefficient does not change with differing gust air condition. Another confirmation is made from the analysis of the scatter plot of the model realization evolution (Figure 4.32) and pole-zero positioning analysis, as seen in Figure 4.34. Again for the realization of 180, 100, 20, and 15 states of the reduced model, the system can also maintain the linearity, which signifies the perfect replication of the true model by the reduced models. However, for the realizations of 9 states (Figure 4.33, it is observed that for its scatter plot that the correlation between the true model and the reduced model of 9 states is not entirely linear. Instead, it has a sort of exponential correlation closer to zero and at the farthest displacement. This may also support the cause that the reduction model at this number of states is less reliable.

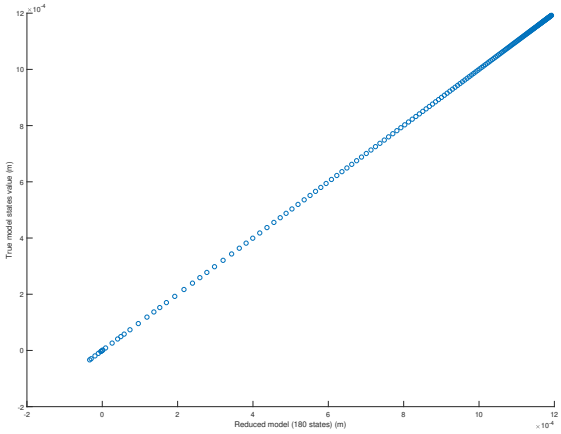
True model states value (m)
Reduced model (180 states) (m)

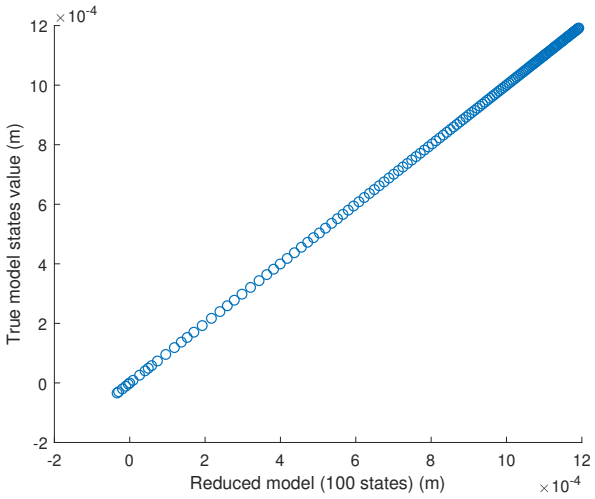
True model states value (m)
Reduced model (100 states) (m)

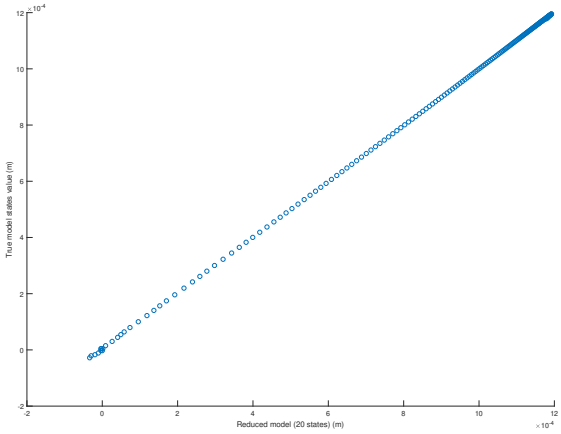
True model states value (m)
Reduced model (20 states) (m)

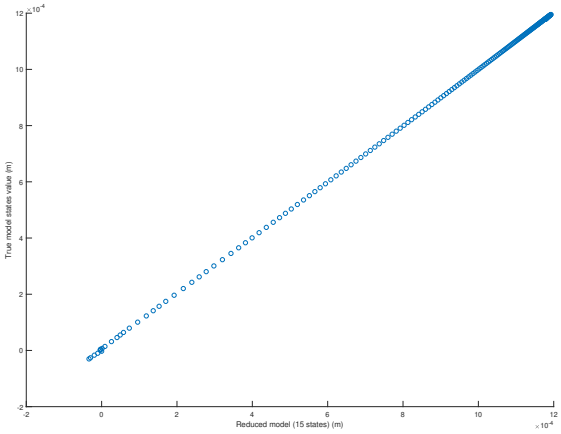

Figure 4.32: **(Model 2, Case 2)**. Scatter plots of true model samples against the reduced model of (from the first to the last) 180, 100, 20, and 15 states.

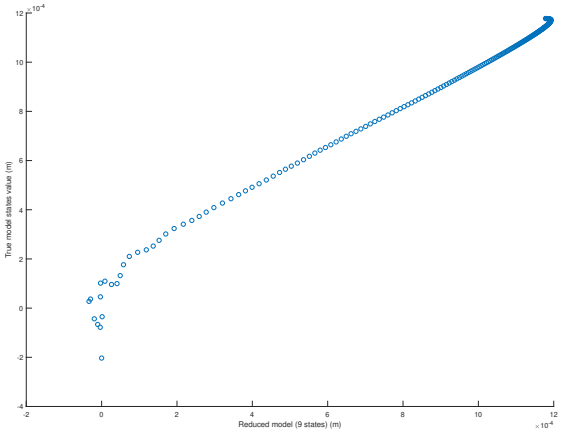

Figure 4.33: **(Model 2, Case 2)**. Scatter plots of true model samples against the reduced model of 9 states. Notice the nonlinearities region at each end of the samples' line.

The results of the pole-zero map are also observed. An interesting result may attract the readers can be seen from the poles and zeros position of the reduced model with a realization of 180 states. It can be observed that there lies a zero that is located at the right half-plane, while the reduced model is a stable one. This zero presence at the right half-plane may coincide with the position of one pole that is very close to the neutral axis. It might be caused by the realization of the determinant of the state-space system, which has some degree of instability in it. However, in order to preserve the stability of the true system, the zero then appears. The occurrence of the zero cancels the instability of the realization, and the poles stay at the left half-plane indicating the stability of the model. The realization of zero in other example realizations in Model 1 and Model 2 never again occurs as the realizations of the reduced model has the poles positioned far enough from crossing to the right half-plane.

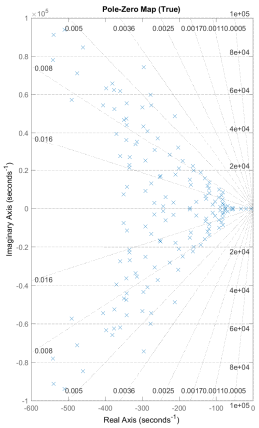
Pole-Zero Map (True)
Imaginary Axis (seconds^{-1})
Real Axis (seconds^{-1})

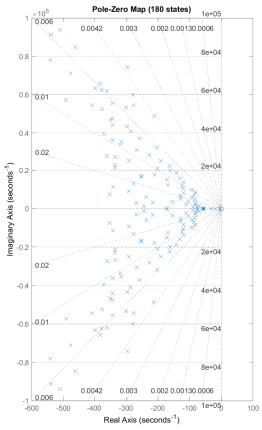
Pole-Zero Map (180 states)
Imaginary Axis (seconds^{-1})
Real Axis (seconds^{-1})

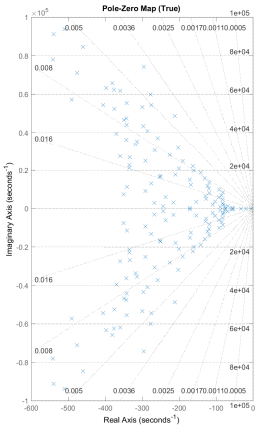
Pole-Zero Map (True)
Imaginary Axis (seconds^{-1})
Real Axis (seconds^{-1})

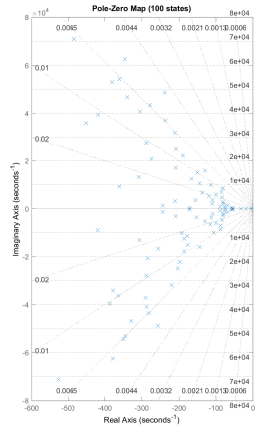
Pole-Zero Map (100 states)
Imaginary Axis (seconds^{-1})
Real Axis (seconds^{-1})

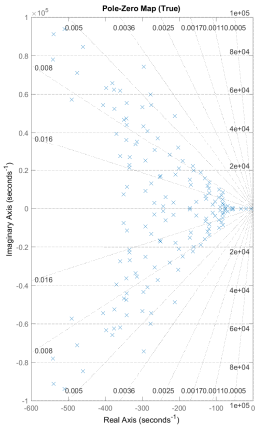
Pole-Zero Map (True)
Imaginary Axis (seconds^{-1})
Real Axis (seconds^{-1})

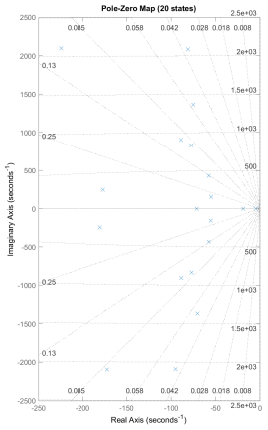
Pole-Zero Map (20 states)
Imaginary Axis (seconds^{-1})
Real Axis (seconds^{-1})

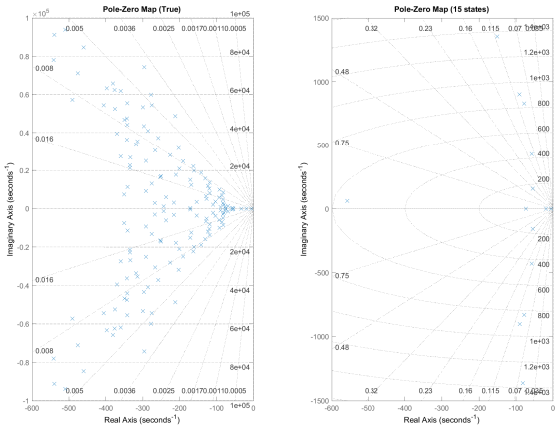

Figure 4.34: **(Model 2, Case 2)**. Pole-zero map comparison between the true model (left) and the reduced model (right). The poles-zeros position evolution in the right is the realization of (from the first to the last) 180, 100, 20, and 15 states.

The model reduction validity will also be observed from the Bode plot frequency. The case is the same as in Model 1 analysis, which is at the tip heaving response against the vertical force input and at the same frequency range of interest. In this case, the sample is taken for the realization of the reduced model with 180, 100, 20, 15, and 14 states. The corresponding figures of Bode magnitude plot frequency for the Model 2 can be seen in the following Figure 4.35-4.39.

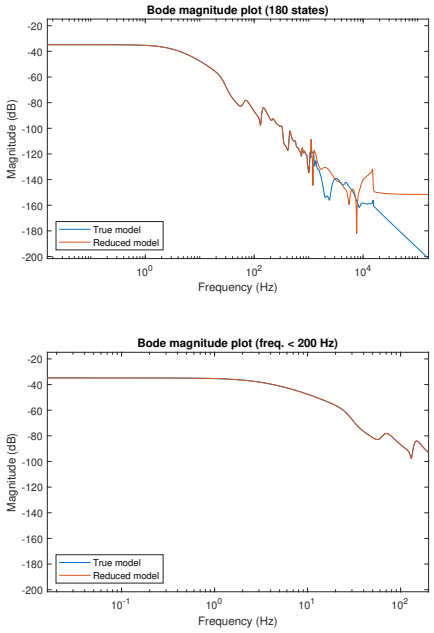

Figure 4.35: **(Model 2)**. Bode magnitude (frequency response) plot of tip heaving response due to the vertical force input. The comparison between the true model and 180-states reduced model for all frequency spectrum (top) and the zoomed-in plot for the frequency range of interest (bottom) in Hertz.

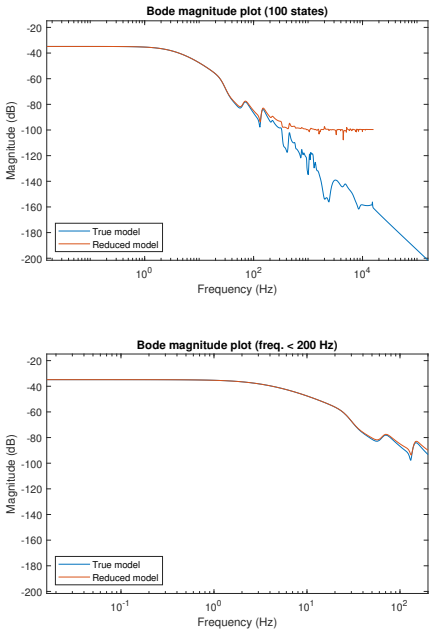

Figure 4.36: **(Model 2)**. Bode magnitude (frequency response) plot of tip heaving response due to the vertical force input. The comparison between the true model and 100-states reduced model for all frequency spectrum (top) and the zoomed-in plot for the frequency range of interest (bottom) in Hertz.

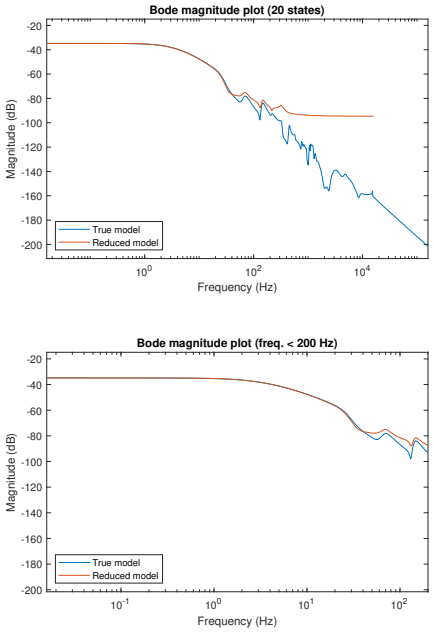

Figure 4.37: **(Model 2)**. Bode magnitude (frequency response) plot of tip heaving response due to the vertical force input. The comparison between the true model and 20-state reduced model for all frequency spectrum (top) and the zoomed-in plot for the frequency range of interest (bottom) in Hertz. Note that the margin of the magnitude between two realizations starts to grow

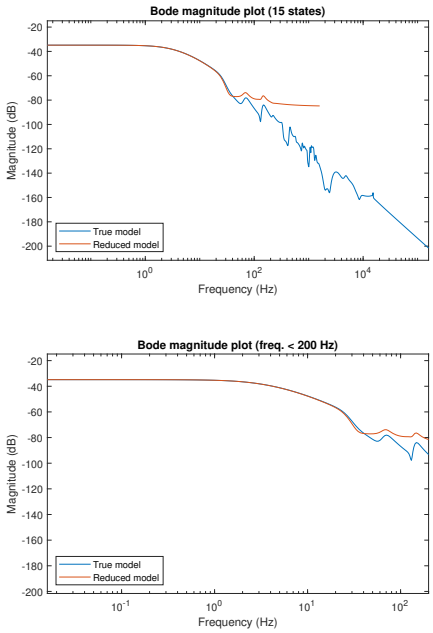

Figure 4.38: **(Model 2)**. Bode magnitude (frequency response) plot of tip heaving response due to the vertical force input. The comparison between the true model and 15-states reduced model for all frequency spectrum (top) and the zoomed-in plot for the frequency range of interest (bottom) in Hertz.

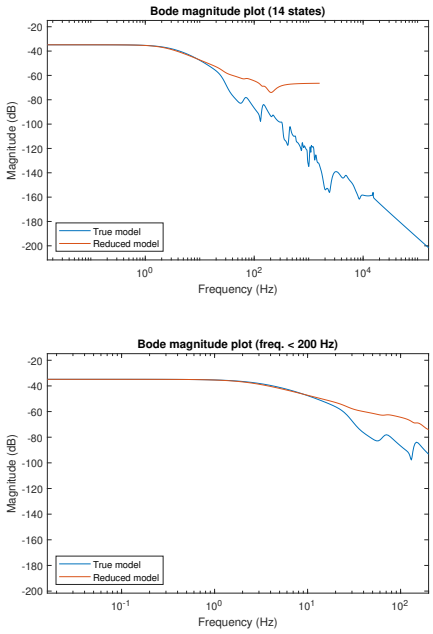

Figure 4.39: **(Model 2)**. Bode magnitude (frequency response) plot of tip heaving response due to the vertical force input. The comparison between the true model and 14-state reduced model for all frequency spectrum (top) and the zoomed-in plot for the frequency range of interest (bottom) in Hertz. Note the separation at the second "downward bend" between the two realizations.

It can be seen that at the realization of 100 states, the bode plot of the reduced model has slightly deviated

from that of the original model. However, it can be seen from the scatter plot that the reduced model can perfectly replicate the dynamic of the true model. The same can be told for the realization of 20 and 15 states, although their magnitude deviates even further from the ground truth. However, it can be seen that despite the deviation, the realizations have similarities with the true model. It can be seen from the frequency response of the realized reduced model of 100, 20, and 15 states at the frequency range of 30 Hz up to 200 Hz. At this range, the true model shows two small magnitude peaks. These peaks can be imitated by the frequency response at the mentioned frequency, albeit imperfectly. The difference in peak value may cause the reduced model realization to behave somehow in a similar way as the true model, hence creating a perfect linear scatter plot. The difference can be told for the realizations of 14 states (Figure 4.38). In this case, the reduced model fails to replicate the two peaks between 30 Hz and 200 Hz. This will then, in turn, shows the degradation in R-squared value and sudden increase in terms of the normalized root-mean-square error value. Therefore, from the Model 1 and 2, it can be seen that looser requirements for the reduced system to fully imitate the original model is that the error and the correlation will be very close to 1 as long as the Bode magnitude plot can replicate the behavior of the true model.

4.4.3 Summary of Model Reduction Results

From the results with two models and two cases for each model, it can be observed that the modified Gawronski-Juang frequency-limited is more reliable in finding the reduced model with the realization of the least number of states compared to other presented balanced truncation method. It can also be concluded that the singular perturbation extension step yields a higher rate of correlation between the reduced model and the true model compared to using Moore's balanced truncation method. The results analysis can be seen by using time-domain and frequency analysis using the means as presented in the previous section. It can be concluded that the reduced model realization succeeds when the scatter plot coordinates of the reduced model point is equal to that of the true model. Furthermore, it can be seen that the successful reduced model shall retain the distribution or the shape of the poles and zeros while also keeping the stability profile of the true model. The Bode magnitude plot also shows that as long as the reduced model frequency response can capture the characteristics of the Bode plot of the original model, a linear line scatters plot can also be achieved, creating looser requirements for the choice of reduced model realization from the frequency response analysis side.

4.5 State and Parameter Estimation Results

After obtaining the reduced model, it is now possible to perform the State and Parameter Estimation following the proposed ROTS estimation algorithm. Given the full condition prepared for the state estimation and parameter in Section 4.3.2, the equation of the state-space to be used for the state estimation part is formulated as

$$\begin{aligned} \dot{\bar{x}} &= \mathbf{A}_{red}\bar{x} + \mathbf{B}_{red}u + \mathbf{G}v \\ y &= \mathbf{C}_{red}\bar{x} + \mathbf{H}w \end{aligned} \tag{4.6}$$

where $\mathbf{G}$ and $\mathbf{H}$ represent the identity process noise and measurement noise matrices respectively whereas v and w represent respectively the process noise for the truncated state and the measurement states. In this case the noise presented is given as in Table 4.3, however it will be downsized to see more clearly whether the state estimation is really converging to its true model value. Way beyond after state estimation is performed at each iteration the parameter will then recursively calculated.

In estimating parameters, it is concerned that the number of measurements that can be obtained through a linear Kalman Filter state estimation routine is 182 states with 78 inputs. The parameters to be estimated are, in this case, the mass, damping, and stiffness of the system. The parameters which relate to the aerodynamic lags need not be calculated since it is formed based on Wagner's indicial function, the geometric properties of the wing, and the airspeed. Hence, once the aerodynamic lag states values are known, the aerodynamic lag influence on the displacement can then be directly calculated and extracted from the equation. The aerodynamic lag influence parameters which relate to angular and translation displacements of the wing sections are absorbed into the parameters to be estimated. For each of the mass, damping, and stiffness matrices, the structure of the matrix is in a dimension of 78 by 78 elements, yielding 6,084 parameters to estimate and a total of 18,252 parameters to be estimated at a single iteration. However, as observed from the matrix structure as in Figure 4.1, the non-zero element is overwhelmed by the number of zero elements. Therefore

there is no need to calculate the zero elements. This further reduces the number of estimated parameters down to 1,332 parameters for each parameter matrix (3,996 in total). In order to form the regression and output matrix, a naive model decomposition is performed. Since all the mass, damping, and stiffness matrices have the exact similar structure, the algorithm of model decomposition can then be formulated as follows.

For the regressor matrix, the remaining parameters will be related to the remaining 156 states of structural displacement and rate. However, the displacement acceleration is not directly obtained from the state estimator. Hence, the acceleration of displacement has to be derived from the attitude rate states. An array of estimated states can then be formed by arranging in the order of acceleration, rates, and attitude. This will yield an array of 234 states. However, for each mass, damping, and stiffness matrices, it is known that there are 78^2 parameters that need to be solved. Therefore, the array will be expanded into a matrix with the number of rows equal to the row of the parameter matrix. The matrix resulted from the expansion of the estimated states array is then retransformed into the form of an array.

Next, the output matrix will be based on the input data of forces and moments for each iteration. As mentioned earlier, the aerodynamic lag influence, which relates to the aerodynamic lag states on the displacement can then be directly calculated and extracted. By subtracting the aerodynamic forces and moments with the extracted aerodynamic lag states related value. In other words, the output matrix for the recursive least-square is

$$u_{k+1} = F_a - K_z z_i \tag{4.7}$$

This leaves only the mass, damping, and stiffness parameters left. In order to estimate the whole elements of the aforementioned matrices, the output matrix needs to be extended. The extension results in the output matrix size are of initial force and moments input number times the number of a row of all parameter matrices by 1. Next, the position of non-zero elements of the parameter is identified (mass, stiffness, and damping) matrices (MATLAB command: *any*), the resulting binary matrix is then transformed into an array with the same length as the extended output matrix. Lastly, the element-wise multiplication between the output array and the identification (binary) array to obtain a true output matrix. Finally, the regressor and output matrices can then be simplified by deleting the regressor and output elements that are zero. Hence only the non-zero elements are calculated, and the estimation will not propagate to the other elements, which are supposedly zero.

4.5.1 Model 1 State Estimation

As the algorithm and parameters are established, The state estimation results can then be obtained. Four states will be observed for each case and model to be observed for the state estimation. These are the root's heaving attitude and angle-of-attack, as well as the tip's heaving attitude and angle-of-attack. The reduced state-space realizations used in both Model 1 and Model 2 cases are 15 states, respectively. In the simulation of Model 1 for both Case 1 (Figure 4.40-4.43) and Case 2 (Figure 4.44-4.47), it can be seen more clearly that the state-estimator by using linear Kalman Filter can converge and follows the trends of all the observed states of the true model, meaning that the state estimation is successful even when the realization of the model is reduced up to only eight percent of the number of states in the end. It can be seen as well that the state estimation at first initial time step is not following the true trends of the true model for all states observed. This is mainly caused by the high covariance value of the states given initially to the state estimation routine. The high covariance value signifies the uncertainty of the observer in pinpointing the true value of the states. However, with the correction of Kalman gain between the true measurement and the estimated value, it can be observed that the values will then converge as the covariance becomes small. The state estimation will then rely more on the estimation rather than measurement as the difference the two values are diminishing. It can also be observed that the noise in the root states is more pronounced compared to the noise realization in the wing sections closer to the tip. It is undoubtedly the case since the displacement of wing sections closer to the root is at a much smaller magnitude for the case of a clamped wing. The same can also be said when observing the noise in the estimation of angle-of-attack compared to the heaving attitude due to smaller change happening in terms of angle-of-attack. This is what causes some graphs appear to be noisier than the others.

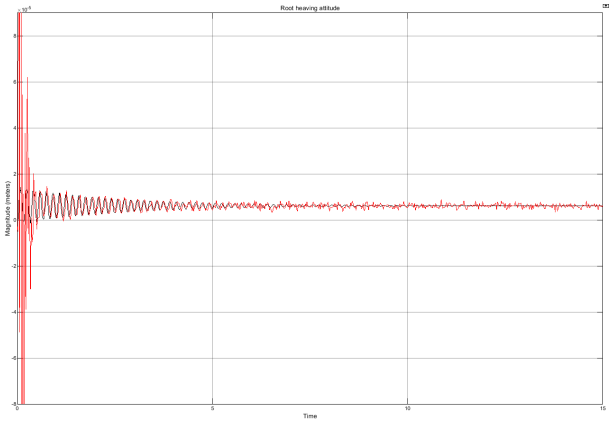

Figure 4.40: **(Model 1, Case 1)**. True attitude (black) against estimated attitude (red) of root heaving attitude.

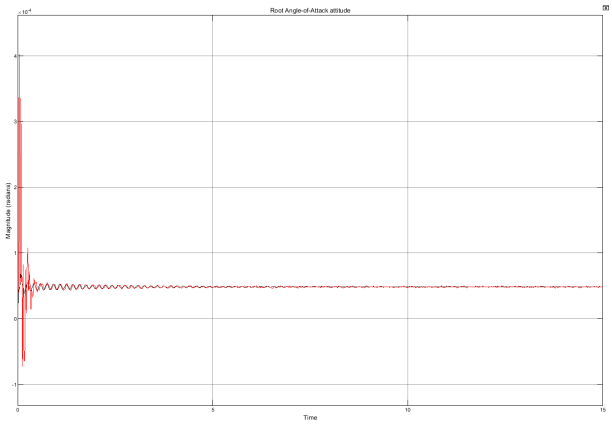

Figure 4.41: **(Model 1, Case 1)**.True attitude (black) against estimated attitude (red) of root angle-of-attack attitude.

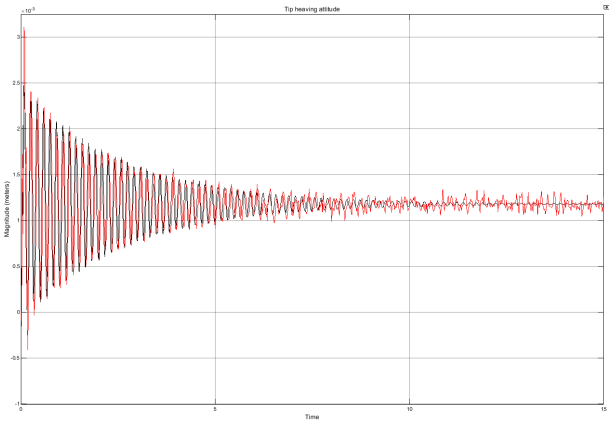

Figure 4.42: **(Model 1, Case 1)**. True attitude (black) against estimated attitude (red) of tip heaving attitude.

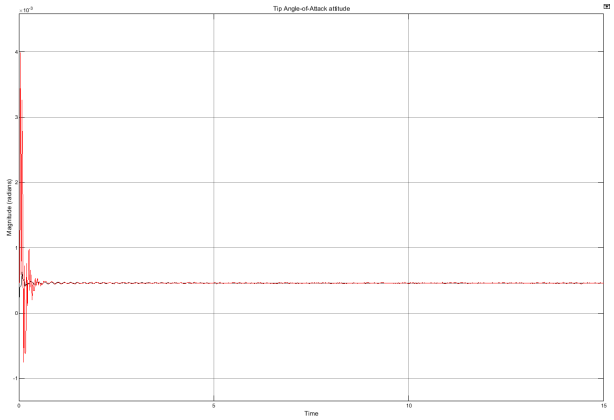

Figure 4.43: **(Model 1, Case 1)**. True attitude (black) against estimated attitude (red) of tip angle-of-attack attitude.

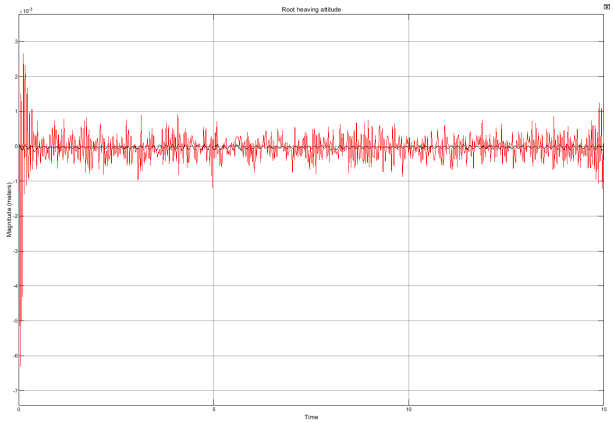

Figure 4.44: **(Model 1, Case 2)**. True attitude (black) against estimated attitude (red) of root heaving attitude.

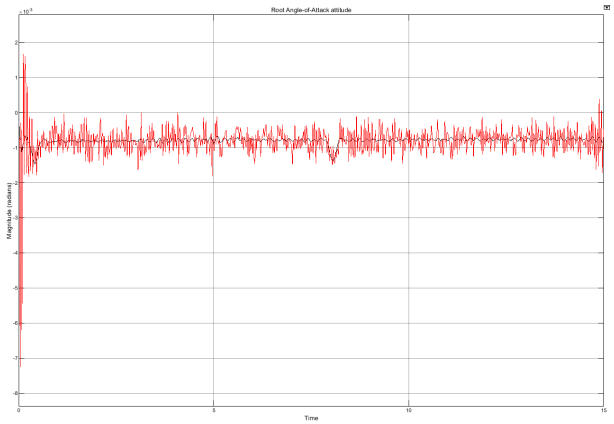

Figure 4.45: **(Model 1, Case 2)**.True attitude (black) against estimated attitude (red) of root angle-of-attack attitude.

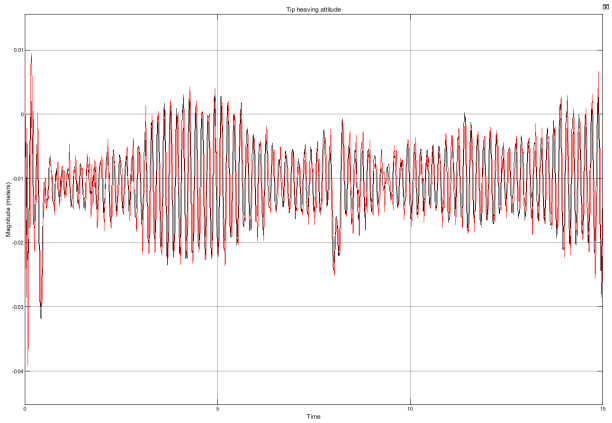

Figure 4.46: **(Model 1, Case 2)**. True attitude (black) against estimated attitude (red) of tip heaving attitude.

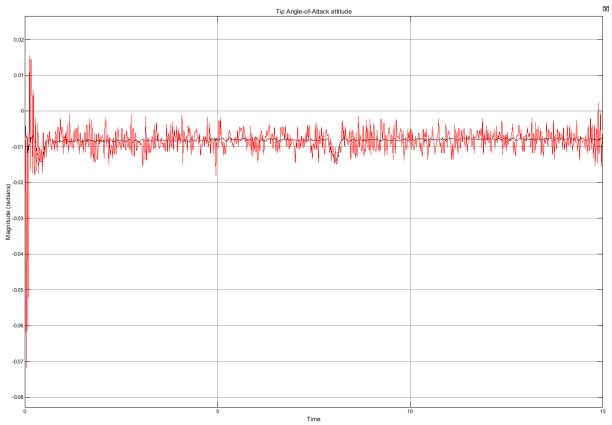

Figure 4.47: **(Model 1, Case 2)**. True attitude (black) against estimated attitude (red) of tip angle-of-attack attitude.

4.5.2 Model 2 State Estimation

Model 2 is again simulated with the same cases as in Model 1. The results of the state estimation can be observed through Figure 4.48-4.51 for the Case 1 and Figure 4.52-4.55 for Case 2. In this case, the realization of the noise is restored to the true value, as filled in in Table 4.4. It can be further observed that the same trend of noise and convergence is similar to the realizations of state estimation of Model 1, where the further wing sections to the root yield a less noisy state estimation. However, it is consistent that the Kalman filter routine presented with the realization of a reduced number of states converges to the true value of the states. The reading of the state estimation should then be able to be improved by introducing a smaller noise for either or both process noise and measurement noise. In terms of measurement errors, this can be further decreased by introducing the camera system with higher resolution such that the area presented for each pixel can become smaller.

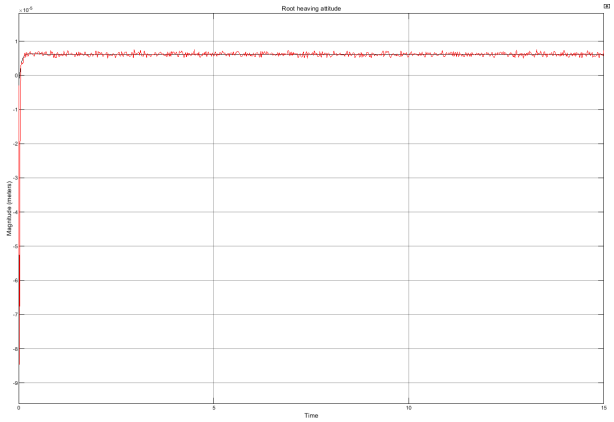

Figure 4.48: **(Model 2, Case 1)**. True attitude (black) against estimated attitude (red) of root heaving attitude.

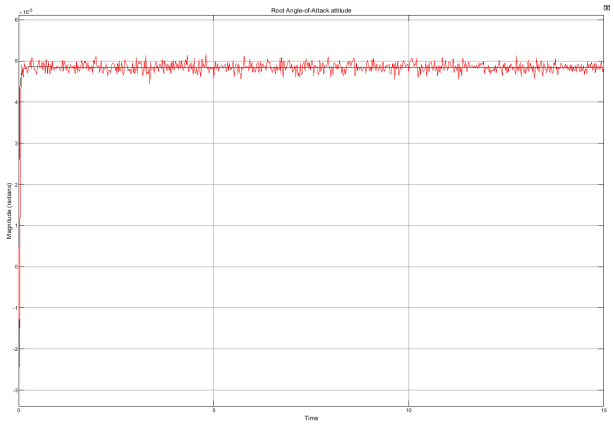

Figure 4.49: **(Model 2, Case 1)**.True attitude (black) against estimated attitude (red) of root angle-of-attack attitude.

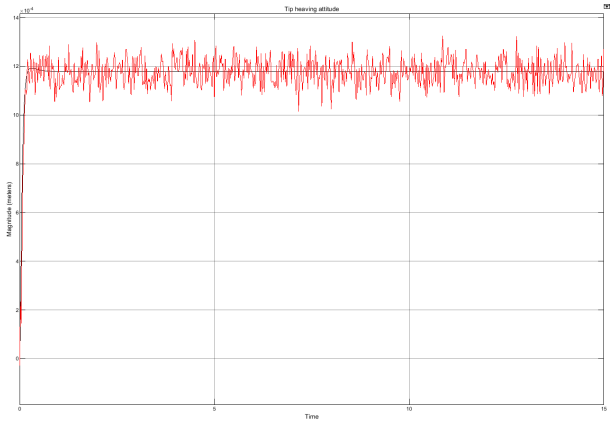

Figure 4.50: **(Model 2, Case 1)**. True attitude (black) against estimated attitude (red) of tip heaving attitude.

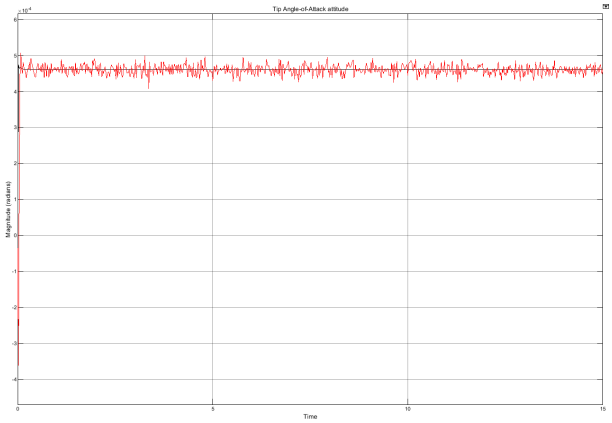

Figure 4.51: **(Model 2, Case 1)**. True attitude (black) against estimated attitude (red) of tip angle-of-attack attitude.

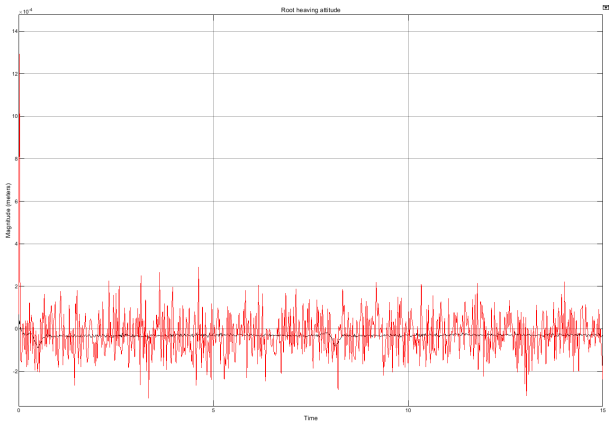

Figure 4.52: **(Model 2, Case 2)**. True attitude (black) against estimated attitude (red) of root heaving attitude.

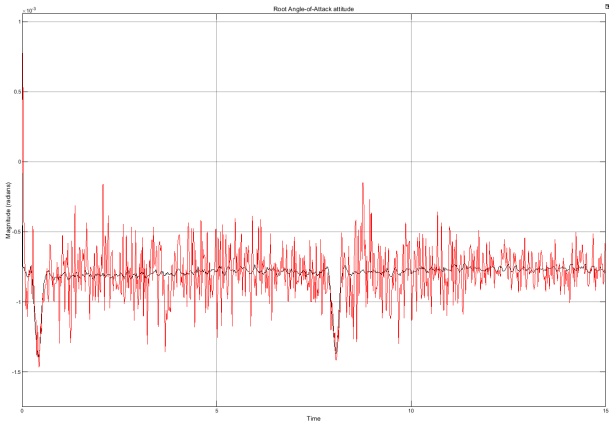

Figure 4.53: **(Model 2, Case 2)**.True attitude (black) against estimated attitude (red) of root angle-of-attack attitude.

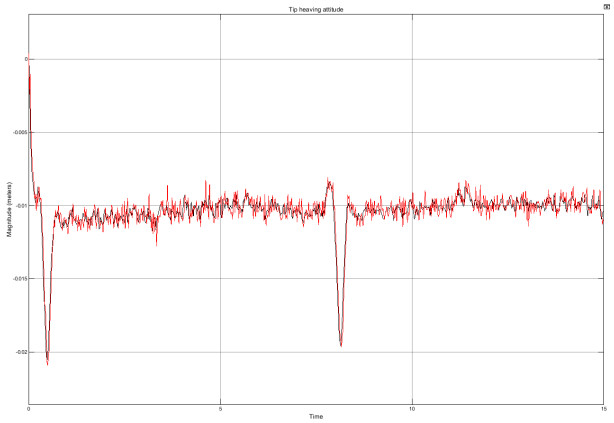

Figure 4.54: **(Model 2, Case 2)**. True attitude (black) against estimated attitude (red) of tip heaving attitude.

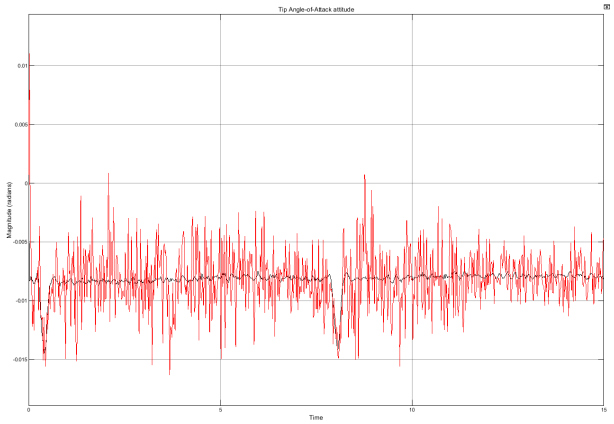

Figure 4.55: **(Model 2, Case 2)**. True attitude (black) against estimated attitude (red) of tip angle-of-attack attitude.

4.5.3 Parameter Estimation

Given the resulting state estimated values for all states, it is then possible to execute the parameter estimation based on the estimated value using the established parameter, as established in Section 4.3.2. In general, the accuracy analysis of the recursive least-square value is conducted by looking at the convergence and the converged value of the parameters compared to a reference. However, such an analysis method is almost impossible to do as there are thousands of parameters to analyze, while the estimated parameter values have also affected the calculation of other parameters, as shown by the structure of the parameter matrix. Furthermore, the end goal of the analysis is to yield an accurate state-space representation of the aeroelastic structure. The accuracy can be observed through the calculation of the poles or eigenvalues position of the reconstructed state-space. Given enough simulation time-space, the parameter value should then converge. This also eases the effort to measure whether the final objective to identify the parameters obtained through the proposed methods is achieved in the numerical simulation condition.

In doing the results analysis for parameter estimation results, only Case 2 is analyzed since it allows the calculation in all six degrees of freedom while the condition of force and moments presented for Case 1 only applied for pitching moment and vertical force, therefore it can be seen that no matter where the initial value of the parameter, it will then yield a zero value for all parameters related to other degrees of freedom other than heave and pitch. This then renders the calculation widely inaccurate for the mentioned case. In order to analyze the eigenvalues of the system, the **A** matrix will be reconstructed based on the aerodynamic lags' influence as well as the estimated structural mass, damping, and stiffness matrices yielded by the Recursive Least square routine.

As seen in Figure 4.56 and 4.57 for Model 1 and Model 2, respectively, it can be seen that the calculation of parameter still yields inaccurate results. The results show that the proposed parameter identification routine is still unable to imitate the poles' position of the true model or by at least maintaining the estimated poles at the left half-plane. The main objective of the system identification in the controller scheme is then reviewed for the reflection of the results, it can be seen that the final objective of yielding an accurate representation of the aeroelastic system is still not achieved due to the occurring results despite the convergence of the state estimation results. The results show different characteristics from the true models where all poles lie on the left-half plane. The finding should become the ground for the next analysis in improving the Two-Step Method for structural system identification.

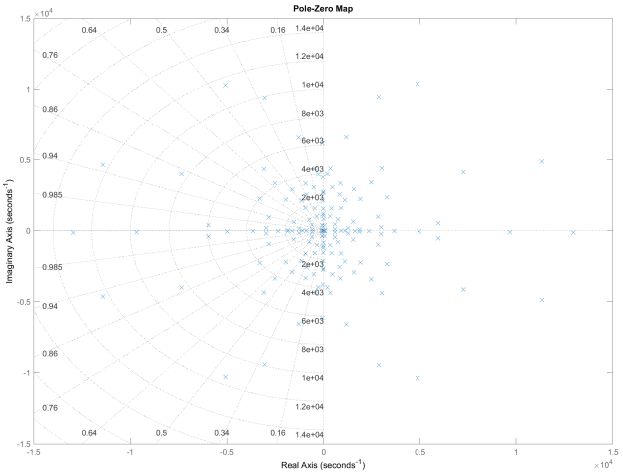

Figure 4.56: **(Model 1, Case 2)**. Pole-zero map of the rebuilt system.

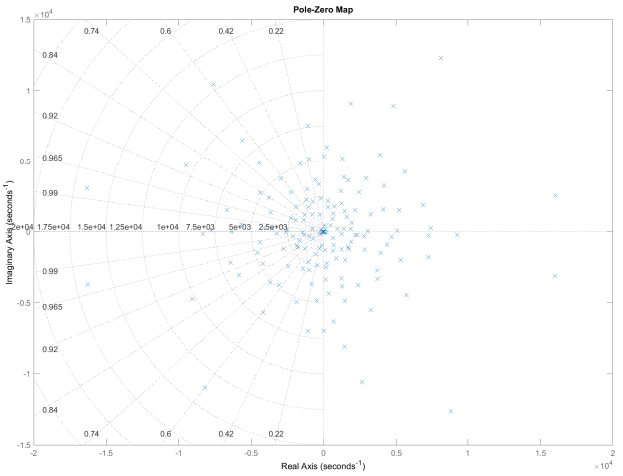

Figure 4.57: **(Model 2, Case 2)**. Pole-zero map of the rebuilt system.

4.5.4 Summary of State and Parameter Estimation Results

From the results with both models with the parameters established for state and parameter estimation in the given numerical simulation condition, the state estimation with the proposed reduced-order model shows

converging results to the true model in all simulation cases. The parameter estimation has also been conducted, and the results are analyzed by means of pole-zero mapping. From the overall results, it can be concluded that the proposed method is able to estimate correctly to the true displacement of each wing section. Reflecting on the main objective of the system identification in the controller scheme, the final objective of yielding an accurate representation of the aeroelastic system is still not achieved as the results show different characteristics from the true models where all poles lie on the left-half plane. Further analysis is recommended to be focused on constraining the parameter estimation in order to ensure that the stability of the true model can be retained to yield an accurate solution for the aeroelastic controller feedback.

4.6 Concluding Remarks

Based on the summary of the model reduction and system identification part of the proposed ROTS method., the results reveal that the proposed modified Gawronski-Juang frequency limited method succeeds in obtaining reduced model realization with small root-mean-square error of 2.63 % with realization of 6 states and 1.84 % error with realization of 9 states for Model 1 and 2 respectively compared to the true model at gust condition. The resulting reduced-order model realizations are then used for both respective models as the observing state-space to calculate the state estimation with the property of simulation accounted in Subchapter 4.3.2.

The chapter is dedicated to preliminarily answer the third and fourth sub-research questions (**RQ 1.3** and **RQ 1.4**). The state estimation with the reduced-order model shows converging results to the true model in all simulation cases. However, parameter estimation has also been conducted, and the results are analyzed by means of pole-zero mapping. It can be seen that the final objective of yielding an accurate representation of the aeroelastic system is still not achieved as the results show different characteristics from the true models where all poles lie on the left-half plane. In order to more fully answer the two remaining sub-research questions, the next chapter will analyze the supporting simulation cases to answer the cases presented.

Chapter 5

Additional Results

In this chapter, more simulation cases are presented in order to execute the sensitivity analysis of the proposed methods. In other words, the writer tries to identify what are the possible parameters that may cause differences in realization results. Furthermore, the effects that the differences will have on the model reduction and state and parameter estimation of structural system identification in the proposed ROTS method. Four critical parameters will be changed from its initial value in the previous chapter, namely the damping ratio, airspeed, gust frequency, and sampling rate. In this case, the model that will be used is Model 2, with the reduced-model realization of 15 states using the modified Gawronski-Juang frequency-limited balanced truncation method. The reasoning is since the model shows a less harmonic and random displacement movement instead of harmonic dampened oscillatory displacement as in Model 1. Furthermore, the 15-state-reduced model realization is used as the results obtained from the previous chapter shows that the perfect simulation result can be attained up to this realization. Therefore, as things are cleared, it is proposed the additional study case for the proposed ROTS method to answer the remaining part to fully answer the research question of **RQ 1.3** and **RQ 1.4**. The simulation cases are tabulated in the following table.

Table 5.1: Additional Analysis Cases

Model type	Case	V_{air} (m/s)	Gust freq.	Damping Ratio	Sampling Rate
Model 2	3	13.6	4 Hz	0.001	50 Hz
	4	13.6	4 Hz	0.05	50 Hz
	5	13.6	8 Hz	0.01	50 Hz
	6	25.6	4 Hz	0.01	50 Hz
	7	25.6	8 Hz	0.01	50 Hz
	8	25.6	10 Hz	0.01	50 Hz
	9	13.6	4 Hz	0.01	25 Hz
	10	13.6	4 Hz	0.01	100 Hz

5.1 Results Discussion

5.1.1 Damping Ratio

In Case 3 and 4, the damping ratio is varied to 0.001 and 0.05. The variation is to follow the observation by Asjes [2] and also [77] that the structural damping for the typical wing is found around the mentioned number range. Therefore the Case 3 is representation to a weakly dampened structure while Case 4 represents a heavily dampened structure. Firstly, the effect of the damping ratio towards the realization of the model reduction using the proposed modified Gawronski-Juang frequency limited method. First, the normalized RMSE and R-squared value analysis are conducted to obtain the optimal realization of the reduced model with the least number of states. Then the realization of the reduced model is then planted into the Two-Step Method routine.

In Case 3, it can be seen from Figure 5.1 that the perfect correlation between the reduced model and the true model is obtained up to a reduced model realization of 39 states. The realization of the reduced model has an R-squared value of 0.95 up to the realization of 9 states. For the reduced model realization of 39 states, the Two-Step method of state and parameter identification is conducted recursively. The results of the state estimation for root's heaving and angle-of-attack, as well as the tip's heaving and angle-of-attack, is described in Figure 5.2. In general, despite the random spikes occurring in tracking the states, it can be seen that the results converge to the true model states values, signifying the success of the model reduction. Nevertheless, the reconstructed state-space matrix shows the instability behavior, as presented in Figure 5.3.

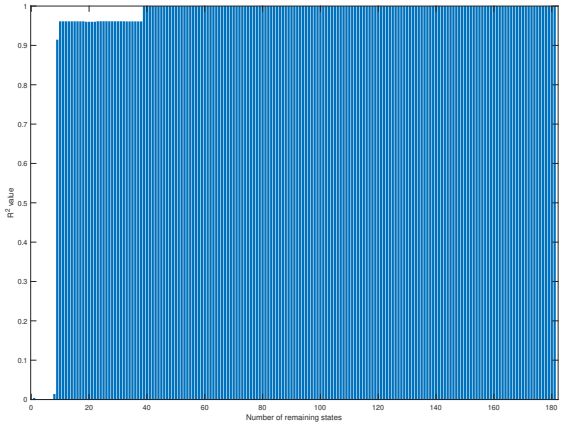

Figure 5.1: **(Model 2, Case 3)**. Achieved R-squared value of reduced model compared to the original system by modified Gawronski-Juang balanced truncation method.

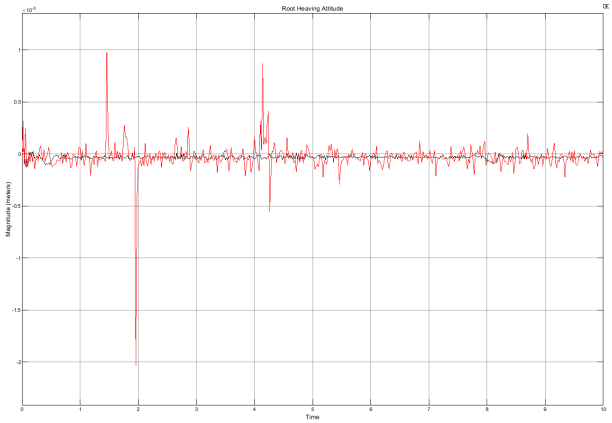

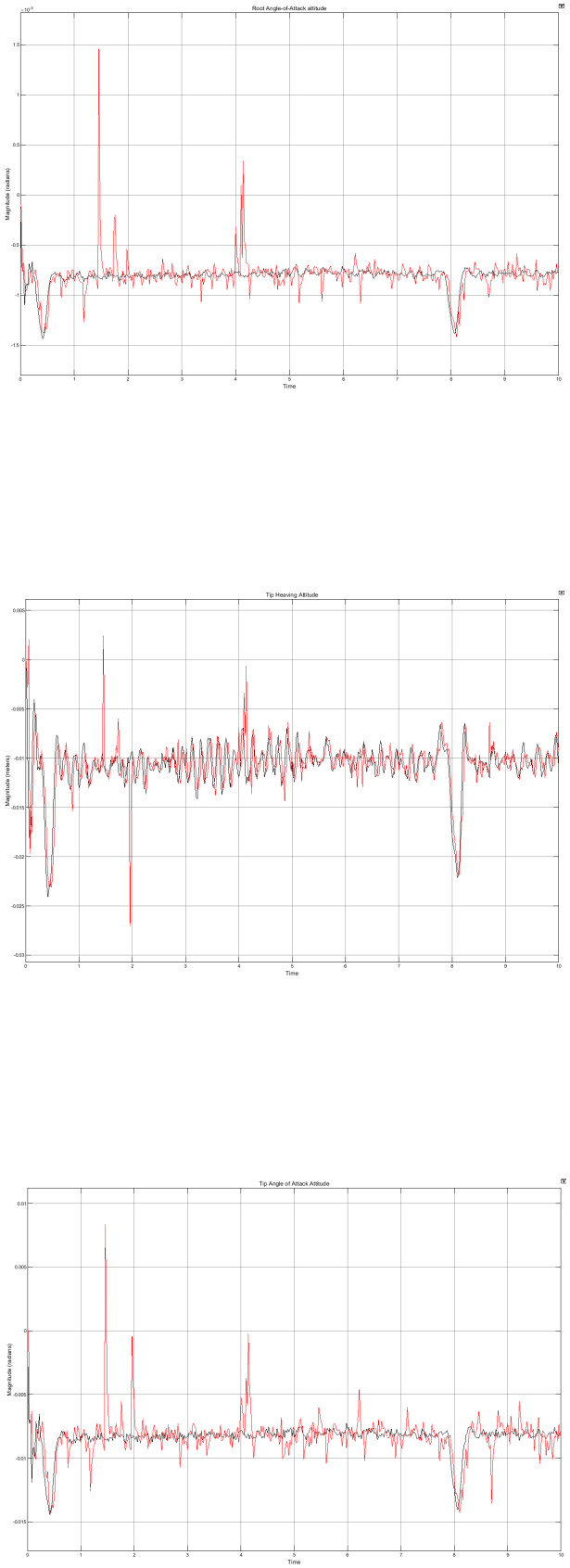

Figure 5.2: **(Model 2, Case 3)**. Value comparison of true attitude (black) and estimated attitude (red) of (from the first to the last) root heaving attitude, root angle-of-attack, tip heaving attitude and tip angle-of-attack. Reduced realization of 39 states.

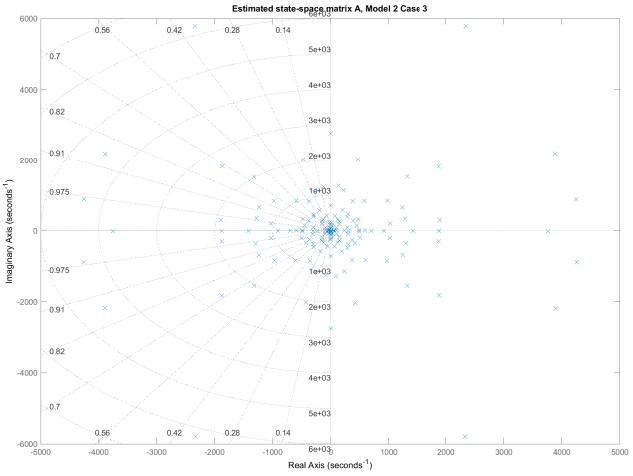

Figure 5.3: **(Model 2, Case 3)**. Estimated eigenvalues position of state-space matrix **A**.

Moving to Case 4, a similar analysis is conducted it is shown that the true model realization can be reduced up to only three states remaining and yields a perfect correlation as shown in Figure 5.4. The reduced model realization of 3 states is then used to obtain the state estimation value. It can be seen that the estimated state's value also converges to its true value (Figure 5.5). The eigenvalues of the estimated state-space matrix can be seen in Figure 5.6, which yields the same results as other parameter estimation in other cases. Hence, based on the realization of Model 2 in the previous chapter, it can be seen that the damping realization affects significantly to the reduced model realization that, the more dampened the system, the less number of states needed in order to attain a perfect correlation as in the true model. However, the parameter estimation results are not affected by the change in the damping terms.

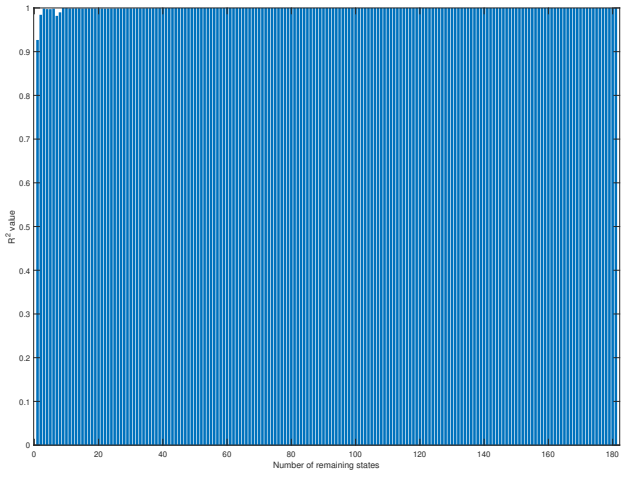

Figure 5.4: **(Model 2, Case 4)**. Achieved R-squared value of reduced model compared to the original system by modified Gawronski-Juang balanced truncation method.

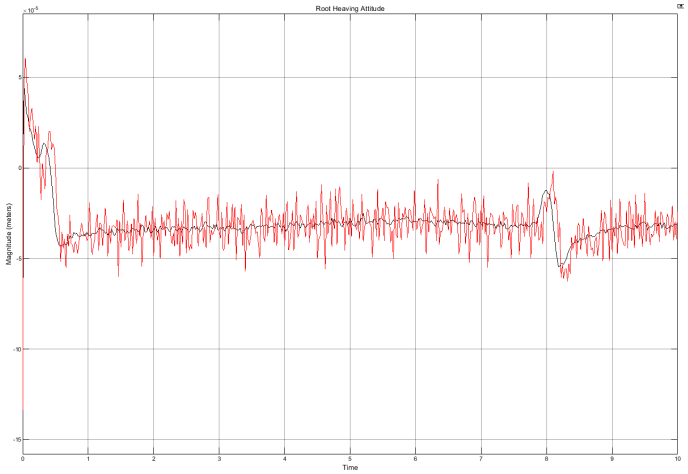
Root Heaving Attitude
Magnitude (meters)
Time

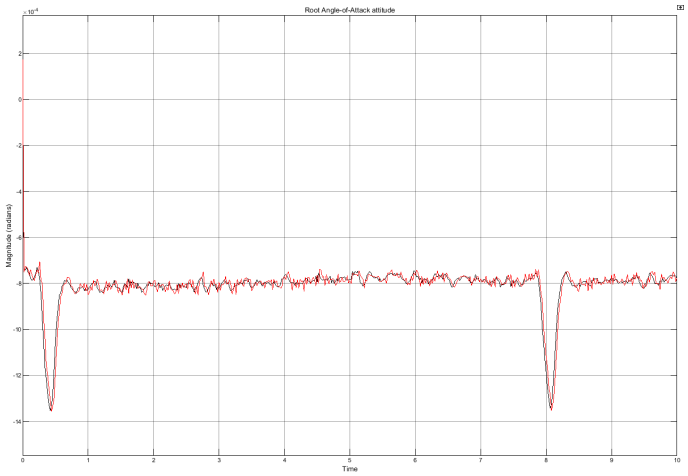
Root Angle-of-Attack attitude
Magnitude (radians)
Time

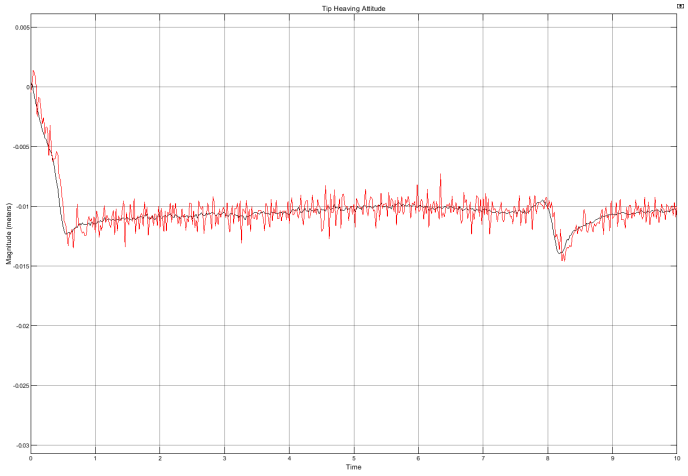
Tip Heaving Attitude
Magnitude (meters)
Time

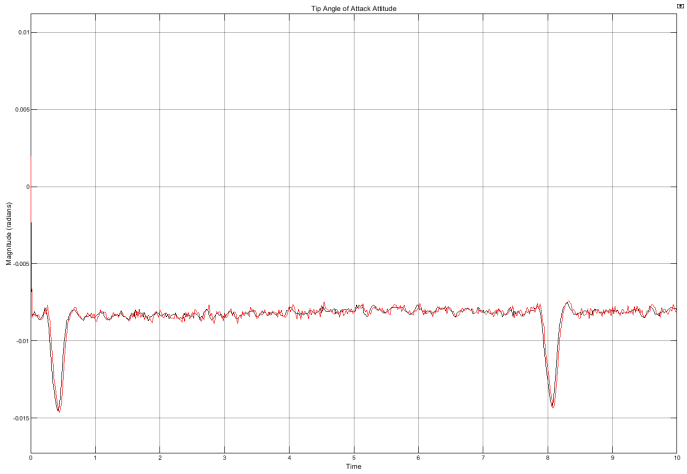

Figure 5.5: **(Model 2, Case 4)**. Value comparison of true attitude (black) and estimated attitude (red) of (from the first to the last) root heaving attitude, root angle-of-attack, tip heaving attitude and tip angle-of-attack. Reduced realization of 3 states.

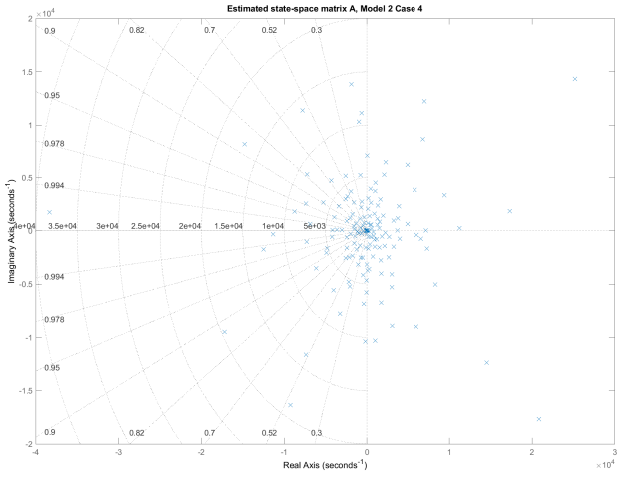

Figure 5.6: **(Model 2, Case 4)**. Estimated eigenvalues position of state-space matrix **A**.

5.1.2 Gust Realization

The gust realization influence to the proposed method realization is also investigated by simulating the Case 5-8 for Model 2. First of all, the normalized RMSE and R-squared values are again then calculated. It is observed that for all cases of gust realization that the number of states for the minimal realization of the reduced model is kept at 15 states for the same damping ratio despite the degrading normalized RMSE for the reduced model at the aforementioned number of states. The Figures for the state estimation and parameter estimation results for Case 5 until Case 8 are tabulated as follows.

Table 5.2: Figures List for Different Turbulence Realizations

Model type	Case	State Estimation	Parameter Estimation
Model 2	5	Figure 5.7	Figure 5.8
	6	Figure 5.9	Figure 5.10
	7	Figure 5.11	Figure 5.12
	8	Figure 5.13	Figure 5.14

It can be seen from the comparison among the cases presented that the realization of the noise is much more prominent with the lower frequency of the gust realization. The state estimation results show that the noise effect is much pronounced in the wing section closer to the root due to poor displacement such that the estimation results are predominantly noisier. Moreover, the noise is also more pronounced when the state's values are flatter. Although it is hard to pinpoint due to the great deviation at the beginning of the simulations, the root-mean-square error on the root is generally smaller compared to that on tip. However, the normalized root mean square shows that the NRMSE value is tabulated as follows.

Table 5.3: Normalized Root-Mean Square Values

Model type	Case	NRMSE Root Heave	NRMSE Root AoA	NRMSE Tip Heave	NRMSE Tip AoA
Model 2	5	3.67 %	38.5%	4.07%	8.14%
	6	8.57%	38.0%	4.51%	41.29%
	7	753%	12.8%	6.5%	10.70%
	8	871%	7.5%	7.08%	10.60%

In other words, the displacements that occur are insignificant when the change in force and moment occurs. In conclusion, it can be concluded that the gust frequency has an effect to the lower level of noise in state estimation calculation, however, the gust by itself less significantly alters the value of R-squared and normalized RMSE of the time response of the states of the reduced model against the true states value, therefore the minimum realization of reduced model without the change in damping ratio is still at 15 states. By comparing the results of Case 5 and 7, where the gust frequency is the same with different airspeed. It can be seen as well that the higher airspeed also affects the state measurement reading to appear less noisy at a higher airspeed, in particular for the angular state of wing section closer to the root.

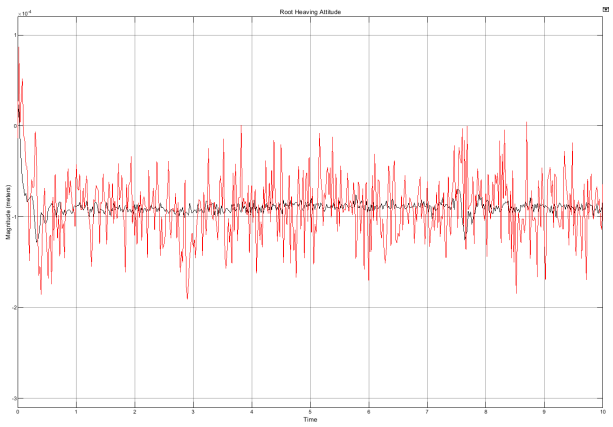

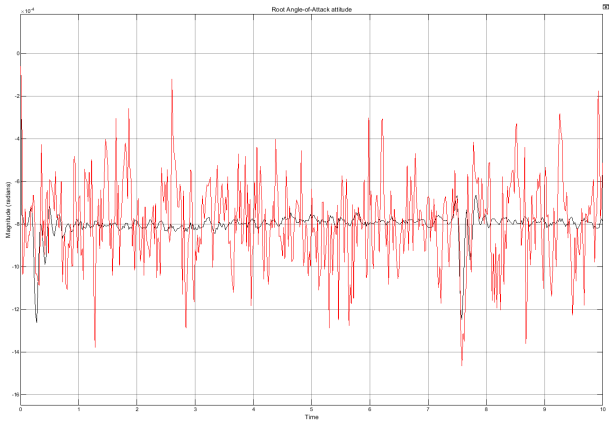
Root Angle-of-Attack attitude
Magnitude (radians)
Time

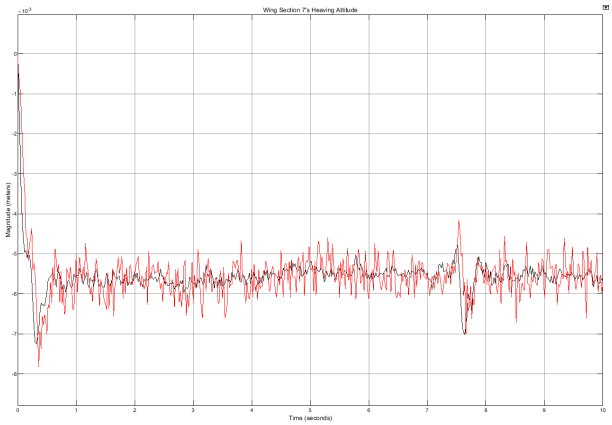
Wing Section 7's Heaving Attitude
Magnitude (meters)
Time (seconds)

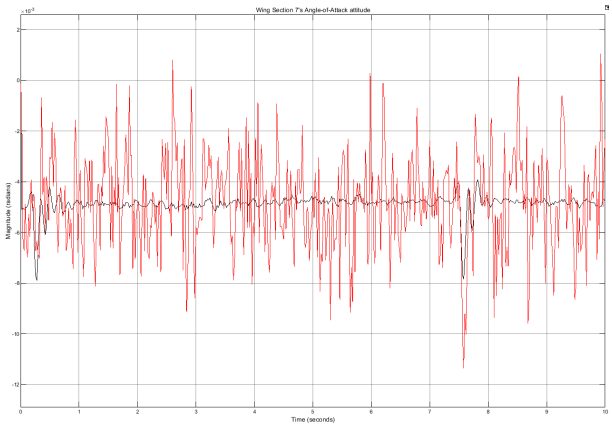
Wing Section 7's Angle-of-Attack attitude
Magnitude (radians)
Time (seconds)

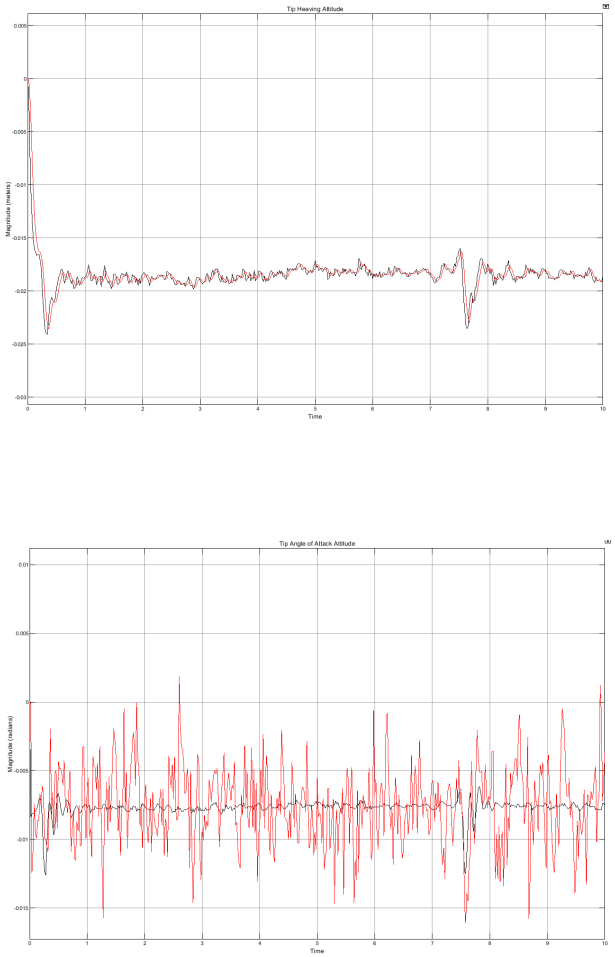

Figure 5.7: **(Model 2, Case 5)**.Value comparison of true attitude (black) and estimated attitude (red) of (from the first to the last) root heaving attitude, root angle-of-attack, middle wing section's heaving attitude, middle wing section's angle-of-attack, tip heaving attitude and tip angle-of-attack. Reduced realization of 15 states.

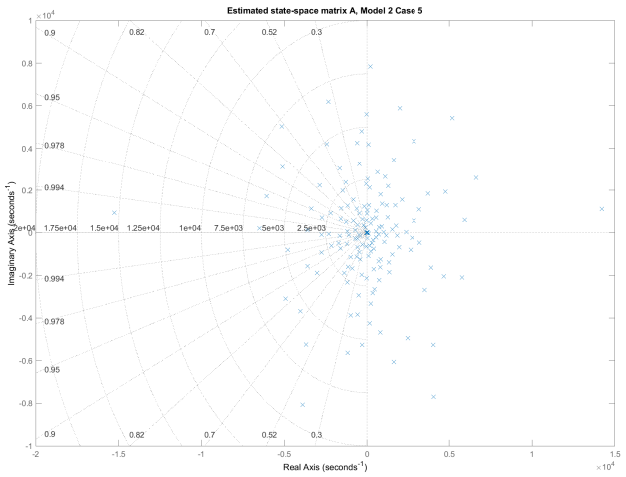

Figure 5.8: **(Model 2, Case 5)**.Estimated eigenvalues position of state-space matrix **A**.

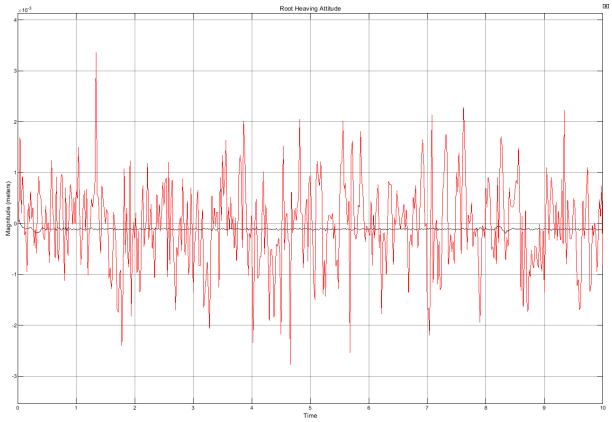
Root Heaving Attitude
Magnitude (meters)
Time

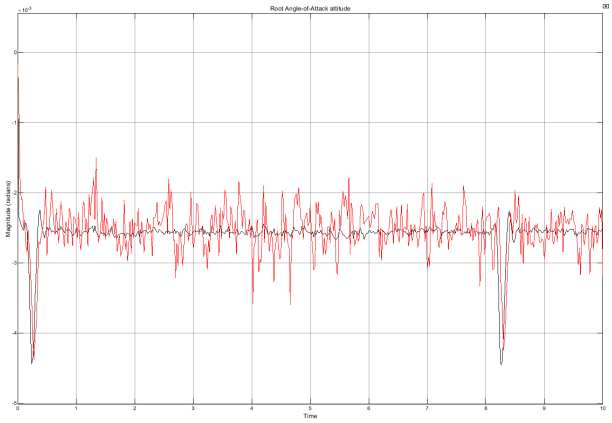
Root Angle-of-Attack attitude
Magnitude (radians)
Time

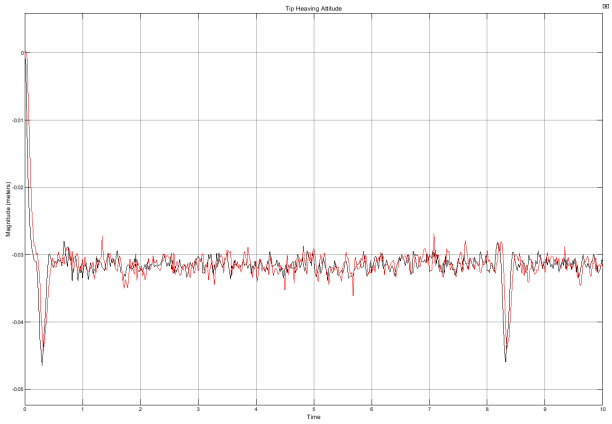
Tip Heaving Attitude
Magnitude (meters)
Time

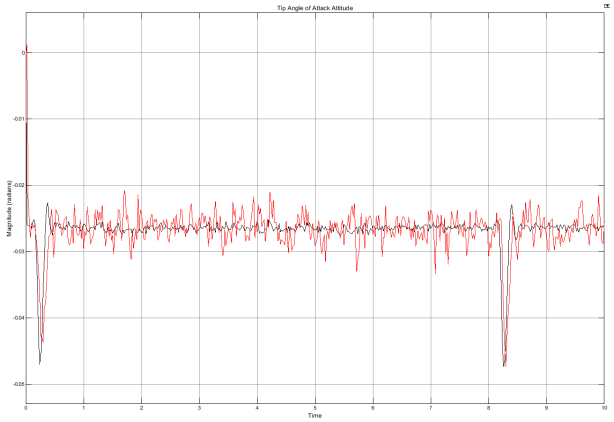

Figure 5.9: **(Model 2, Case 6)**. Value comparison of true attitude (black) and estimated attitude (red) of (from the first to the last) root heaving attitude, root angle-of-attack, tip heaving attitude and tip angle-of-attack. Reduced realization of 15 states.

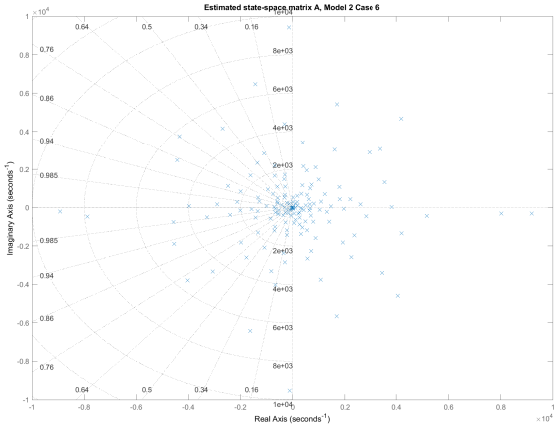

Figure 5.10: **(Model 2, Case 6)**. Estimated eigenvalues position of state-space matrix **A**.

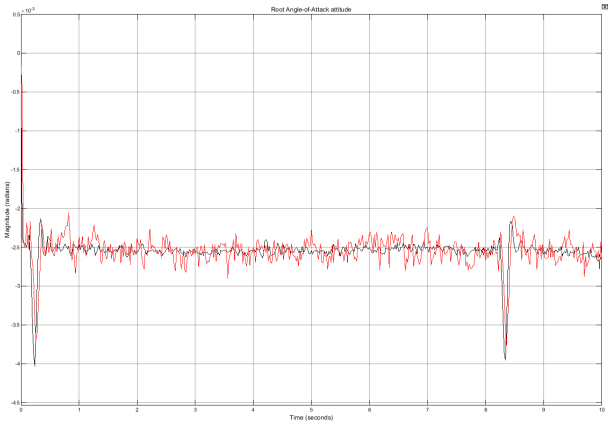

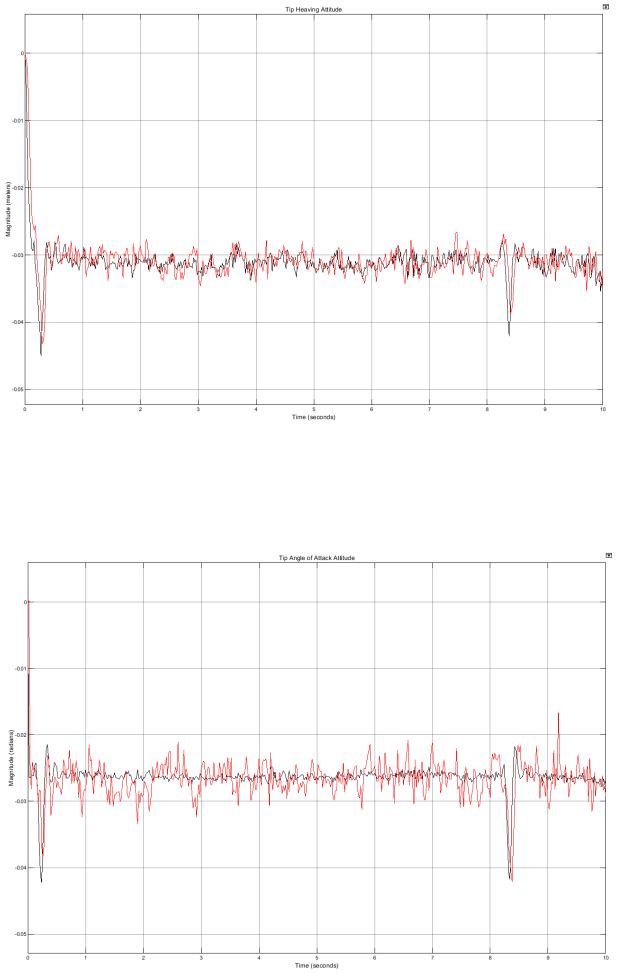

Figure 5.11: **(Model 2, Case 7)**.Value comparison of true attitude (black) and estimated attitude (red) of (from the first to the last) root angle-of-attack, tip heaving attitude and tip angle-of-attack. Reduced realization of 15 states.

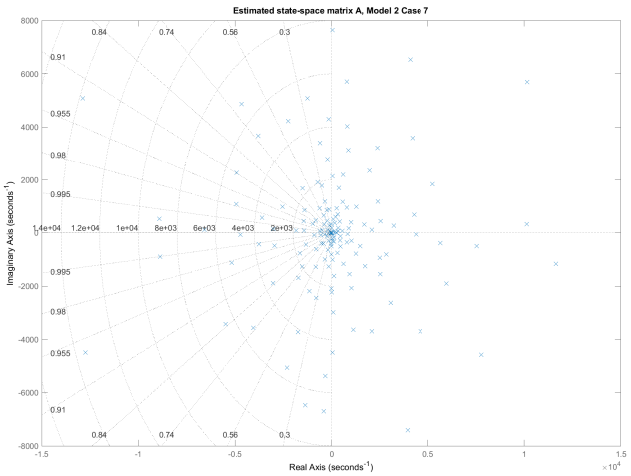

Figure 5.12: **(Model 2, Case 7)**. Estimated eigenvalues position of state-space matrix **A**.

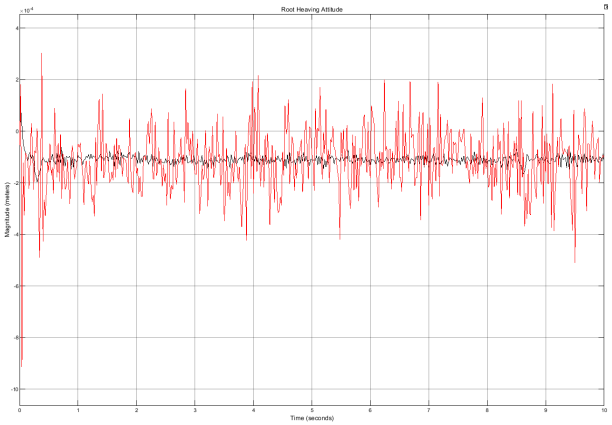
Root Heaving Attitude
Magnitude (meters)
Time (seconds)

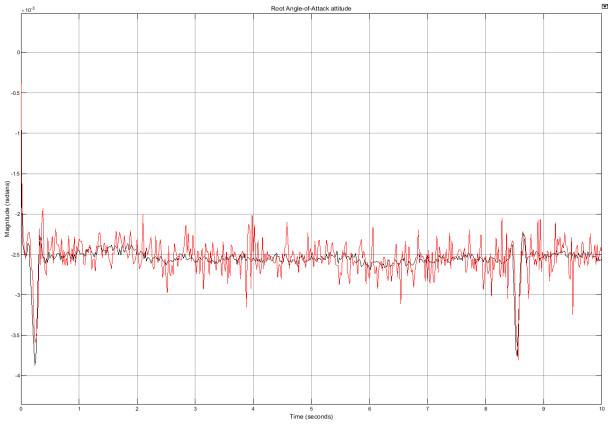
Root Angle-of-Attack attitude
Magnitude (radians)
Time (seconds)

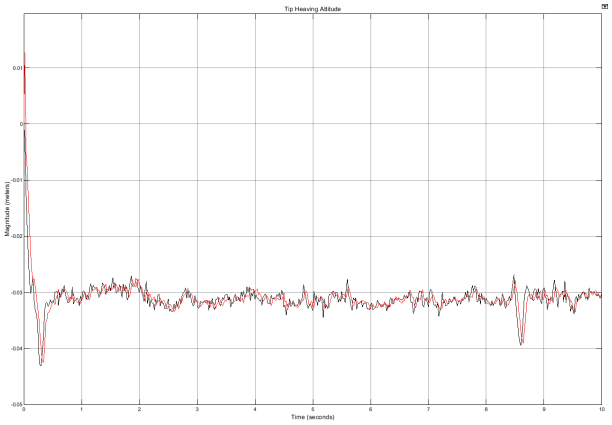
Tip Heaving Attitude
Magnitude (meters)
Time (seconds)

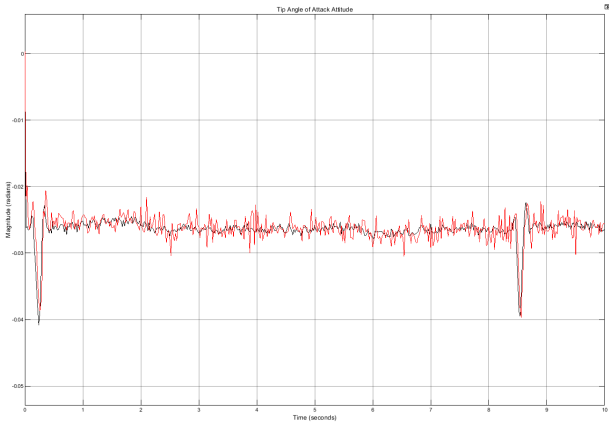

Figure 5.13: **(Model 2, Case 8)**. Value comparison of true attitude (black) and estimated attitude (red) of (from the first to the last) root heaving attitude, root angle-of-attack, tip heaving attitude and tip angle-of-attack. Reduced realization of 15 states.

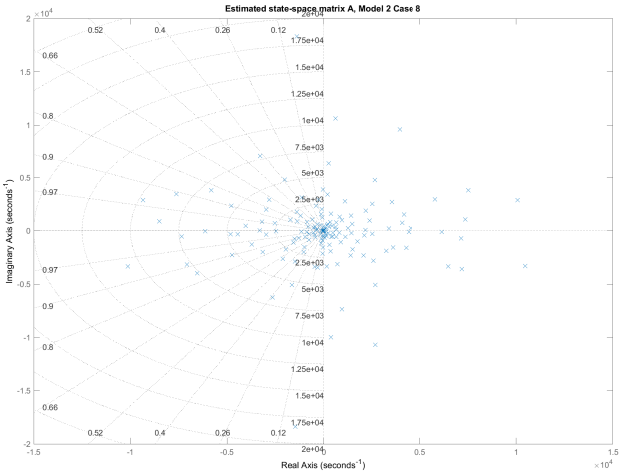

Figure 5.14: **(Model 2, Case 8)**. Estimated eigenvalues position of state-space matrix **A**.

5.1.3 Sampling Rate

The sampling rate influence the proposed method realization is also investigated by simulating the Case 9-10 for Model 2. For all the cases that have been presented, the system is established to work at a uniform sampling rate of 50 Hz. For Case 9, the system identification routine is set to run half the rate to 25 Hz. On the other hand, Case 10 is set at a double rate of 100 Hz. As previously mentioned in the introduction part and the analysis of the pole-zero map of Model 2, it can be seen that poles lie far within the left-half plane. Therefore, the higher the sampling rate, the more displacement modes of the wing section can be captured. Otherwise, the less the bending and torsion modes that can be captured. The noise realization can also be more pronounced with a lower sampling rate. Moreover, when the system is also coupled with faster sensors such as accelerometer and IMU to measure the forces and moments. By using the same reduced model of 15 states for Model 2, the state estimation results for both cases can be observed. For the Case 9, the state estimation results can be observed in Figure 5.15-5.16. It can be seen that at the lower sampling rate, the noise effect is even worse compared to the results of Case 2 (Chapter 4), which runs at 50 Hz. This might happen due to the accumulating process and measurement noise between samples of the slower sensor (i.e., visual tracker), which causes the noise realization to appear more prominent. One way to minimalize the noise is by adjusting the measurement unit to run at the same rate with the slower system compounded in

the scheme. This can be done through reprogramming the faster sensor or by filtering the measurement of the faster sensor. Variable-rate Kalman Filter is one way to filter the state estimation results based on the measurement from the fusion of slow-rate high-quality data with fast-rate low-quality data to form a more accurate fast-rate prediction of quality variables [18]. Case 9 simulation is then rerun by selecting the data so that the input and sensor noise yields an input at the same rate as the visual tracker frequency of 25 Hz. The results show a cleaner results compared to the previous run for all states. Therefore, it can be concluded that the uniformity of the sampling rate of the fused sensors plays a critical role in a more successful state estimation.

The sampling rate is increased to 100 Hz, as in Case 10. Compared to the state estimation results from the rerun Case 9, it can be seen that the deviation of estimated state values is less compared to the results obtained at a 25 Hz rate. This may be caused by the characteristics of the model itself. From the pole-zero map of Model 2 (Chapter 4, Figure 4.25), it can be seen that more displacement modes (complex eigenvalues) of the model lies far to the left on the left-half plane of the map. Therefore, by increasing the sampling rate, the more the displacement modes of the aeroelastic structure can be captured by the system. Hence, the deviation becomes less apparent. In addition to that, the occurring slow convergence can be apparent due to the choice of initial state or error covariance that is too small. This can be mitigated by choosing a larger value for the assumed covariance. The state estimation results of Case 10 can be seen in Figure 5.19-5.20. Despite the results, the parameter estimation results do not show the same characteristics as the true model. In both cases, there are also poles on the right-half plane. The finding means that the reconstructed state-space is not of a stable nature as the true model.

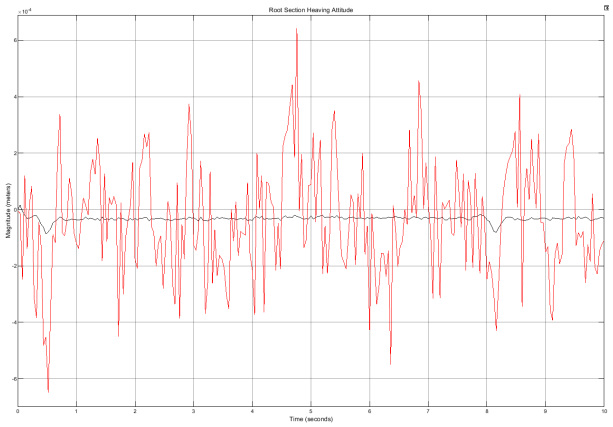

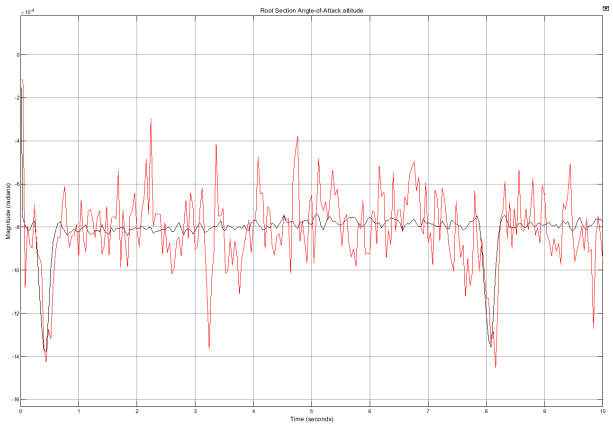

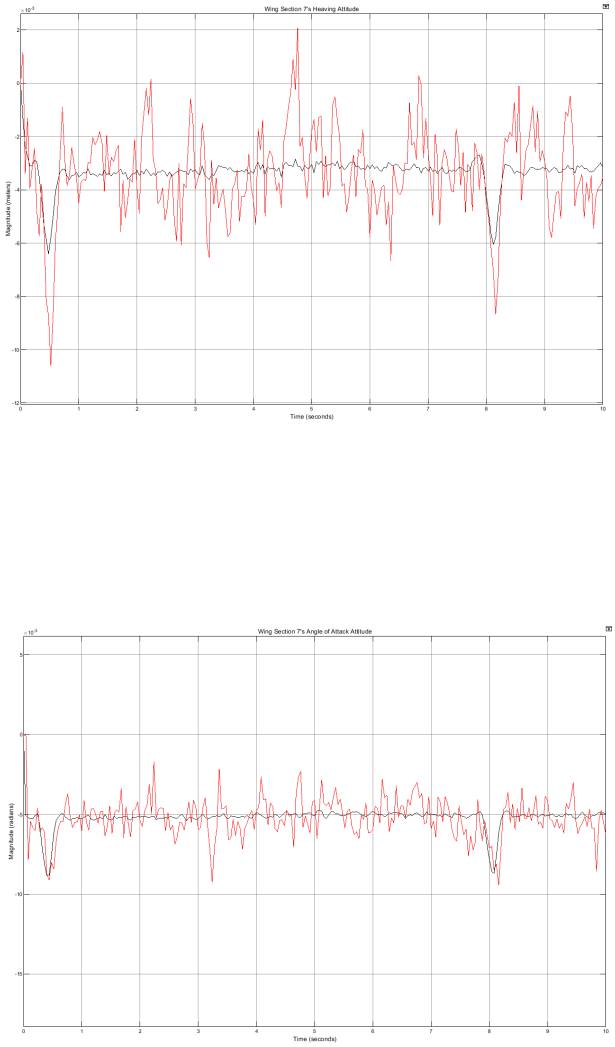

Figure 5.15: **(Model 2, Case 9)**. Value comparison of true attitude (black) and estimated attitude (red) of (from the first to the last) root heaving attitude, root angle-of-attack, Wing Section 7's heaving attitude and Wing Section 7's angle-of-attack. Reduced realization of 15 states.

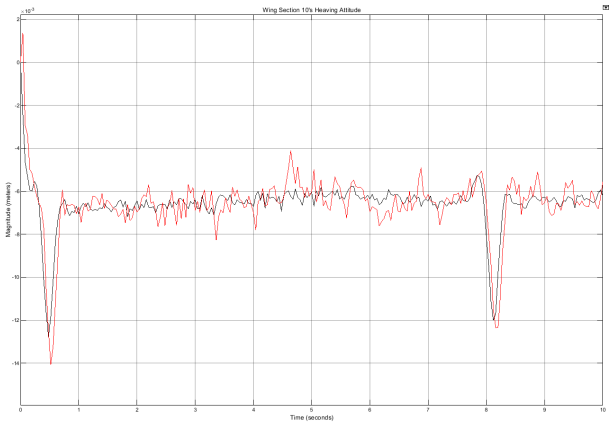

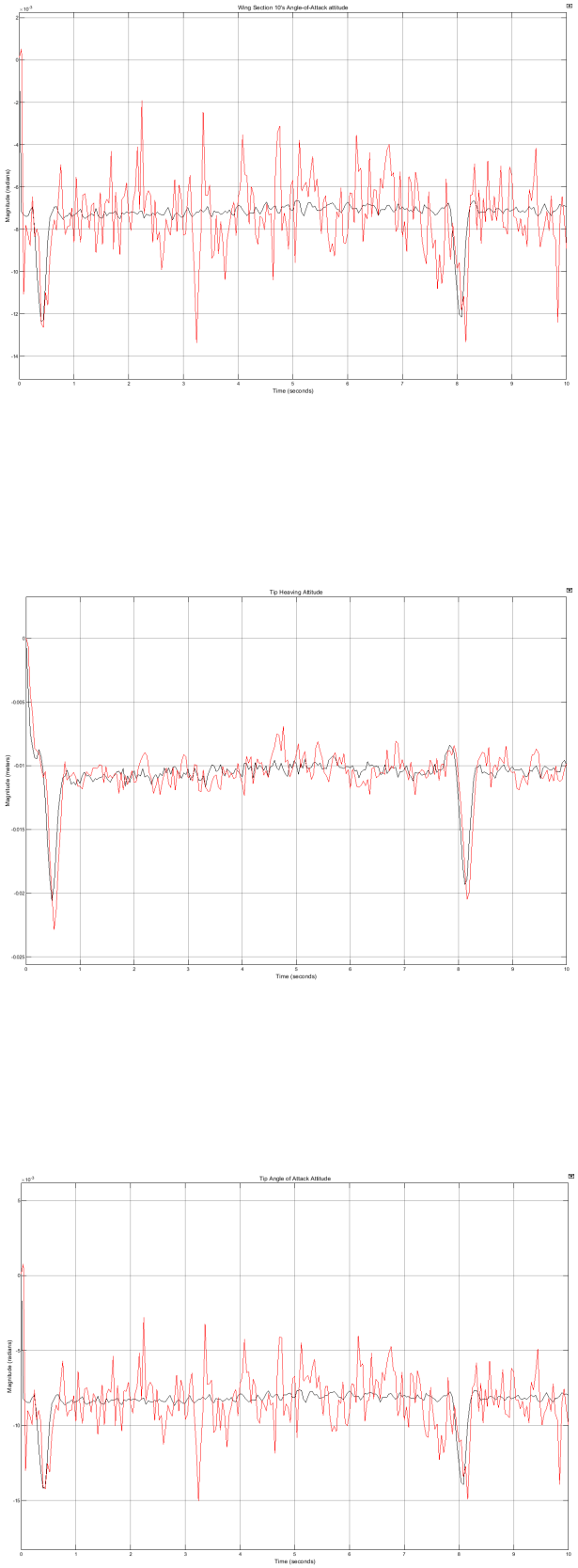

Figure 5.16: **(Model 2, Case 9)**. Value comparison of true attitude (black) and estimated attitude (red) of (from the first to the last) Wing Section 10's heaving attitude, Wing Section 10's angle-of-attack, tip heaving attitude and tip angle-of-attack. Reduced realization of 15 states.

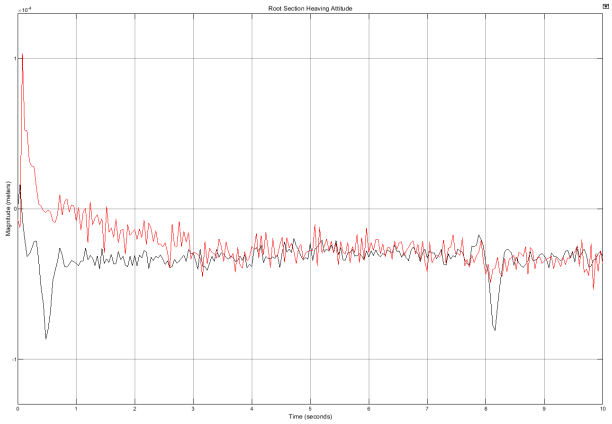
Root Section Heaving Attitude
Magnitude (meters)
Time (seconds)

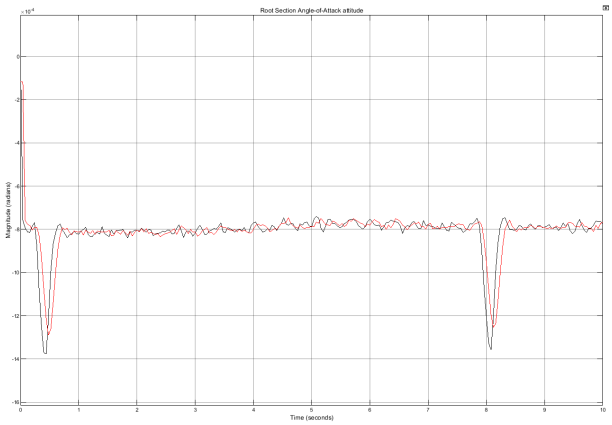
Root Section Angle-of-Attack attitude
Magnitude (radians)
Time (seconds)

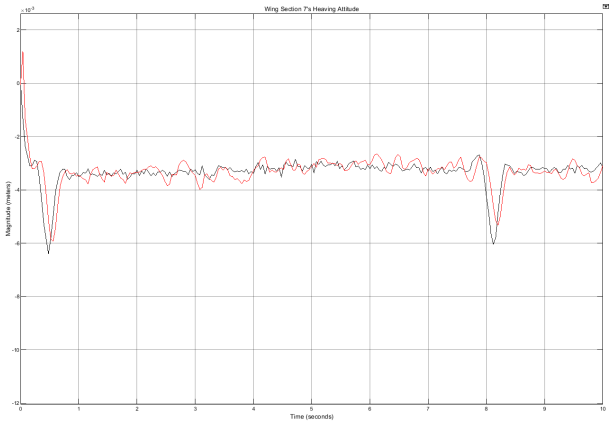
Wing Section 7's Heaving Attitude
Magnitude (meters)
Time (seconds)

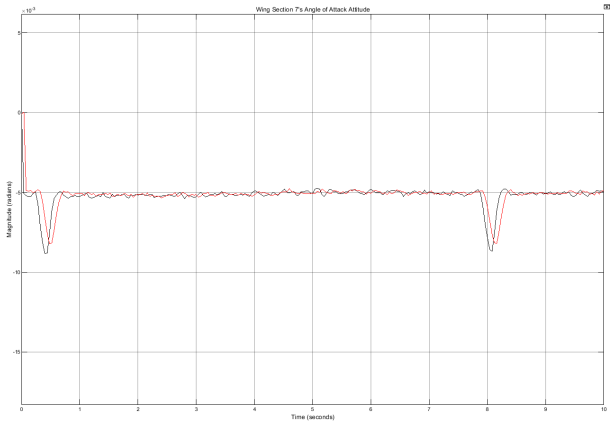

Figure 5.17: **(Model 2, Case 9)**. Rerun simulation by adjusting the sampling rate. Value comparison of true attitude (black) and estimated attitude (red) of (from the first to the last) root heaving attitude, root angle-of-attack, Wing Section 7's heaving attitude, and Wing Section 7's angle-of-attack. Reduced realization of 15 states.

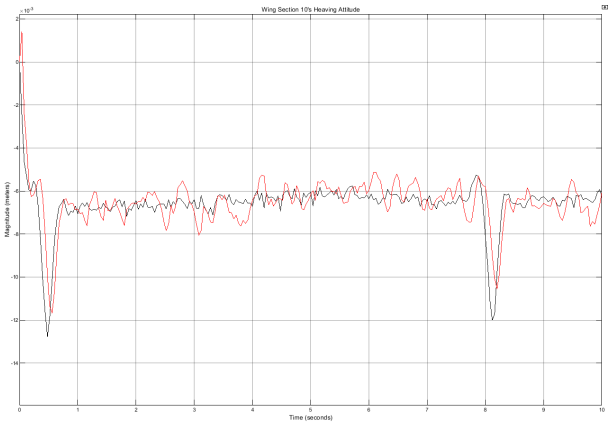

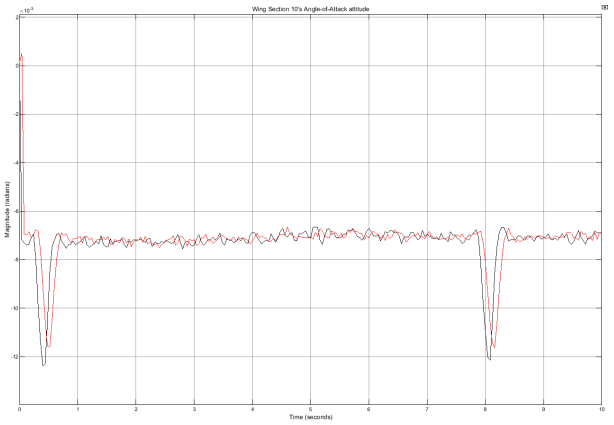

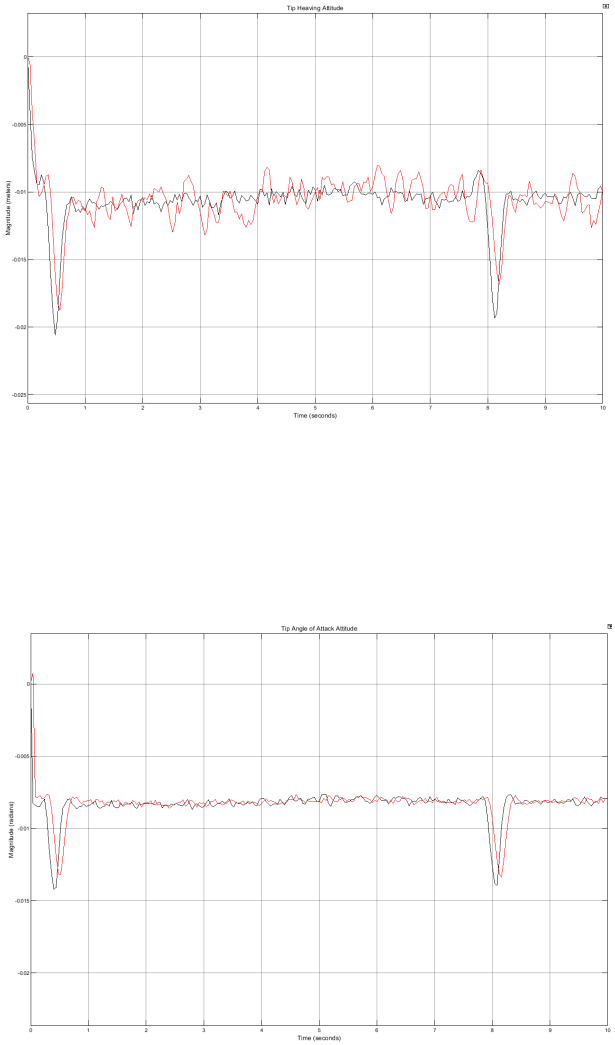

Figure 5.18: **(Model 2, Case 9)**. Rerun simulation by adjusting the sampling rate. Value comparison of true attitude (black) and estimated attitude (red) of (from the first to the last) Wing Section 10's heaving attitude, Wing Section 10's angle-of-attack, tip heaving attitude and tip angle-of-attack. Reduced realization of 15 states.

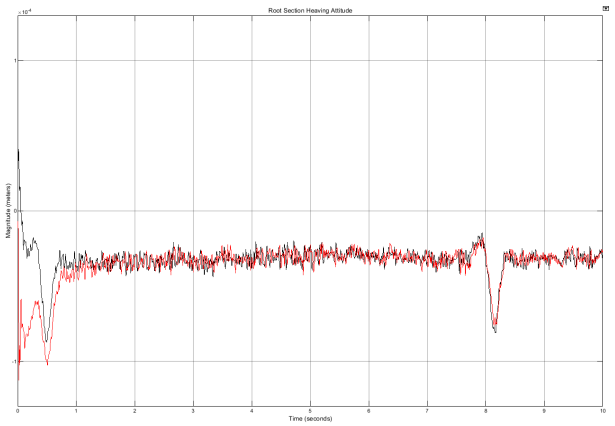

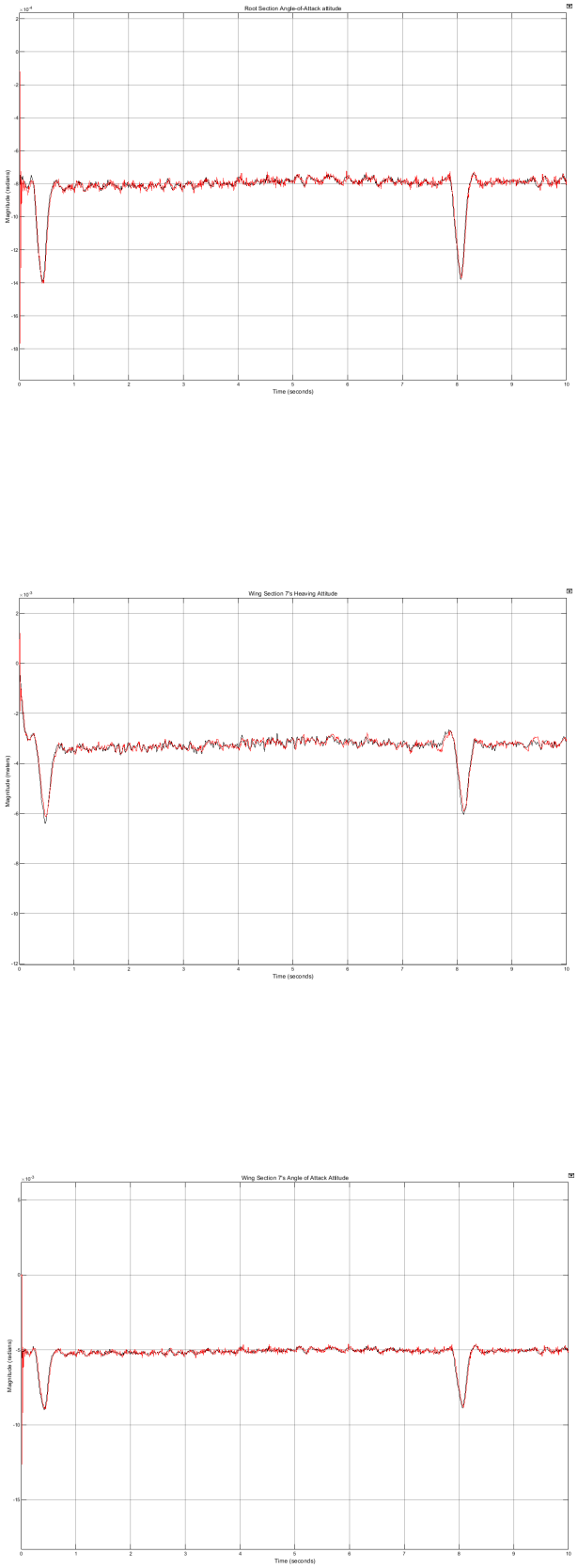

Figure 5.19: **(Model 2, Case 10)**. Value comparison of true attitude (black) and estimated attitude (red) of (from the first to the last) root heaving attitude, root angle-of-attack, Wing Section 7's heaving attitude and Wing Section 7's angle-of-attack. Reduced realization of 15 states.

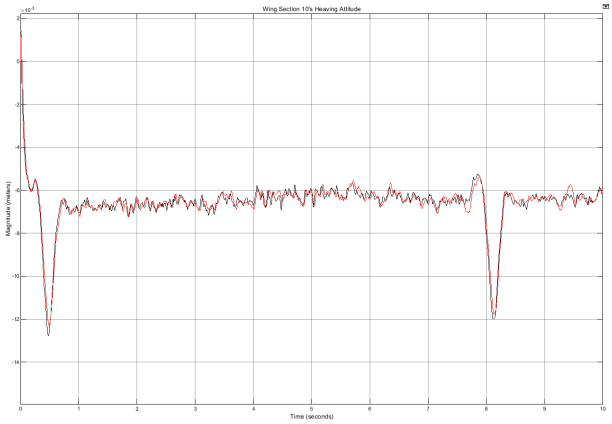
Wing Section 10's Heaving Attitude
Magnitude (meters)
Time (seconds)

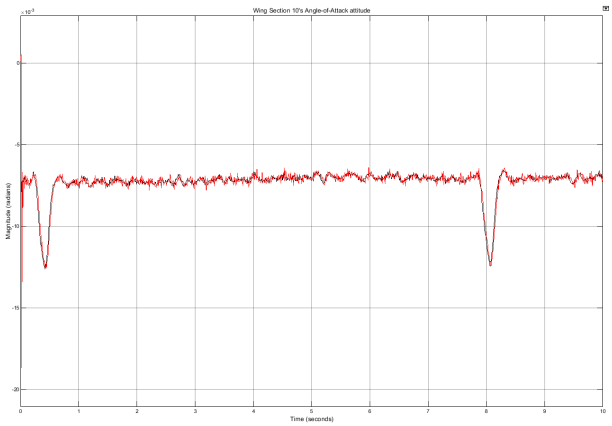
Wing Section 10's Angle-of-Attack attitude
Magnitude (radians)
Time (seconds)

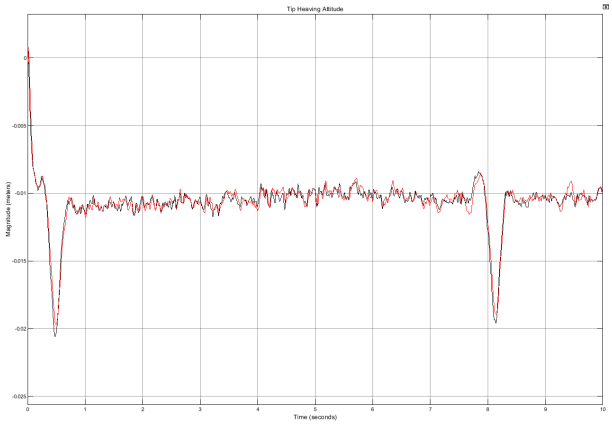
Tip Heaving Attitude
Magnitude (meters)
Time (seconds)

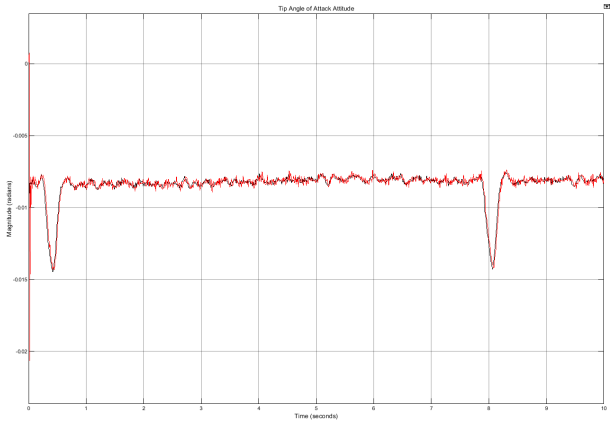

Figure 5.20: **(Model 2, Case 10)**. Value comparison of true attitude (black) and estimated attitude (red) of (from the first to the last) Wing Section 10's heaving attitude, Wing Section 10's angle-of-attack, tip heaving attitude and tip angle-of-attack. Reduced realization of 15 states.

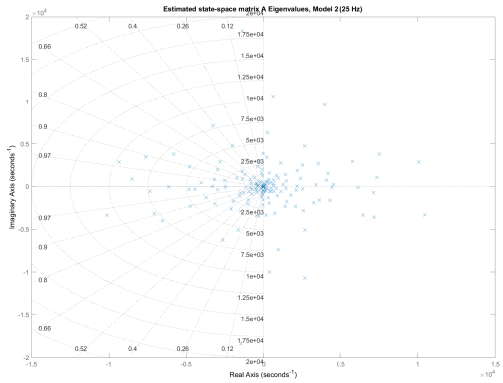

Figure 5.21: **(Model 2, Case 9)**. Estimated eigenvalues position of state-space matrix **A** for the sampling rate case of 25 Hz.

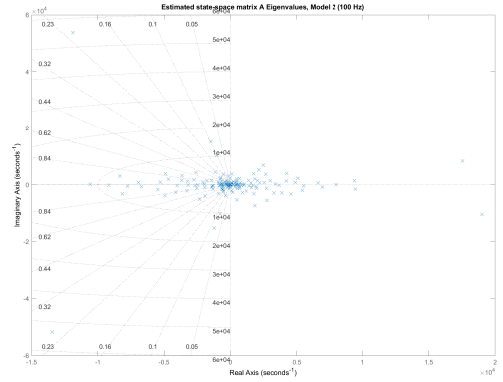

Figure 5.22: **(Model 2, Case 10)**. Estimated eigenvalues position of state-space matrix **A** for the sampling rate case of 100 Hz.

Chapter 6

Conclusion and Recommendations

6.1 Conclusions

With the advancements in the field of aerospace structure and material has brought breakthrough in the construction of air vehicles to be built bigger. However, with the lightness and the dimension, the structure can deform more appreciably due to the aerodynamic disturbance. An attempt is made by introducing visual tracking in combination with state estimation and parameter estimation in order to provide a cheaper method of structural health monitoring compared to the conventional method of planting the measurement units across the wing section.

In this chapter, the results will be concluded in order to answer the established research questions as follows.

- **What is the theoretical basis for the aircraft aeroelastic behaviors, and how does the behavior of the aeroelastic wing in fluttering or buffeting condition be represented mathematically?**

In Chapter 2, the derivation of the mathematical model has been derived that the mathematical model of an aeroelastic and aeroservoelastic wing dynamics are modeled after a spring-mass-damper system. It is confirmed that the behavior of an aeroelastic wing is influenced by aerodynamic profile and the structural profile of the wing itself. The aerodynamic influence representation in the time domain is introduced by Leishman and Nguyen [48] based on Wagner's indicial function derivation. It is hence expanding the state-space representation as it is influenced by aerodynamic lag to represent the influence of the circulatory trailing wake on top of the displacement attitude, rate, and acceleration of the wing itself. Based on the fusion of the Theodorsen and Leishman's state-space, the full model of aeroelastic behavior is then formed. From which the three-dimensional wing behavior is then developed based on the discretization of the wing. Therefore the whole behavior can then be analyzed by multiple two-dimensional wing sections. The final equation of Chapter 2 is the concluding remarks on how the wing is mathematically modeled in a three-dimensional form that will be implemented for the system identification.

- **Given the numerical measurement and process noises occurring in the process and the limitation of the hardware, what is the structure of the state and parameter estimation routine for the estimation of the aeroelastic object in visual tracking environment?**

Given the structure of previously answered in the first sub-research question, the state and parameter estimation can be performed. The question is fully answered in Chapter 3 that out of three possible methods for recursive structural health monitoring. The maximum likelihood estimation and augmented extended Kalman filter can be used to yield reliable results of state and parameter estimation. Based on the maximum likelihood estimation's relaxation technique, the state and parameter estimation can be further simplified in the routine form of the Two-Step Method. In order to further quicken the calculation, the model reduction is then performed by using modified Gawronski-Juang frequency-limited balanced truncation with the extension step of singular perturbation. The step is taken to obtain the least possible realization of the reduced model before executing the Two-Step Method based on the arbitrary and recommended parameters by literature. The structure for the routine is called as Reduced Order Two-Step (ROTS) method.

- **With the proposed framework, how does the state estimator routine in different conditions approximate the correct response? In other words, how robust is the proposed method for the different realization of turbulence, and what are the influencing parameters that may affect the state estimation results with the given system environment**?

The state estimator performance is observed and analyzed in eight simulation cases in Chapters 4 and 5. The simulated simulation cases are set up with the parameters given in Subchapter 4.3.2. From the results, it can be observed that the routine shows the convergence at all states of interest in any gust realizations in the condition where the forces and moments input are sampled at higher rate. Therefore, it can be concluded that the proposed method up to the state estimation step is a robust method at the given conditions. The error or deviation that may occur during the state estimation comes from the process noise and measurement noise. Based on the simulation results, it can be seen that the deviation is more pronounced at the states related to the wing sections closer to the root. Otherwise, the deviation also occurs more in the states where the weak excitation occurs, i.e., the displacement is insignificant compared to the change in force and moment. Furthermore, the higher airspeed condition shows the noise to be less pronounced, in particular for the angular state of wing section closer to the root. In addition to that, the simulations have also been conducted with changes in the damping term. In both cases of low damping and high damping coefficient, the results show the convergence as well. The sampling rate also affects the state estimation quality in terms of noise clearance. The higher the sampling rate, the less noisy the state estimation measurement is as the process and measurement noise are not accumulated in the time-space between samples. However, the noise occurring in the state estimation can be further mitigated by adjusting the forces and moment sensor to run at the same sampling rate.

- **How does the proposed method reconstruct the true parameter values such that the reconstructed system can imitate the true model of the system? What is the error that occurs during the parameter estimation**?

In parallel with the state estimation analysis routine of the method, the parameter estimation analysis is also conducted at every end of the simulation. From the results, it can be seen uniformly that in terms of structure, the method can duplicate the structure of the mass, damping, and stiffness matrices. Nevertheless, for all presented cases and models, the eigenvalues of the reconstructed state-space **A** matrix do not maintain the original stability of the true model. The failure is caused by the presence of poles on the right-half plane. The same results are also obtained with the change in damping realization, gust realization, and sampling rate. Further analysis is recommended to be focused in this part in order to ensure that the stability of the true model can be retained.

In the end, the main research objective is again reviewed.

Contribute to the development of the online state estimator for the dynamics and aeroelastic constants from the nonlinear flexible structure of flexible rectangular wing by investigating the feasibility of application of existing online state estimation framework within active controller scheme for structural integrity control with visual tracking to estimate aeroelastic dynamics and its parameters in Theodorsen's fluttering condition.

In this thesis, the full mathematical modeling of the three-dimensional aeroelastic structure behavior has been derived based on the derivation of state-space by Theodorsen and Leishman. Furthermore, the system identification method is chosen and modified in order to obtain the smallest realizations. Therefore, a complex calculation, which consists of a large number of states, can be minimalized to reduce the computational cost. The verification of the proposed method has been carried out. The results show that it is possible to yield an accurate estimation of the displacement state of an aeroelastic structure based on calculating the true dynamics of the system instead of doing so in the pixel reference frame. The results have been supported by the convergence of all presented states in the ten simulation cases presented in Chapters 4 and 5. From reflecting on the main objective of the system identification in the controller scheme, it can be seen that the final objective of yielding an accurate representation of the aeroelastic system is still not achieved due to the occurring results despite the convergence of the state estimation results. The results show different characteristics from the true models where all poles lie on the left-half plane. The finding should become the ground for the next analysis in improving the Two-Step Method for structural system identification. Further investigation is recommended to be focused on this part to ensure that the stability of the true model can be retained to yield an accurate solution for the aeroelastic controller feedback. Furthermore, the results of the formed Reduced-Order Two-Step (ROTS) can be used as the basis for the next research for the implementation of the routine in the visual structural health monitoring in real-time.

6.2 Recommendations

Based on the findings, a few recommendation points can then be formed.

1. In this research, the calculation is based on the visual tracking environment. Therefore the parameters taken into consideration in the presented simulation cases are based on this account. A higher verification level needs to be carried out by integrating the proposed method routine with the simulated visual tracking such as in Blender before implementing it in the real system.

2. During the phase of the thesis work, an idea was discovered to make a feedback loop between the Recursive Least-Square and the Kalman Filter routines such that the state-space system could be renewed for every iteration. This idea is currently hampered by the instability problem of the reconstructed state-space matrix. Therefore, based on the writer's concern, the focus for the next research should be on integrating some constraints in the recursive least square in order to obtain a stable reconstruction of the state-space.

3. In addition to the first point, it can be seen from the formation of the regression and output matrix that the structure of the matrices has been formed initially by doing the naive model decomposition based on the structure of the model. Nevertheless, it might be possible that other more sophisticated model decomposition methods can be applied to the routine such that the residual or error accumulated during the process of the parameter estimation will yield a smaller error to the formation of restructured state-space matrices.

4. In this research, the linear Kalman Filter is proposed based on initial information of the mass and stiffness matrix. While the structural matrices will be the same if the gust load is in the elastic region, the structure will ultimately suffer from fatigue due to a long period of load exposure. This will have an implication on the mass and stiffness. This alone is the reason why the idea of making a feedback loop between the parameter estimation and the state estimation routine is based on in the first place. Another way to do is by the implementation of model reduction for nonlinear state-space. In very recent years, few research efforts have been conducted in order to find a suitable routine for this condition. The benefit of research in this field can also be investigated in future research.

5. In this research, it can be seen that the fusion of multiple sensors at different sampling rate may cause noise realization to occur at greater magnitude compared to the results where the IMU, visual tracker, and the system identicatin routine work at the same rate (see the sampling rate analysis on Chapter 5). One idea to mitigate the condition is by pre-processing data utilizing variable-rate Kalman Filter. This can be further implemented to augment the accuracy of the results in future research.

6. Lastly, at the technical level, it is also found that the measurement noise in the camera frame is based on the representation of the object in pixel units, with a camera of high resolution, the measurement noise can then be decreased. Furthermore, the implementation in other programming languages is preferable for the simulation as the simulation may take a longer time in the presented console.

Bibliography

[1] M Sanjeev Arulampalam, Simon Maskell, Neil Gordon, and Tim Clapp. A tutorial on particle filters for online nonlinear/non-gaussian bayesian tracking. *IEEE Transactions on Signal Processing*, 50(2):174–188, 2002.

[2] David C. Asjes. *Nonlinear analysis of a two- and three-degree-of-freedom aeroelastic system with rotational stiffness free-play*. PhD thesis, Iowa State University, 2015.

[3] Sonali Bagchi and Sanjit K. Mitra. *Filtering and System Identification: A Least Squares Approach*. Springer US, 1999.

[4] Chenglong Bao, Yi Wu, Haibin Ling, and Hui Ji. Real time robust l1 tracker using accelerated proximal gradient approach. In *2012 IEEE Conference on Computer Vision and Pattern Recognition*, pages 1830–1837. IEEE, 2012.

[5] Bart Besselink, Umut Tabak, Agnieszka Lutowska, Nathan Van de Wouw, H Nijmeijer, Daniel J Rixen, ME Hochstenbach, and WHA Schilders. A comparison of model reduction techniques from structural dynamics, numerical mathematics and systems and control. *Journal of Sound and Vibration*, 332(19): 4403–4422, 2013.

[6] Nilesh Bhoir and Sahjendra N Singh. Output feedback nonlinear control of an aeroelastic system with unsteady aerodynamics. *Aerospace Science and Technology*, 8(3):195–205, 2004.

[7] Emmanuel Blanchard, Adrian Sandu, and Corina Sandu. Parameter estimation method using an extended kalman filter. *Proceedings of the Joint North America, Asia-Pacific ISTVS Conference and Annual Meeting of Japanese Society for Terramechanics*, pages 1–14, 2007.

[8] David S Bolme, J Ross Beveridge, Bruce A Draper, and Yui Man Lui. Visual object tracking using adaptive correlation filters. In *2010 IEEE Computer Society Conference on Computer Vision and Pattern Recognition*, pages 2544–2550. IEEE, 2010.

[9] Cheng Chang and Rashid Ansari. Kernel particle filter for visual tracking. *IEEE Signal Processing Letters*, 12(3):242–245, 2005.

[10] Zhe Chen. Bayesian filtering: From kalman filters to particle filters, and beyond. *Statistics*, 182(1):1–69, 2003.

[11] Eric Cuevas, Daniel Zaldivar, and Raul Rojas. Kalman filter for vision tracking, technical report b 05-12. Technical report, Freie Universitaet Berlin, Institut fuer Informatik, Berlin, Germany, 2005.

[12] E Davison. A method for simplifying linear dynamic systems. *IEEE Transactions on automatic control*, 11(1):93–101, 1966.

[13] Roeland de Breuker. *Energy-based aeroelastic analysis and optimisation of morphing wings'*. PhD thesis, Delft University of Technology, 2011.

[14] Roeland de Breuker, Simon Binder, and Andreas Wildschek. Combined active and passive loads alleviation through aeroelastic tailoring and control surface/control system optimization. 2018.

[15] Visvanathan Ramesh Dorin Comaniciu and Peter Meer. Kernel-based object tracking. *IEEE Transactions on Pattern Analysis and Machine Intelligence*, 25(5):564–577, 2003.

[16] Norman R Draper and Harry Smith. *Applied regression analysis*, volume 326. John Wiley & Sons, 1998.

[17] Dale F Enns. Model reduction with balanced realizations: An error bound and a frequency weighted generalization. In *The 23rd IEEE conference on decision and control*, pages 127–132. IEEE, 1984.

[18] Alireza Fatehi and Biao Huang. Kalman filtering approach to multi-rate information fusion in the presence of irregular sampling rate and variable measurement delay. *Journal of Process Control*, 53:15–25, 2017.

[19] Nathan Funk. A study of the kalman filter applied to visual tracking. *University of Alberta, Project for CMPUT*, 652(6), 2003.

[20] I.E. Garrick and Wilmer H. Reed III. Historical development of aircraft flutter. *AIAA Journal of Aircraft*, 18(11):897–912, 1981.

[21] Wodek Gawronski and Jer-Nan Juang. Model reduction in limited time and frequency intervals. *International Journal of Systems Science*, 21(2):349–376, 1990.

[22] Roger Ghanem and Masanobu Shinozuka. Structural-system identification i: Theory. *ASCE Journal of Engineering Mechanics*, 121(2):255–264, 1994.

[23] Erik Gillebaart and Roeland De Breuker. Reduced-order modeling of continuous-time state-space unsteady aerodynamics. In *53rd AIAA Aerospace Sciences Meeting*, page 0260, 2015.

[24] Graham Clifford Goodwin and Robert L Payne. *Dynamic system identification : experiment design and data analysis*. Academic Press, New York, 1977.

[25] Jared A. Grauer and Eugene A. Morelli. A new formulation of the filter-error method for aerodynamic parameter estimation in turbulence. page 2704. doi: 10.2514/6.2015-2704.

[26] William Gressick, John T Wen, and Jacob Fish. Order reduction for large-scale finite element models: A systems perspective. *International Journal for Multiscale Computational Engineering*, 3(3), 2005.

[27] Serkan Gugercin and Athanasios C Antoulas. A survey of model reduction by balanced truncation and some new results. *International Journal of Control*, 77(8):748–766, 2004.

[28] Kenneth C Hall. Eigenanalysis of unsteady flows about airfoils, cascades, and wings. *AIAA journal*, 32 (12):2426–2432, 1994.

[29] Richard I. Hartley and Peter Sturm. Triangulation. *Computer Vision and Image Understanding*, 68(2): 146–157, 1997.

[30] João F Henriques, Rui Caseiro, Pedro Martins, and Jorge Batista. High-speed tracking with kernelized correlation filters. *IEEE Transactions On Pattern Analysis and Machine Intelligence*, 37(3):583–596, 2014.

[31] Nicholas J Higham. Computing a nearest symmetric positive semidefinite matrix. *Linear algebra and its applications*, 103:103–118, 1988.

[32] Philip Holmes, John L Lumley, Gahl Berkooz, and Clarence W Rowley. *Turbulence, coherent structures, dynamical systems and symmetry*. Cambridge university press, 2012.

[33] Masaru Hoshiya and Etsuro Saito. Structural identification by extended kalman filter. *Journal of Engineering Mechanics, ASCE*, 110(12):1757–1770, 1984.

[34] Xuan-Phung Huynh, In-Ho Choi, and Yong-Guk Kim. Tracking a human fast and reliably against occlusion and human-crossing. In *Image and Video Technology*, pages 461–472. Springer, 2015.

[35] Rob J Hyndman and Anne B Koehler. Another look at measures of forecast accuracy. *International journal of forecasting*, 22(4):679–688, 2006.

[36] Daniel J. Inman. *Engineering Vibration*. Prentice-Hall, Inc., 2001.

[37] Roberto Isacco. Design Guidelines for Gust Load Inclusion in Aeroelastic Optimization of a Civil Aircraft in the Preliminary Design Phase. Master's thesis, Delft University of Technology, the Netherlands, 2019.

[38] Helmut John. Critical review of methods to predict the buffet capability of aircraft, ad-a008 593. Technical report, Messerschmitt-Boelkow-Blohm G.m.b.H, 1974.

[39] R.T. Jones. The unsteady lift of a wing of finite aspect ratio. Technical report, 1940.

[40] Simon J. Juller and Jeffrey K. Uhlmann. A new extension of the kalman filter to nonlinear systems. In *Signal processing, sensor fusion, and target recognition VI*, volume 3068, pages 182–194. International Society for Optics and Photonics, 1997.

[41] R.E. Kalman. A new approach to linear filtering and prediction problems. *Transactions of the ASME–Journal of Basic Engineering*, 82(1):35–45, 1960.

[42] Rudolph E Kalman and Richard S Bucy. New results in linear filtering and prediction theory. *Journal of Basic Engineering*, 83(1):95–108, 1961.

[43] Vladislav Klein and Eugene A. Morelli. *Aircraft System Identification.* AIAA, 2006.

[44] Petar V Kokotovic, Robert E O'Malley Jr, and Peddapullaiah Sannuti. Singular perturbations and order reduction in control theory—an overview. *Automatica*, 12(2):123–132, 1976.

[45] H. G. Küssner. Zusammenfassender bericht über den instationären auftrieb von flügeln. *Luftfahrtforschung 13, 410*, 1936.

[46] Alanj Laub, MICHAELT Heath, C Paige, and R Ward. Computation of system balancing transformations and other applications of simultaneous diagonalization algorithms. *IEEE Transactions on Automatic Control*, 32(2):115–122, 1987.

[47] B.H.K. Lee, L.Y. Jiang, and Y.S. Wong. Flutter of an airfoil with a cubic restoring force. *Journal of Fluids and Structures*, 13(1):75–101, 1999.

[48] J.G. Leishman and K.Q. Nguyen. State-space representation of unsteady airfoil behavior. *American Institute of Aeronautics and Astronautics (AIAA) Journal*, 28(5):836–844, 1990.

[49] Peihua Li, Tianwen Zhang, and Bo Ma. Unscented kalman filter for visual curve tracking. *Image and Vision Computing*, 22(2):157–164, 2004.

[50] Ting Liu, Gang Wang, and Qingxiong Yang. Real-time part-based visual tracking via adaptive correlation filters. In *2015 IEEE Conference on Computer Vision and Pattern Recognition (CVPR)*, pages 4902–4912. IEEE, 2015.

[51] L. Ljung and T. Söderström. *Theory and Practice of Recursive Identification.* MIT Press, 1983.

[52] Lennart Ljung. *System Identification Theory for the User.* Prentice Hall, Inc., second edition, 1999.

[53] Gertjan Looye. Basics of aeroelasticity and flutter analysis. Technical report, German Aerospace Research Center, Oberpfaffenhofen, Germany, 1998.

[54] Bruce D. Lucas and Takeo Kanade. An iterative image registration technique with an application to stereo vision. *International Joint Conference on Artificial Intelligence*, pages 674–679, 1981.

[55] Bruce Moore. Principal component analysis in linear systems: Controllability, observability, and model reduction. *IEEE transactions on automatic control*, 26(1):17–32, 1981.

[56] J. A. Mulder. *Design and Evaluation of Dynamic Flight Test Maneuvers.* PhD thesis, Delft University of Technology, 1986.

[57] Pietro Muraca and Ciro Picardi. A reduced order extended kalman filter algorithm for parameter and state estimation of an induction motor. In *Algorithms and Architectures for Real-Time Control 1992*, pages 225–230. Elsevier, 1992.

[58] Nhan Nguyen and Ilhan Tuzcu. Flight dynamics of flexible aircraft with aeroelastic and inertial force interactions, 2009.

[59] Altan Odabasioglu, Mustafa Celik, Lawrence T Pileggi, Lawrence T Pileggi, and Lawrence T Pileggi. Prima: Passive reduced-order interconnect macromodeling algorithm. In *Proceedings of the 1997 IEEE/ACM international conference on Computer-aided design*, pages 58–65. IEEE Computer Society, 1997.

[60] Katsuhiko Ogata. *Modern Control Engineering, 5th Edition*. Prentice Hall Inc., 2010.

[61] Aanchal Pathak and Esmita Singh. Comparative study on filtering techniques of digital image processing. *Advance in Electronic and Electric Engineering*, 4(6):669–674, 2014.

[62] Mayuresh J. Patil. Limit-cycle oscillations of aircraft caused by flutter-induced drag. *Journal of Aircraft*, 41(3):571–576, 2004.

[63] Mayuresh J. Patil and Dewey H. Hodges. Flight dynamics of highly flexible flying wings. *Journal of Aircraft, November-December 2006*, 43(6):1790–1799, 2006.

[64] J. A. Mulder Q.P. Chu and J.K. Sridhar. Decomposition of aircraft state and parameter estimation problem. *IFAC Proceeding Volumes*, 27(8):1025–1030, 1994.

[65] Marianne J. Reijerkerk. *Aeroelastic Model Identification of Winglet Loads from Flight Test Data*. PhD thesis, Delft University of Technology, 2006.

[66] Andres Rodriguez, Jeffrey Panza, B.V.K. Vijaya Kumar, and Abhijit Mahalanobis. Automatic recognition of multiple targets with varying velocities using quadratic correlation filters and kalman filters. *IEEE Radar Conference*, pages 446–451, 2010.

[67] Clarence W Rowley. Model reduction for fluids, using balanced proper orthogonal decomposition. *International Journal of Bifurcation and Chaos*, 15(03):997–1013, 2005.

[68] Yong Rui and Yunqiang Chen. Better proposal distributions: Object tracking using unscented particle filter. In *Proceedings of the 2001 IEEE Computer Society Conference on Computer Vision and Pattern Recognition. CVPR 2001*, volume 2, pages II–786. IEEE, 2001.

[69] Carl Runge. Über empirische funktionen und die interpolation zwischen äquidistanten ordinaten. *Zeitschrift für Mathematik und Physik*, 46(224-243):20, 1901.

[70] Yousef Saad. *Iterative methods for sparse linear systems*, volume 82. siam, 2003.

[71] Jianbo Shi and Carlo Tomasi. Good features to track. *IEEE Conference on Computer Vision and Pattern Recognition*, pages 593–600, 1994.

[72] Masanobu Shinozuka and Roger Ghanem. Structural system identification ii: Experimental verification. *Journal of Engineering Mechanics*, 121(2):265–273, 1995.

[73] Haithem E. Taha, Muhammad R. Hajj, and Philip S.Beran. State-space representation of the unsteady aerodynamics of flapping flight. *Aerospace Science and Technology*, 34:1–11, 2014.

[74] Theodore Theodorsen. General theory of aerodynamic instability and the mechanism of flutter. Technical report, National Advisory Committee for Aeronautics, United States of America, 1949.

[75] S. Timme and F. Sartor. Passive control of transonic buffet onset on a half wing-body configuration. *International Forum on Aeroelasticity and Structural Dynamics*, 2015.

[76] Henry Tol. *Finite-dimensional approximation and control of shear flows*. PhD thesis, Delft University of Technology, 2018.

[77] P. Verboven, B.Cauberghe, P. Guillaume, S. Vanlanduit, and E. Parloo. Modal parameter estimation and monitoring for online flight flutter analysis. *Mechanical Systems and Signal Processing 18*, 18(3):587–610, 2004.

[78] Eric A. Wan and Rudolph van der Merwe. The unscented kalman filter for nonlinear estimation. *Proceedings of the IEEE 2000 Adaptive Systems for Signal Processing, Communications, and Control Symposium*, pages 153–158, 2000.

[79] Noud Philip Maria Werter. *Aeroelastic Modelling and Design of Aeroelastically Tailored and Morphing Wings*. PhD thesis, Delft University of Technology, 2017.

[80] NPM Werter and R De Breuker. A novel dynamic aeroelastic framework for aeroelastic tailoring and structural optimisation. *Composite Structures*, 158:369–386, 2016.

[81] Karen Willcox and Jaime Peraire. Balanced model reduction via the proper orthogonal decomposition. *AIAA journal*, 40(11):2323–2330, 2002.

[82] Meiliang Wu and Andrew W. Smyth. Application of unscented kalman filter for real-time nonlinear structural system identification. *Structural Control and Health Monitoring: The Official Journal of the International Association for Structural Control and Monitoring and of the European Association for the Control of Structures*, 14(7):971–990, 2007.

[83] Liyu Xie, Zhenwei Zhou, Lei Zhao, Chunfeng Wan, Hesheng Tang, and Songtao Xue. Parameter identification for structural health monitoring with extended kalman filter considering integration and noise effect. *Applied Sciences*, 8(12):2480, 2018.

[84] Zongbo Xie and Jiuchao Feng. Real-time nonlinear structural system identification via iterated unscented kalman filter. *Mechanical systems and signal processing*, 28:309–322, 2012.

[85] Ronghui Zhan and Jianwei Wan. Iterated unscented kalman filter for passive target tracking. *IEEE Transactions on Aerospace and Electronic Systems*, 43(3):1155–1163, 2007.